



Cite as

Nano-Micro Lett.
(2020) 12:118Received: 22 March 2020
Accepted: 22 April 2020
© The Author(s) 2020

A Review on Nano-/Microstructured Materials Constructed by Electrochemical Technologies for Supercapacitors

Huizhen Lv¹, Qing Pan¹, Yu Song¹ ✉, Xiao-Xia Liu¹, Tianyu Liu² ✉

Huizhen Lv and Qing Pan have contributed equally to this work.

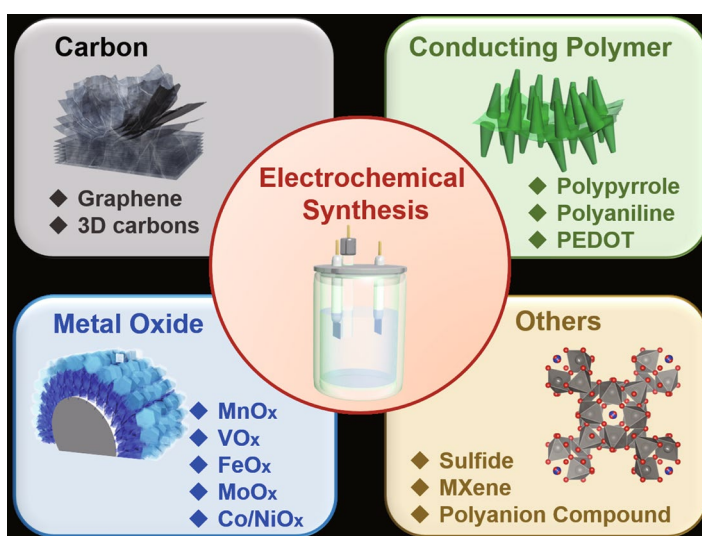
✉ Yu Song, songyu@mail.neu.edu.cn; Tianyu Liu, tliu23@vt.edu¹ Department of Chemistry, Northeastern University, Shenyang 110819, People's Republic of China² Department of Chemistry, Virginia Polytechnic Institute and State University, Blacksburg, VA 24061, USA

HIGHLIGHTS

- Recent progress of active materials in supercapacitors synthesized by electrochemical techniques is reviewed.
- Electrochemically synthesized nanostructures of various dimensions, compositions, and electrochemical properties are discussed.
- The advantages and challenges of electrochemical technologies in preparing nano-/microstructured materials for electrochemical energy storage devices are summarized.

ABSTRACT The article reviews the recent progress of electrochemical techniques on synthesizing nano-/microstructures as supercapacitor electrodes. With a history of more than a century, electrochemical techniques have evolved from metal plating since their inception to versatile synthesis tools for electrochemically active materials of diverse morphologies, compositions, and functions. The review begins with tutorials on the operating mechanisms of five commonly used electrochemical techniques, including cyclic voltammetry, potentiostatic deposition, galvanostatic deposition, pulse deposition, and electrophoretic deposition, followed by thorough surveys of the nano-/microstructured materials synthesized electrochemically. Specifically, representative synthesis mechanisms and the state-of-the-art electrochemical performances of exfoliated graphene, conducting polymers, metal oxides, metal sulfides, and their composites are surveyed. The article concludes with summaries of the unique merits, potential challenges, and associated opportunities of electrochemical synthesis techniques for electrode materials in supercapacitors.

KEYWORDS Nanostructure; Microstructure; Electrochemical; Synthesis; Supercapacitor



1 Introduction

The rapidly expanding markets of mobile electronics, electrified transportation, wireless networks (e.g., the Internet of Things), and sustainable energy utilization have substantially fueled the development of electrochemical energy storage systems [1–4]. Supercapacitors, including electrochemical capacitors and pseudocapacitors, stand out among diverse arrays of energy storage devices due to their ultrahigh power density and ultralong life spans [5–9]. Since the first introduction in 1957 by Howard Becker of American General Electric [10], supercapacitors have pervaded in applications demanding energy input and output with high power, e.g., the power source to the emergency doors of Airbus A380 aircraft [11, 12]. Therefore, elevating the capacitance and energy density of supercapacitors at ultrafast charging rates has remained a central topic [13–16]. Extensive research efforts have been devoted to developing high-performance electrode materials [13, 15–17], since electrodes primarily determine the capacitance, energy density, and power density of supercapacitors.

Supercapacitors are classified into two categories: electric double-layer capacitors (EDLCs) and pseudocapacitors. EDLCs store charges through adsorption and desorption of ions in electrolytes at the electrolyte/electrode interfaces. Carbon materials are conventional electrode materials in EDLCs. Pseudocapacitors store charges through kinetically fast Faradaic reactions. Surface redox pseudocapacitance, intercalation pseudocapacitance, and underpotential deposition are examples of pseudocapacitance [13]. Redox pseudocapacitance occurs when electrolyte ions adsorbed on or near the electrode surfaces and involves interfacial charge transfer. Intercalation pseudocapacitance comes from reversible insertion and desorption of electrolyte ions in layered or tunneled electrode materials without phase transitions. Underpotential deposition will be elaborated in Sect. 2.2, but it is not used for charge storage due to its limited capacity. Pseudocapacitance has its electrochemical features, such as quasi-rectangular cyclic voltammetry curves, linear galvanostatic charge/discharge profiles, as well as a near-linear response between current and scan rate in cyclic voltammograms. These characteristics must be clearly distinguished from battery-type behaviors (Sect. 5.6).

Electrochemical techniques are a group of synthesis methods of versatile active materials in supercapacitors. These

methods have a history of more than 150 years [18], and their first application is to plate metals for jewelry decoration, surface protection, and electronic-circuit manufacturing [19]. Along with the boom of electrochemical energy storage, the role of electrochemical techniques has been enriched by synthesizing nano-/microstructured materials for electrochemical energy storage [2, 20]. The syntheses involve electrochemical processes including reduction, oxidation, gas evolution, ion intercalation, and combinations of these methods thereof. Chemical reactions, such as the electrolysis of electrolytes (e.g., H_2 and O_2 evolution in aqueous electrolytes), redox reactions of electrolyte ions, as well as modifications of the structures and compositions of electrode materials, are typically accompanying phenomena.

Compared to other synthesis strategies, electrochemical techniques have their unique advantages. First, they are facile and mild. Room temperature, ambient pressure, and aqueous solutions are sufficient for performing electrochemical techniques. Second, the experimental setups, such as electrolytic cells and electrochemical workstations, are often readily available in electrochemistry laboratories. This availability allows electrochemists to prepare active materials without delicate instruments and sophisticated protocols. Perhaps the most striking feature of electrochemical techniques is their high tunability toward the structure, composition, property, and morphology of products [2, 20]. Magnitudes of applied current or voltage, types and concentrations of salts in electrolytes, reaction durations, solution temperatures, as well as substrate morphologies are all tunable parameters that result in versatile materials. Benefited from these merits, electrochemical techniques have been extensively studied and rapidly developed in the past decades. The materials that have been prepared electrochemically include exfoliated graphene [21], metal oxides [22–24], conducting polymers [25, 26], and their composites [27–29].

This review article presents a thorough survey of electrochemically synthesized nano-/microstructured materials for supercapacitors. It starts with introduction of the operating mechanisms, characteristics of input and output signals, strengths, and weaknesses of cyclic voltammetry, potentiostatic (constant voltage) and galvanostatic (constant current) depositions, pulse electrodeposition, and electrophoretic deposition. Afterward, the article reviews the recent progress of the active materials synthesized by electrochemical techniques. This part is segmented based on the compositions of

materials, including carbon-based materials, metal oxides, conducting polymers, composites, and other materials. Each subsection starts with typical synthesis mechanisms and is exemplified with one or more representative examples in the literature. At last, the article comments on the merits, challenges, and opportunities of electrochemical technologies in terms of synthesizing nano-/microstructured materials for electrochemical energy storage.

2 Fundamentals of Electrochemical Synthesis Techniques

Cyclic voltammetry, galvanostatic deposition, potentiostatic deposition, pulse deposition, and electrophoretic deposition constitute the most widely and extensively investigated and practiced electrochemical synthesis techniques for nano-/microstructured materials as supercapacitor electrodes. These processes are typically carried out in electrolytic cells powered by electrochemical workstations. Based on the number of electrodes involved, the setup for electrochemical synthesis is categorized into two types: two-electrode (Fig. 1a) and three-electrode (Fig. 1b) configurations

[30]. The two-electrode configuration contains a positive electrode and a negative electrode that are both immersed in electrolytes. An electrochemical workstation or power source provides voltage across the two electrodes. Therefore, the measured voltage in this scenario is the overall cell voltage. The three-electrode system comprises a working electrode (WE), a counter electrode (CE), and a reference electrode (RE). Ideally, current flows only between WE and CE, and the voltage of WE is referenced to that of RE. Saturated calomel electrode (SCE), Ag/AgCl, and Hg/HgO electrodes with their nearly constant half-reaction potentials are common REs. REs are placed in vicinity to WEs to minimize iR drop and voltage fluctuation due to electrolyte resistance [31]. The measured voltage in three-electrode configurations is the real-time potential of WEs.

2.1 Cyclic Voltammetry (CV)

Besides a conventional electrochemical technique for probing electrochemically redox activities [32], CV serves as a synthetic tool. It linearly scans potential within a range, termed potential window, and simultaneously records

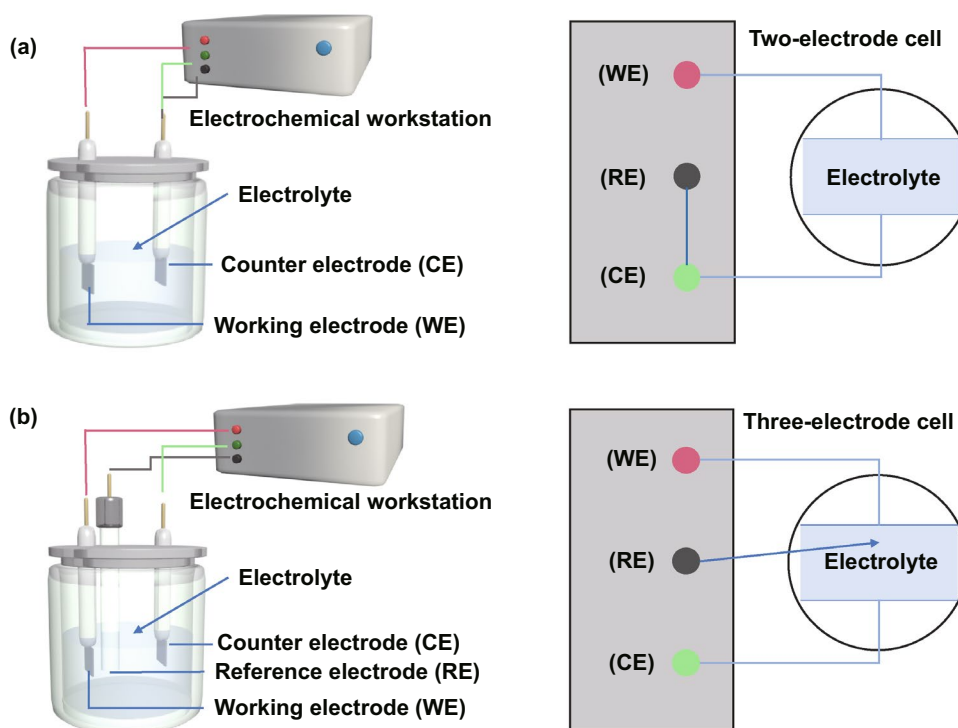


Fig. 1 Schemes illustrating the experimental setups of **a** two-electrode and **b** three-electrode electrolytic cells for electrochemical syntheses

current as a response [33]. Increasing the applied potential, the forward scan oxidizes species in electrolytes or on electrodes and produces anodic current. Conversely, the backward scan decreases the applied potential, reduces active components, and generates a cathodic current.

CV has three main advantages as a synthetic approach. First, it allows for determining the onset potential of an electrodeposition reaction. Oxidation or reduction reactions involving charge transfer across the electrolyte–electrode interfaces will display sharp increases or well-defined peaks in the current. Since the onset potential is the minimum voltage needed to initiate electrodeposition reactions, CV is useful for developing experimental protocols. Second, the potential linear scan of CV is beneficial for growing uniform and conformal films. This characteristic provides a gradient driving force for deposition: Deposition will only begin until the potential is scanned above the onset potential, and the driving force of deposition scales linearly with the potential gradually elevated away from the onset potential. This gradient driving force of CV adjusts the deposition rate and avoids consistently high deposition voltages that can lead to overgrowth of materials, rapid clogging of pores, and/or uneven deposition of films. Third, CV is suitable for synthesizing materials with multiple valence states, e.g., transition metal oxides. For example, deposited by CV within a potential range between -1.5 and 1.5 V vs. SCE in a 0.1 M VOSO_4 aqueous electrolyte, vanadium oxide nanorods contained $\sim 50\%$ V_5O_{12} (a mixture of V^{5+} and V^{4+}) and $\sim 50\%$ VO_2 [34]. The high valence state, V^{5+} , formed during the anodic or forward scan, while the as-deposited V_5O_{12} was partially reduced to VO_2 in the subsequent cathodic or backward scan. These redox processes were documented by the broad peaks in the corresponding CV curve (Fig. 2). Compounds with multivalent species reportedly possess augmented capacitance [35], improved rate capability [34, 36], as well as enhanced cycling stability [37, 38] compared to their monovalent counterparts.

2.2 Potentiostatic (Constant Voltage) Deposition

Potentiostatic deposition synthesizes materials by applying a constant potential across the positive and negative electrodes (two-electrode system) or between the working and counter electrodes (three-electrode system). The deposition potential is maintained constant by an electrochemical workstation

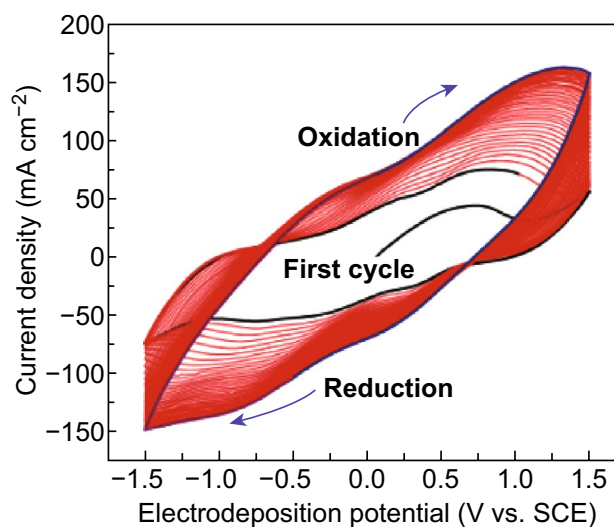


Fig. 2 CV curves of the deposition of mixed-valence vanadium oxide nanorods

(Fig. 3a), and the current is recorded as a function of time (Fig. 3b) [39]. Based on the difference between applied and thermodynamic equilibrium potentials, potentiostatic deposition is categorized into underpotential deposition (UPD) and overpotential deposition (OPD) [40, 41].

UPD happens at potentials below thermodynamic equilibrium potentials. For example, metal deposition can initiate at potentials smaller than the corresponding equilibrium reduction potentials, due to the lower work function of the deposited metal than that of the substrate metal, as described by the Kolb–Gerischer equation [42]:

$$\Delta E = 0.5\Delta\phi \quad (1)$$

where ΔE is the downshift of deposition potential (in V) and $\Delta\phi$ is the difference in the work functions between the deposited and substrate metals (in eV). The coefficient 0.5 (in V eV^{-1}) comes from a linear fitting involving 21 metal–metal couples [42]. UPD involves adsorption, nucleation, and growth processes determined by surface characteristics of substrates (e.g., chemical composition, crystal structure, morphology, and electrolyte wettability) and ion–substrate interactions. Besides, the types of cations in electrolytes and anions strongly influence the structure and properties of the deposited materials, as well as deposition kinetics [43–45]. One example is the UPD of Cu on Au(111) facets in aqueous sulfuric acid solutions [46]. The deposition was much slower under $\text{pH} = 2$ than $\text{pH} = 4$. This discrepancy in the deposition rate was correlated with the different anions under different pH values. Increasing the solution

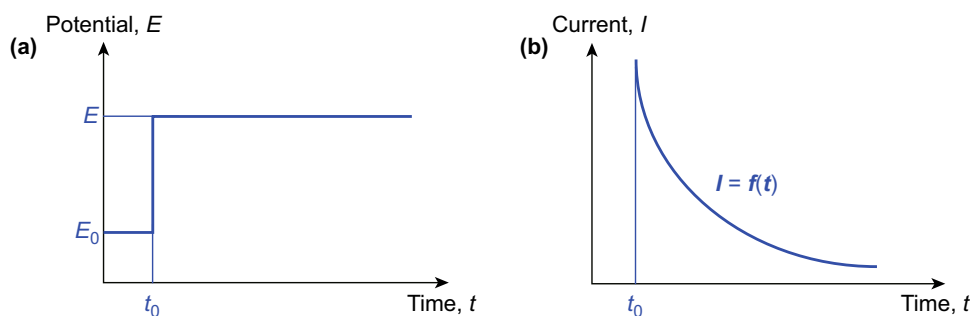


Fig. 3 **a** Constant potential applied in potentiostatic deposition; E_0 and E are the open-circuit potential and the applied potential; t_0 marks the starting time of deposition. **b** Corresponding current as a function of time

acidity converted bisulfate ions to sulfate ions. The latter adsorbed much more strongly than the former on the gold substrate, which blocked some active sites for deposition and hence decelerated the UPD.

OPD occurs in potentials above thermodynamic equilibrium potentials [39, 47]. The structure and properties of the OPD deposits highly depend on various factors, including overpotential (the difference between applied and equilibrium potentials), electrolyte concentration, growth mechanism and deposit–substrate interactions [41]. Notably, diffusion-controlled nucleation is often the rate-determining step of OPD, while that of UPD is the deposit lattice incorporation into substrate [46].

2.3 Galvanostatic (Constant Current) Deposition

Galvanostatic deposition refers to electrodeposition with constant currents between the positive and negative electrodes in a two-electrode system, or between the working electrode and counter electrode in a three-electrode setup (Fig. 4a) [39]. The recorded response is the time-dependent potential of the cell (two-electrode) or the working electrode (three-electrode). The $V-t$ curves (Fig. 4b) sometimes are called polarization curves. Unlike potentiostatic deposition that can start the moment when potentials are applied, galvanostatic deposition needs a short period to begin [48, 49]. It is because that some applied current needs to charge electrical double layers (EDLs) first. After potential reaches certain thresholds (usually equilibrium potentials plus overpotentials), electrochemical reactions occur. Therefore, the applied constant current (I) is contributed from two components:

$$I = I_{DL} + I_{ct} \quad (2)$$

where I_{DL} is capacitive current for charging EDLs and I_{ct} is charge transfer current for electrodeposition. I_{DL} rapidly approaches zero when electrodeposition starts.

$V-t$ curves of galvanostatic deposition contain essential information on electrodeposition chemistries. Since EDL charging time is on the order of milliseconds, $V-t$ curves collected on the timescale of minutes or hours are almost contributed from electrodeposition. For example, the $V-t$ curves of manganese dioxide (MnO_2) deposition processes at different temperatures qualitatively elucidate the nucleation kinetics (Fig. 4d) [50]. The increased potentials at the beginning of the electrodeposition corresponded to the nucleation of MnO_2 as nucleation demanded more energy than its growth to surmount the activation energy barrier. Increasing temperature from 25 to 60 °C offered the additional electrodeposition energy to enable the MnO_2 deposition at the reduced deposition potentials. The prolonged nucleation process at 25 °C results in dense manganese oxide nanosheets.

2.4 Pulse Electrodeposition

Pulse electrodeposition technique deposits materials by applying pulses of potential or current, i.e., a series of pulses with equal polarization, amplitude, and duration, separated by periodic zero current or open-circuit potentials (Fig. 5) [39, 51]. Each pulse has “on” periods when the current or potential is applied and “off” periods with no current or potential (Fig. 5) [52–54]. During the “off” periods, ions in electrolytes diffuse into electric double layers along the surfaces of the deposition substrates, which is beneficial to obtain the uniform deposition of fine-grained deposits during “on” periods [55–57].

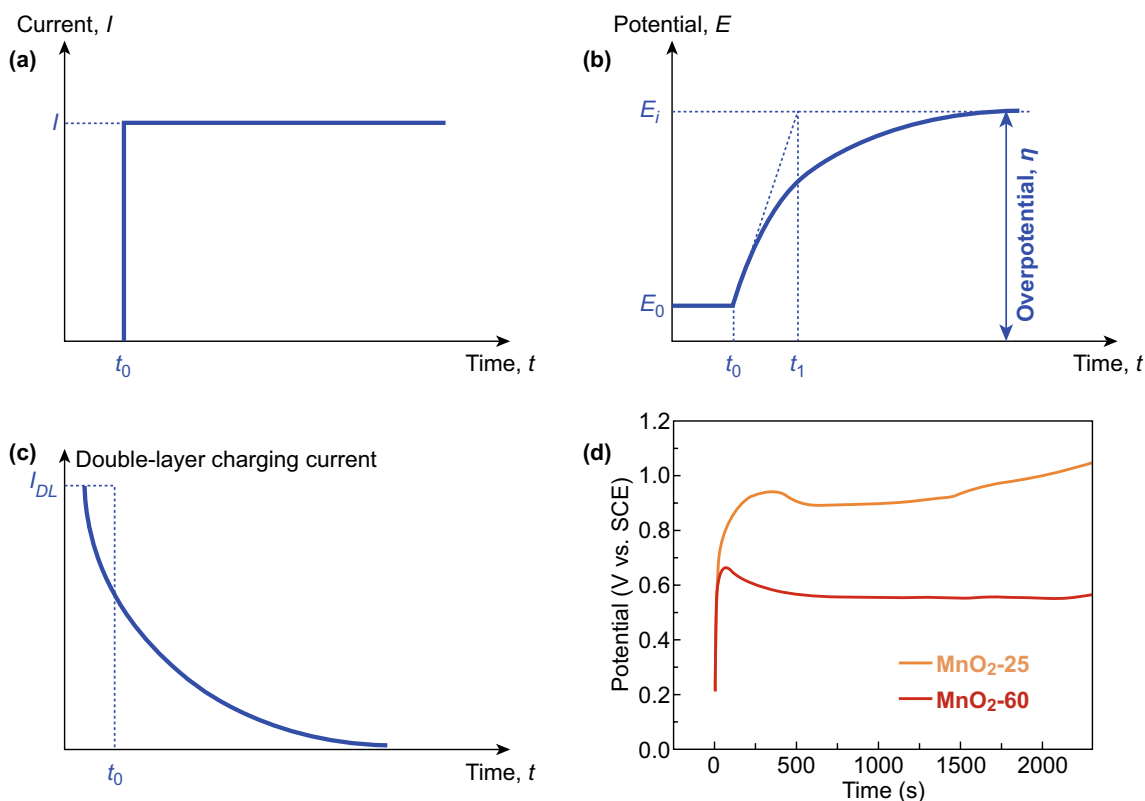


Fig. 4 **a** Constant current applied during a galvanostatic deposition; t_0 represents the moment when current is applied. **b** Potential response as a function of time in a galvanostatic deposition; E_0 and E_i are the equilibrium potential and maximal potential of a working electrode during galvanostatic deposition, respectively. **c** Double-layer charging current (I_{DL}) decays exponentially with time. **d** Time evolutions of the potential during galvanostatic depositions of MnO_2 at temperatures of 25 °C (orange) and 60 °C (red). Adapted from Ref. [50] with permission. (Color figure online)

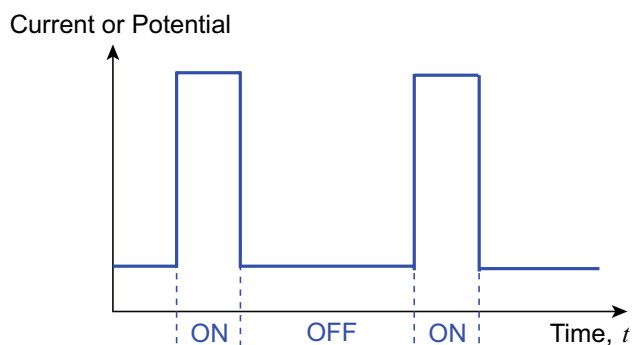


Fig. 5 Current or potential signals applied in pulse electrodeposition

Using pulsed electrodeposition, Yu et al. synthesized flexible graphene/polypyrrole composite films as pseudocapacitor electrodes [57]. The “off” period allowed pyrrole monomers to diffuse into the intersheet spaces of graphene and then electropolymerized into uniform polypyrrole coatings over the “on” periods. By contrast, the continuous, unpulsed electrodeposition triggered the fast polymerization

of pyrrole near the graphene sheets. Since there are no “off” periods to replenish pyrrole monomers near graphene surfaces, the lowered reactant concentration led to scattered polypyrrole particles on the graphene surface. This work highlights the suitability of pulse electrodeposition in coating uniform films onto irregularly shaped substrates.

2.5 Electrophoretic Deposition

Electrophoretic deposition (EPD) differs from all the above-discussed techniques. First, the charge carriers in EPD are suspending, charged colloidal particles, not ions. Second, EPD involves electrostatic attractions between the particles and substrates, but no charge transfer. Third, unlike electrodeposition that demands electrolytes to conduct ions, EPD can perform in poorly conductive media, e.g., water [58, 59].

Depending on charges carried by the colloidal particles, EPD is classified into cathodic and anodic EPD. The

cathodic EPD refers to the deposition of positively charged particles onto negatively charged substrates (Fig. 6a), whereas anodic EPD proceeds in a reverse manner (Fig. 6b) [58]. The structures of the deposits are tailorable by varying parameters of applied potential, particle concentration, and deposition duration [60–65]. Notably, the stoichiometry of the electroadsorbed particles directly determines the stoichiometry of the deposit [59].

3 Electrochemically Synthesized Carbon Materials

Carbon materials, including activated carbon, carbon fibers, carbon aerogels, carbon nanotubes, and graphene, are conventional materials in electrical double-layer capacitors [17]. Their high electrical conductivity, large surface areas, cost-effectiveness, chemical inertness, and tailorable porous structures make them suitable electrode candidates [66, 67]. The two outstanding advantages of carbon electrodes are their exceptional rate capability and ultralong lifetimes. Electrochemical approaches have been widely used to produce carbon materials [68–70]. The following sections first present the recent progress in syntheses of graphene (Sect. 3.1) and 3D carbons (Sect. 3.2), the two carbon materials that have been prepared by electrochemical technologies. Their applications in supercapacitors are highlighted separately in Sect. 3.3.

3.1 Graphene

Electrochemical exfoliation is a facile method for synthesizing graphene. Compared with chemical exfoliation,

electrochemical exfoliation avoids chemical treatments that can introduce unwanted species, simplifying product purification [66, 71]. Electrochemically exfoliated graphene often maintains more sp^2 -hybridized carbon networks than that made by chemical oxidation. Additionally, the graphene surface functionalization often accompanies with exfoliation [72, 73], and the heteroatom doping level is highly controllable. Another strength of electrochemical exfoliation is its high efficiency. It only needs minutes or hours, depending on applied potentials, electrolyte compositions, and graphite sources, to produce grams of graphene sheets in laboratories [74, 75].

According to the potential polarity, electrochemical exfoliation is classified into (1) anodic exfoliations performed in aqueous electrolytes containing inorganic salts [76], mineral acids [77, 78], ionic liquids [79], or their mixtures [67, 80]; and (2) cathodic exfoliations in organic electrolytes having lithium or alkylammonium salts [21, 67, 81–83].

3.1.1 Anodic Exfoliation

Anodic exfoliation separates graphite into graphene by anion intercalation [73, 76]. It is the most used electrochemical approach for graphene production due to its high exfoliation efficiency. With inorganic acids (e.g., H_2SO_4 [78, 84], HNO_3 [85, 86], and H_3PO_4 [87]) or salts (e.g., KNO_3 [88] and $(NH_4)_2SO_4$ [89]) as supporting electrolytes, a high exfoliation potential (e.g., 3–10 V) can generate single-layer or multilayer graphene sheets from graphite. For example, Parvez et al. exfoliated graphite foils in sulfuric acid aqueous solutions with concentrations of 0.1, 1, and 5 M [84].

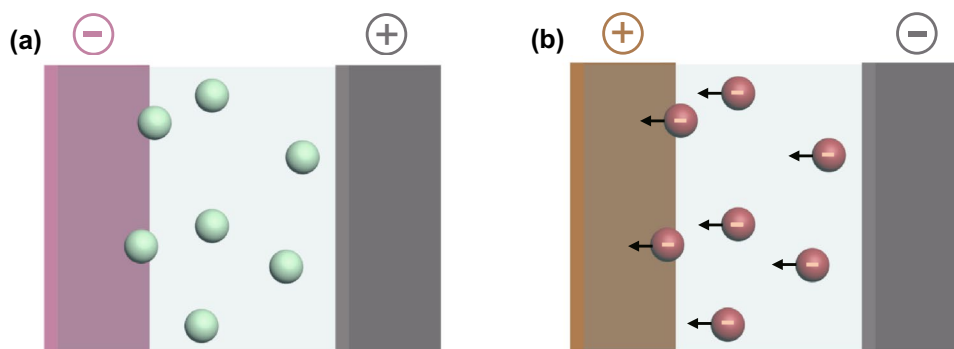


Fig. 6 Schematic illustrations of **a** cathodic and **b** anodic electrophoretic deposition. Only ions of interest are shown for brevity

The synthesis procedures involved multiple steps (Fig. 7a). First, a high potential of 10 V was applied across a graphite positive electrode and a Pt negative electrode (Fig. 7b), splitting water into hydroxyl ($\text{OH}\cdot$) and oxygen radicals ($\text{O}\cdot$). These radicals preferentially oxidized the boundaries and defects of graphite, opening its edges. Second, driven by the applied electrical field, sulfate ions (SO_4^{2-}), together with water molecules, intercalated into graphite layers through the open edges and expanded graphite layers. Meanwhile, oxygen gas evolution in between graphite layers further torn apart graphite sheets and dispersed exfoliated graphene layers into electrolytes (Fig. 7c–e). Water in the electrolytes was critical for electrochemically exfoliation, as it both generated $\text{OH}\cdot$ and $\text{O}\cdot$ (the exfoliation initiators) and served as an intercalant. The exfoliation efficiency in the 0.1 M H_2SO_4

electrolyte reached the highest, since the 5 M H_2SO_4 electrolyte overexfoliated graphite into graphitic particles, while the 0.1 M H_2SO_4 electrolyte led to incomplete exfoliation due to insufficient sulfate ions. The obtained graphene sheets in 0.1 M H_2SO_4 had a high yield of > 80%, less than three layers, a high C/O ratio of 12.3, and good electrical conductivity (sheet resistance of $\sim 4.8 \text{ k}\Omega/\square$), all of which are comparable to those of high-quality graphene sheets synthesized by chemical vapor deposition.

Changing the water content of non-aqueous electrolytes can yield graphene-based materials with different surface areas and morphologies. Specifically, Lu et al. found that the morphologies of the exfoliation products in 1-methyl-3-butylimidazolium tetrafluoroborate, an ionic liquid (IL), depended on the water-to-IL ratio [79]. Identical to

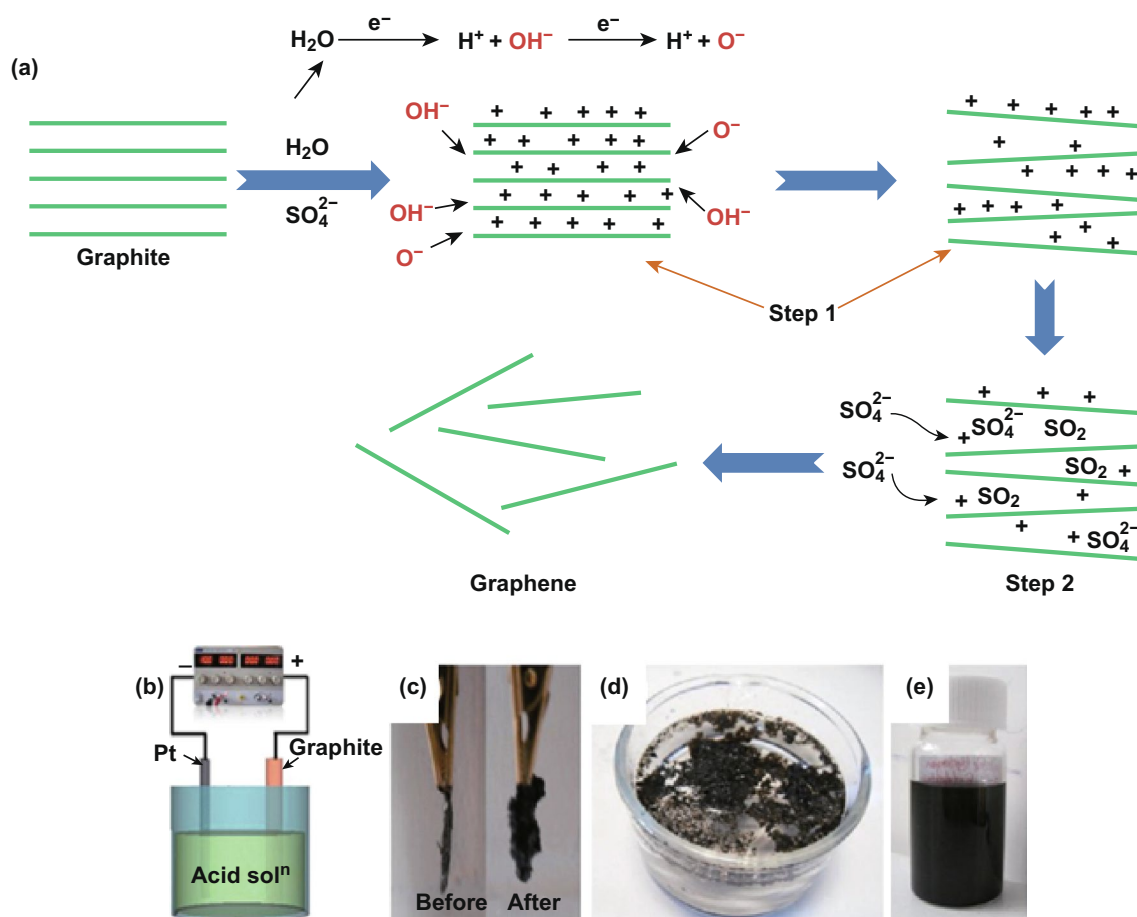


Fig. 7 a Schemes of the microscopic processes of graphite exfoliation in H_2SO_4 aqueous electrolytes. Step 1: edge opening by waterborne radicals; Step 2: SO_4^{2-} intercalation and exfoliation. b Experimental setup for the graphite exfoliation. c Photographs of the exfoliated electrodes before and after exfoliation. d Exfoliated graphene floating on an electrolyte. e Dispersed graphene sheets in dimethylformamide solution. Adapted from Ref. [84] with permission

electrochemical exfoliations in aqueous solutions, water in the IL produced $\text{OH}\cdot$ and $\text{O}\cdot$ to drive the exfoliation process, while subsequent intercalation of BF_4^- promoted complete exfoliation. Decreasing the water/IL ratio favored BF_4^- intercalation that significantly expanded graphite into graphene nanoribbons. Increasing the water/IL ratio increased the populations of $\text{OH}\cdot$ and $\text{O}\cdot$, which substantially oxidized and broke graphite into hydroxylated carbon particles. In this case, the oxygen-containing radicals acted as electrochemical “scissors” that cut the graphite plates into nanoribbons or nanoparticles.

Graphite exfoliation in aqueous solutions often yields oxygenated graphene with reduced electrical conductivity, a property unfavorable for rapid charge storage [36, 80, 90–94]. To circumvent this shortcoming, a variety of additives, including reducing agents [95] and oxygen radical scavengers [76], have been introduced into electrolytes to prevent overoxidation of exfoliated graphene. For example, Yang et al. demonstrated that (2,2,6,6-tetramethylpiperidin-1-yl)oxyl (TEMPO), ascorbic acid, and sodium borohydride could consume radicals. This characteristic kept oxygen content at low levels (3.8 atom% O of TEMPO-added exfoliated graphene vs. 11 atom% O of TEMPO-free exfoliated graphene) [95]. Besides, Ejigu et al. reported that transition metal ions (e.g., Co^{2+} , Ni^{2+} , Fe^{3+} , Mn^{2+} , Ru^{3+} , Ir^{3+} , and V^{3+}) as electrolyte additives were conducive to acquiring high-quality graphene because they scavenged oxygen radicals [76]. Among all these ions, Co^{2+} was the most promising one because it converted to an oxygen evolution reaction catalyst. During anodic exfoliation, Co^{2+} was first oxidized to Co^{4+} , an active species for oxygen evolution. The Co^{4+} adsorbed on graphite facilitated oxygen evolution from water, bypassing the formation of oxygen radicals that oxidized exfoliated graphene. The lowest oxygen content was 2.6%.

3.1.2 Cathodic Exfoliation

Cathodic exfoliation, which produces graphene by applying negative biases to graphite, is a method free of oxidation concerns. Though this technique is not as developed as anodic exfoliation, it has successes in graphite exfoliation in organic-based electrolytes [21, 67, 81, 83] and molten salts [82]. For example, Wang et al. deployed a cathodic exfoliation method that acquired highly conductive, less than

five layers of graphene nanosheets from graphite with yields of $> 70\%$ [21]. At a high cathodic potential of -15 ± 5 V, Li^+ -propylene carbonate (PC, a solvent) complexes intercalated into graphite and expanded graphite layers. Subsequently, the reduction of PC molecules liberated gas bubbles in between graphite layers, eventually exfoliating graphite into graphene sheets (Fig. 8a–c). Because the exfoliation involved no oxidation, the resultant graphene contained little defects, as evidenced by the small I_D/I_G ratio of 0.1 revealed by Raman spectroscopy (Fig. 8d).

In addition to liquid electrolytes, quasi-solid molten salts were potent electrolytes for graphite exfoliation. For instance, Huang et al. successfully exfoliated graphite in molten LiOH with a high cathodic current of 15 A [82]. This process was based on intercalation, expansion, and micro-explosion. First, Li^+ ions in the molten LiOH intercalated into graphite layers and widened the interlayer gap of graphite, forming graphite intercalation compound (Li_xC_y). Afterward, the Li^+ -intercalated graphite was soaked in water. Li_xC_y and metallic Li reacted violently with water (micro-explosion), creating hydrogen gas bubbles that further exfoliated graphite into graphene. The conversion efficiency was $\sim 80\%$.

3.2 Three-Dimensional Carbons

As supercapacitor electrodes, three-dimensional (3D) carbon materials have advantages over other conventional carbon powders (e.g., activated carbon) and graphene. First, their self-standing nature requires no binder blending for preparing electrodes, which eases fabrication and reduces the negative impact of the binders on electron transport. Second, their tailorable structures offer opportunities to achieve both high surface areas and hierarchical porous networks known to facilitate ion diffusion [4, 96–102].

Electrochemical partial exfoliation of graphitic materials is the most common synthesis method of electrochemically synthesizing 3D carbon materials. As indicated by its name, electrochemical partial exfoliation only partially exfoliates graphitic precursors, e.g., carbon fibers [37, 85, 97, 99], graphene aerogels [99], and graphite foils [88, 103, 104], leading to graphene sheets anchored on the exposed surfaces. For example, Song et al. demonstrated a two-step electrochemical partial exfoliation method to prepare oxygen-functionalized, partially exfoliated graphite foils (Fig. 9a)

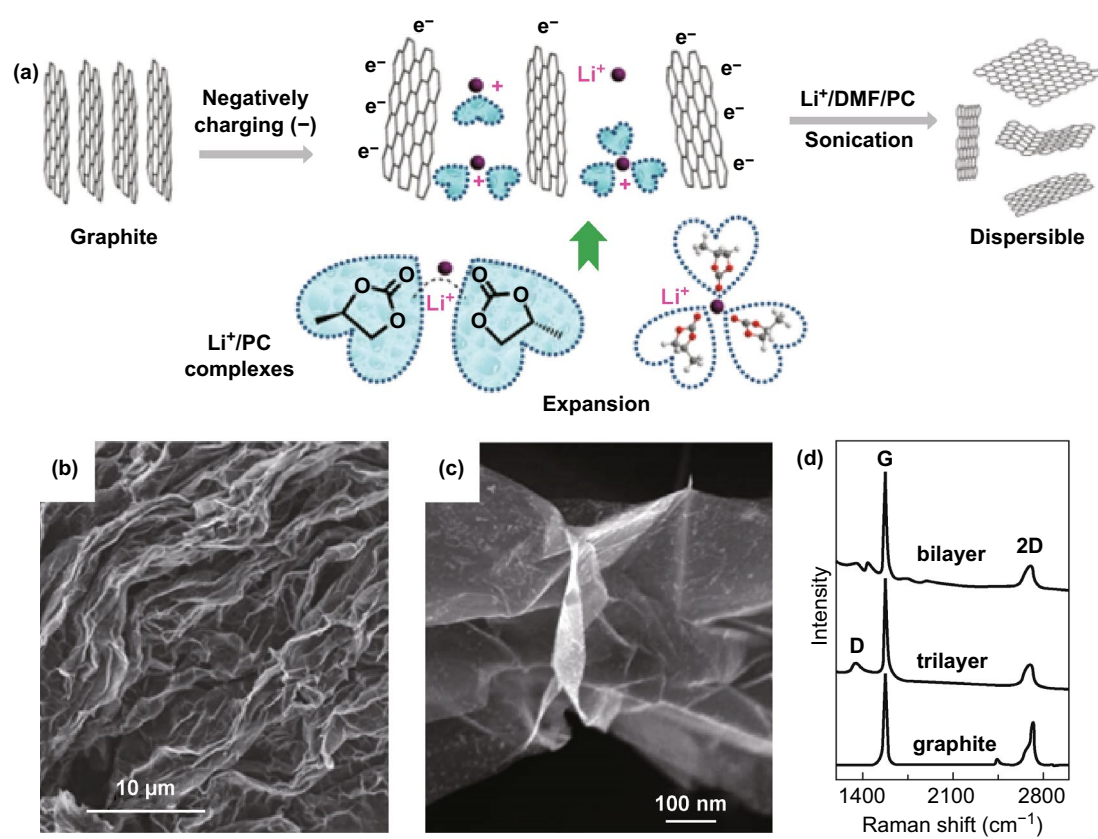


Fig. 8 **a** Schematic illustration of cathodic exfoliation of graphite by intercalation of Li^+ complexes. **b**, **c** SEM images of the cathodically exfoliated graphene plates. **d** Raman spectra of the cathodically exfoliated graphene with bilayers and trilayers, in comparison with that of pristine graphite. Adapted from Ref. [21] with permission

[88]. The authors first scanned a piece of graphite foil (EG in Fig. 9b) in aqueous K_2CO_3 electrolytes by cyclic voltammetry. This step partially exfoliated the graphite layers on and near the outer surface of EG through vigorous gas evolution from water splitting (Fig. 9c). The secondary exfoliation process intercalated NO_3^- into EG through the open edges and defects formed during the first step, forming graphite intercalation compounds ($\text{C}-\text{NO}_3$). These compounds, when placed in water, hydrolyzed and released oxygen gas. The gas evolution further exfoliated and oxygenated the top layers of EG (Fig. 9d). The introduced oxygen functionalities rendered the foil superhydrophilicity as reflected from the zero contact angle (Fig. 9d inset). The potential applied in the second step controlled the degrees of the exfoliation and oxygenation. The functionalized, exfoliated EG possessed a 3D network consisting of oxygenated graphene sheets integrated onto graphite foil. The seamless integration between the top layer and the graphite bottom ensured fast electron conduction pathways. Besides improving electrolyte

wettability, the oxygen moieties served as anchoring sites for depositing guest materials for polyaniline [27], polypyrrole [105], manganese oxides [86], vanadium oxides [37], iron oxides [35, 106], nickel–cobalt double hydroxides [106], and molybdenum-based materials [28].

In addition to graphite, carbon fibers can also be partially electroexfoliated. For example, Wang et al. synthesized electrochemically activated carbon fiber cloth electrodes by applying a voltage of 3 V in $\text{HNO}_3/\text{H}_2\text{SO}_4$ mixed aqueous electrolytes [85]. The high voltage, together with the highly oxidative and corrosive acids, roughened the carbon fiber surfaces and introduced functionalities of $\text{C}-\text{OH}$, $-\text{C}=\text{O}$, and $-\text{COOH}$. This activated carbon cloth electrode exhibited a high areal capacitance of 756 mF cm^{-2} at 6 mA cm^{-2} . Song et al. demonstrated an acid-free method to exfoliate carbon fiber cloth partially [37]. First, NO_3^- anions intercalated into carbon fibers, exfoliating and oxidizing the outer surface (Fig. 9e). To recover the electrical conductivity of carbon fibers, the researchers immersed the oxidized carbon

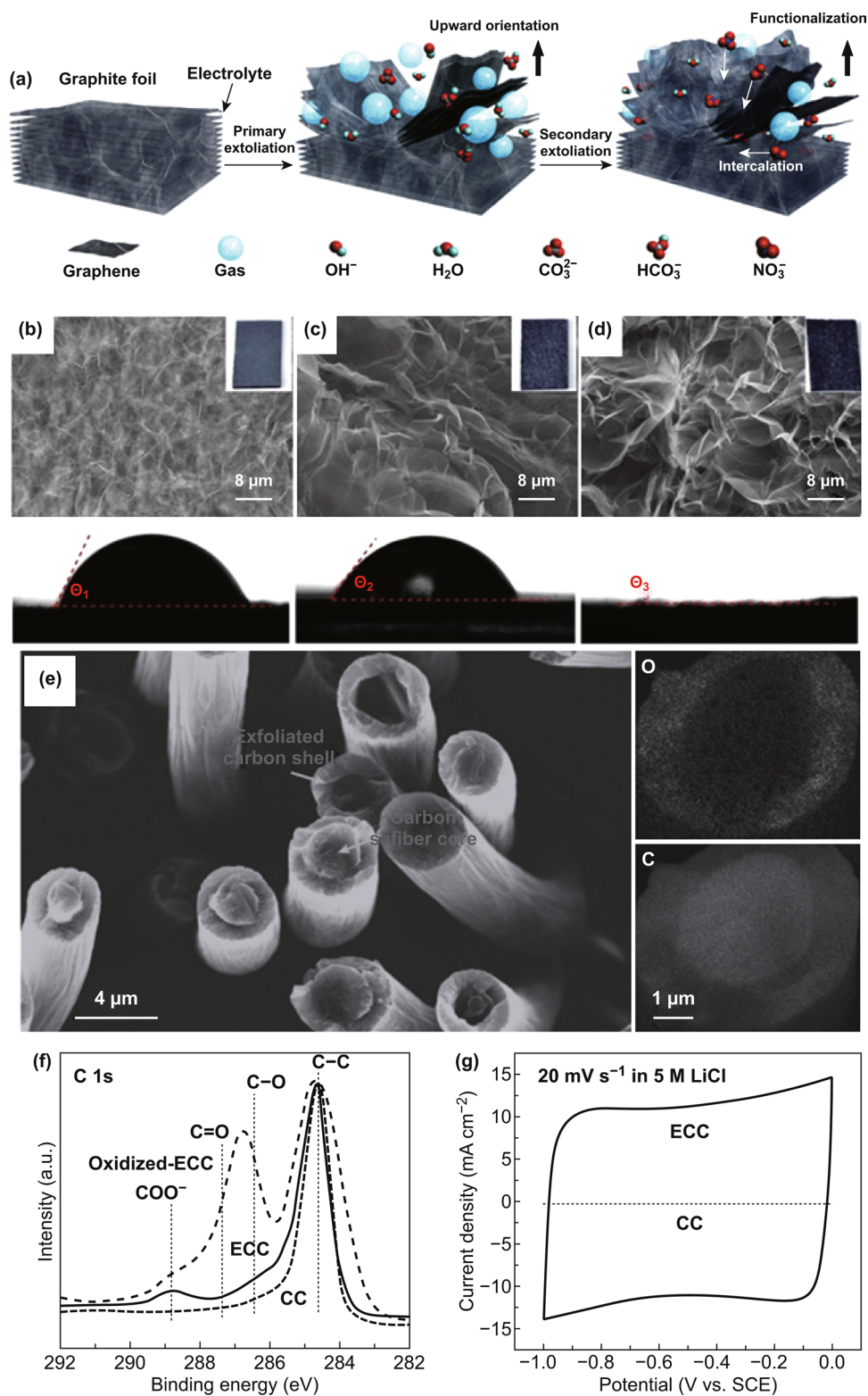


Fig. 9 **a** Schemes of the two-step partial exfoliation of graphite foil. **b–d** SEM images and contact angles of **b** graphite foil, **c** graphite foil after primary exfoliation, and **d** graphite foil after secondary exfoliation. Insets: photographs of graphite foil at different treatment stages. **e** SEM image and EDS element mappings (C and O) of the cross sections of exfoliated carbon cloth fibers. **f** XPS C 1s spectra of pristine carbon cloth (CC) and exfoliated carbon cloth (ECC). **g** CV curves of CC and ECC. Adapted from **a–d** Ref. [88] and **e–g** Ref. [37] with permission

cloth in a 0.1% hydrazine hydrate aqueous solution to reduce the oxygen content. This reduction process removed most of the oxygen functionalities (Fig. 9f) and resulted in enhanced capacitive performance (Fig. 9g). The partially exfoliated carbon cloth electrode exhibited a high areal capacitance of $\sim 500 \text{ mF cm}^{-2}$ at 20 mA cm^{-2} .

3.3 Application for Supercapacitors

Owing to the enhanced surface areas and high electrical conductivity, electrochemically exfoliated graphene-based materials or activated carbon fibers have functioned as either electrode materials or current collectors in supercapacitors. Liu et al. fabricated an in-plane micro-supercapacitor through directly printing electrochemically exfoliated graphene on patterned microelectrodes. This micro-supercapacitor delivered an areal capacitance of $800 \mu\text{F cm}^{-2}$ at 1 mV s^{-1} [107]. Wu et al. used electrochemically exfoliated graphene to prepare graphene paper and 3D graphene foams as supercapacitor electrodes [75]. The specific capacitance of the 3D graphene electrode reached 113.2 F g^{-1} and 58.9 F g^{-1} at 0.5 A g^{-1} in 6 M KOH aqueous and 1 M triethylmethylammonium tetrafluoroborate acetonitrile (TEMABF₄/AN), respectively.

Besides reporting the outstanding electrochemical performance, some researchers devoted to revealing the interplays between exfoliation conditions and electrochemical properties. Ambrosi et al. compared the capacitive performances of electrochemically exfoliated graphene synthesized in different aqueous electrolytes, i.e., 0.5 M H₂SO₄, Na₂SO₄, and LiClO₄ [71]. The results showed that the graphene prepared in H₂SO₄ and Na₂SO₄ exhibited relatively high specific capacitance of 78 and 106 F g⁻¹, respectively. LiClO₄ introduced a large amount of oxygen functional groups on the exfoliated graphene, which could be anchoring sites for growing other materials to form graphene-based composites. Notably, the specific capacitances of the electrochemically exfoliated graphene often fall in the range of 50–100 F g⁻¹, which are slightly lower than those of graphene obtained through chemical oxidation. The underlying reason was revealed by Xia et al., who studied the different graphite exfoliation routes via chemical oxidation and electrochemical exfoliation [66]. The authors discovered that the surface area of the electrochemically exfoliated graphite was only $6.6 \text{ m}^2 \text{ g}^{-1}$, which was three orders of magnitude lower than

that of the theoretical value ($2600 \text{ m}^2 \text{ g}^{-1}$) of a graphene monolayer achieved by chemical exfoliation. Therefore, electrochemical exfoliation is challenging to fully separate graphite into monolayer graphene, resulting in the relatively low gravimetric capacitance due to the small surface area (Table 1). This limitation has motivated the introduction of pseudocapacitive functional groups to boost capacitance [85, 99, 101].

Compared with fully exfoliated graphene sheets, partial exfoliated graphite and carbon electrodes have the main advantage that the whole electrodes remain structurally and electrically connected, enabling them to function as current collectors for loading pseudocapacitive materials. The resultant composite materials possess both high capacitance from the incorporated pseudocapacitive materials and the excellent rate capability characteristic of carbon-based materials. In this regard, the mass loadings of the pseudocapacitive materials must be meticulously tuned to ensure the highest specific capacitance without significantly compromising the rate capability.

4 Conducting Polymers

Conducting polymers, or conjugated polymers, are organic polymers that conduct electricity in their electron conjugated networks in the polymer backbones [116–118]. Polyaniline (PANI) [119–122], polypyrrole (PPy) [105, 123], polythiophene (PTh) [124, 125], and poly(3,4-ethylene dioxythiophene) (PEDOT) [126–129] are common supercapacitor electrode materials. In terms of electrochemical synthesis, electrochemical polymerization of monomers is typical to prepare these conducting polymers. It grows conducting polymers onto electrically conductive substrates (current collectors), eliminating the need for blending powdered materials with binders and conductive additives when preparing electrodes. Potentiostatic deposition [130], galvanostatic deposition [131, 132], and cyclic voltammetry [105] are synthesis techniques of conducting polymers. The thicknesses and mass loadings of conducting polymers are controllable by tuning deposition duration. The compositions of electrolytes mainly influence their electrical conductivity. This section summarizes the mechanisms of electrochemical polymerization, recent progress of the electrochemically synthesized conducting polymers, and their electrochemical performance as supercapacitor electrodes.

Table 1 Synthesis conditions and specific capacitance of electrochemically exfoliated graphene-based electrodes

Material ^a	Method	Exfoliation electrolyte ^b	Specific capacitance	Current density/scan rate
Exfoliated carbon cloth [85]	Anodic exfoliation	HNO ₃ /H ₂ SO ₄	756 mF cm ⁻²	6 mA cm ⁻²
Exfoliated carbon fibers [102]	Cathodic exfoliation	0.1 M TMAClO ₄ /NMP	64.5 mF cm ⁻²	10 mV s ⁻¹
Partial exfoliation of HOPG [104]	Anodic exfoliation	1 M H ₂ SO ₄	750 mF cm ⁻²	20 mV s ⁻¹
Exfoliated carbon paper [86]	Anodic exfoliation	0.5 M KOH	400 mF cm ⁻²	1 mA cm ⁻²
Trilayer graphite foil [101]	Anodic exfoliation	0.5 M K ₂ CO ₃ /0.5 M KNO ₃ /3 M KCl	820 mF cm ⁻²	5 mA cm ⁻²
Exfoliated carbon cloth [97]	Anodic exfoliation	2 M H ₂ SO ₄	12 mF cm ⁻²	1 mA cm ⁻²
Exfoliated graphitic paper [99]	Cathodic and anodic exfoliation	1 M LiClO ₄ /propylene carbonate	108.8 mF cm ⁻²	0.5 mA cm ⁻²
Exfoliated 3D printed graphene aerogel [99]	Cathodic and anodic exfoliation	1 M LiClO ₄ /propylene carbonate	101.7 F g ⁻¹	10 A g ⁻¹
Vertically oriented graphene nanosheets [98]	Anodic exfoliation	0.5 M H ₂ SO ₄	3.9 F cm ⁻³	7.5 mA cm ⁻³
Exfoliated graphite foils [88]	Anodic exfoliation	0.5 M K ₂ CO ₃ /1 M KNO ₃ in PBS (pH=6.7)	60 mF cm ⁻²	0.23 mA cm ⁻²
Exfoliated carbon cloth [37]	Anodic exfoliation	0.5 M KNO ₃	560 mF cm ⁻²	2 mA cm ⁻²
Graphene [108]	Anodic exfoliation	0.1 M NaI	50 F g ⁻¹	0.1 A g ⁻¹
Graphene [107]	Anodic exfoliation	0.1 M H ₂ SO ₄	5.4 mF cm ⁻²	1 mV s ⁻¹
Graphene [92]	Anodic exfoliation	0.1 M (NH ₄) ₂ SO ₄	56.6 F g ⁻¹	1 A g ⁻¹
Graphene [95]	Anodic exfoliation	0.05 M (NH ₄) ₂ SO ₄ + TEMPO + H ₂ O	11.5 mF cm ⁻²	2 mV s ⁻¹
Graphene [89]	Anodic exfoliation	0.1 M (NH ₄) ₂ SO ₄	11.3 mF cm ⁻²	1 mV s ⁻¹
S-doped graphene [109]	Anodic exfoliation	Na ₂ S ₂ O ₃ + H ₂ SO ₄	320 F g ⁻¹	3 A g ⁻¹
Graphene film [110]	Anodic exfoliation	0.15 M Na ₂ SO ₄ + 0.01 M sodium dodecyl sulfate	900 μF cm ⁻²	10 mV s ⁻¹
Graphene aerogel [111]	Cathodic/Anodic exfoliation	0.2 M H ₂ SO ₄ + KOH	325 F g ⁻¹	1 A g ⁻¹
3D graphene [75]	Anodic exfoliation	10 M H ₂ SO ₄	113.2 F g ⁻¹	0.5 A g ⁻¹
3D N-doped graphene [112]	Anodic exfoliation	CH ₃ COOH/H ₂ SO ₄ (V/V = 4:6)	170.5 F g ⁻¹	10 mV s ⁻¹
Acid modified graphene [113]	Anodic exfoliation	9-anthracene carboxylic acid (1 mg mL ⁻¹)	577 F g ⁻¹	7 A g ⁻¹
Graphene film [114]	Electrophoretic deposition	Graphene oxide suspension (0.6 mg mL ⁻¹)	156 F g ⁻¹	0.15 A g ⁻¹
P-doped graphene [115]	Anodic exfoliation	H ₃ PO ₄	290 F g ⁻¹	1 A g ⁻¹
Graphene [71]	Anodic exfoliation	0.5 M Na ₂ SO ₄	106 F g ⁻¹	0.1 A g ⁻¹
Graphene [71]	Anodic exfoliation	0.5 M LiClO ₄	78 F g ⁻¹	0.1 A g ⁻¹
Graphene [71]	Anodic exfoliation	0.5 M H ₂ SO ₄	21 F g ⁻¹	0.1 A g ⁻¹

^aTMAClO₄: tetramethylammonium perchlorate; NMP: *N*-methyl pyrrolidone; PBS: phosphate-buffered saline; TEMPO: (2,2,6,6-tetramethylpiperidin-1-yl)oxyl

^bUnless specifically stated, solutions are aqueous-based

4.1 Mechanism of Electrochemical Polymerization of Conducting Polymer Materials

Electrochemical technologies are time- and cost-efficient in preparing conducting polymers. Electrochemical polymerization begins with oxidizing monomers possessing

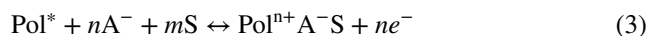
five-membered aromatic heterocycles (e.g., pyrrole or thiophene) [133, 134] or cyclic aromatic amines (e.g., aniline) [116]. The oxidation involves generating and dimerizing radical cations, followed by polymer chain growth. Electrochemical polymerization initiates polymer growth on the surfaces of conductive substrates.



Diaz proposed the widely accepted electrochemical polymerization mechanism of five-membered aromatic monomers in 1983 (Fig. 10a) [133]. Taking polypyrrole (PPy) as an example, pyrrole (Py) monomers are first oxidized to radical cations under an anodic potential. Subsequently, the radical cations dimerize through radical–radical coupling reactions at α -positions and deprotonated into neutral dimers. The as-formed dimers further combine and eventually extend to PPy.

The polymerization of another conducting polymer, polyaniline, follows a similar path as that of PPy (Fig. 10b) [135]. Its monomers are first oxidized to radical cations, then coupled, and deprotonated to dimers. Unlike PPy, whose chain propagation is driven by continuous dimer combination, aniline dimers undergo further oxidation and couple with one aniline radical cation at a time. The coupling extends to polyaniline. For both cases, anions (or counterions in general) will dope into the as-formed conducting polymers to balance the charges carried by the positively charged sites on the polymer backbones. Note that the concept of doping in the context of conducting polymers is fundamentally different from that in conventional solid-state semiconductors. Doping semiconductors means to incorporate dopants into the crystal lattices of the host materials [136].

This counterion doping process maintains the electro-neutrality of conducting polymer and affects the electrical conductivity of conducting polymers [137]:



where Pol^* is the positively charged sites in a conducting polymer, A^- stands for counterion, and S represents a solvent molecule. When electrons enter in conducting polymers, doping of A^- and concurrently co-insertion of solvent molecules lead to volumetric expansion of the host polymers. Conversely, electron extraction causes de-doping of A^- and de-solvation of conducting polymers, resulting in volumetric contraction. The irreversible volumetric deformation is a typical culprit for the structural instability that causes unsatisfactory cycling stability of conducting polymers [138, 139].

4.2 Electrochemically Synthesized Conducting Polymers for Supercapacitors

4.2.1 Films

Conformal films are the most common morphologies of electrochemically polymerized conducting polymer electrodes [97, 140, 141]. Parameters associated with

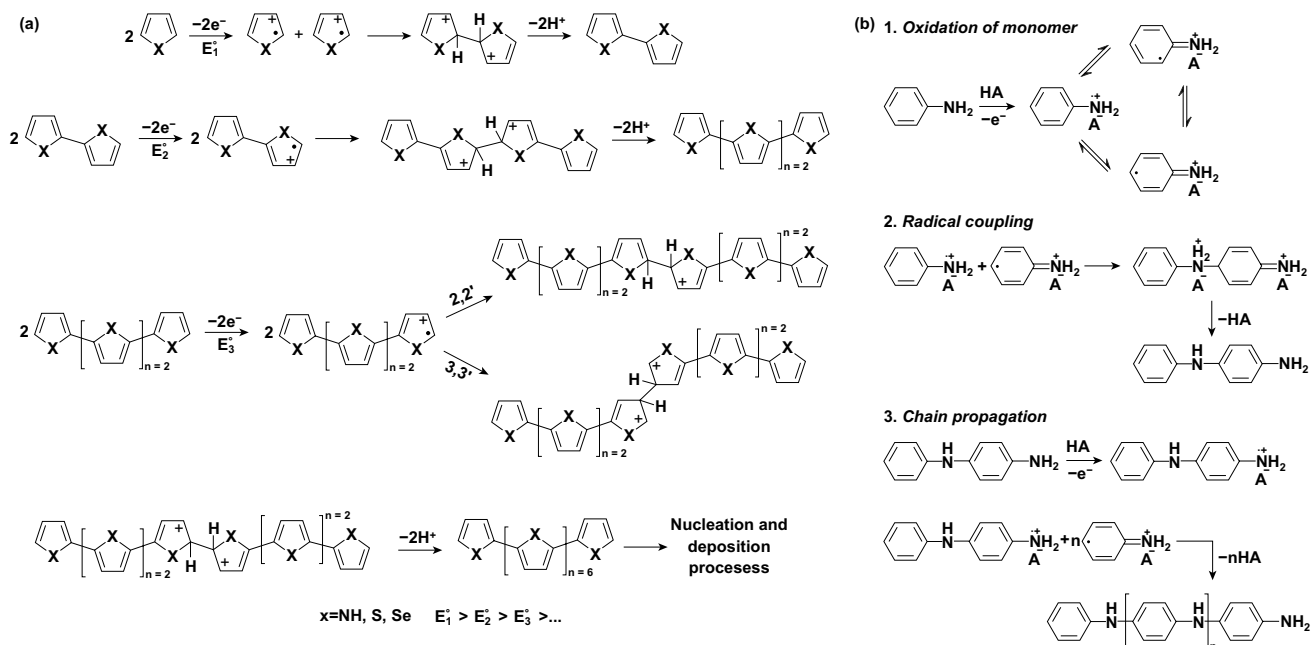


Fig. 10 **a** Electrochemical polymerization mechanism of pyrrole. Adapted from Ref. [133] with permission. **b** Electrochemical polymerization mechanism of polyaniline. Adapted from Ref. [135] with permission

electropolymerization have profound influences on the chemical compositions, morphologies, and electrochemical properties of the deposited polymer films [130, 142].

The surface properties of the substrates influence the adhesion strength and chemical compositions of the polymer films. For example, Feng et al. electrochemically deposited a thin PPy layer on oxygen-functionalized carbon cloth (FCC) [97]. Compared with PPy deposited on pristine carbon cloth (CC), PPy/FCC exhibited enhanced dopant concentrations and electrical conductivity, because the oxygen functional groups on FCC could dope into PPy and reinforced the adhesion of PPy onto FCC. Consequently, PPy/FCC displayed an areal capacitance of 341 mF cm^{-2} at 1 mA cm^{-2} , about 40 mF cm^{-2} higher than that of PPy/CC at the same current density.

Electrochemically polymerized conducting polymer films have different molecular structures from those prepared by chemical polymerization. Huang et al. reported that PPy film deposited via galvanostatic electrodeposition exhibited higher molecular order than that made by chemical oxidation (Fig. 11a) [143]. During electrochemical polymerization, the α - α coupled PPy chains stacked layer by layer with an inter-layer spacing of 3.45 \AA , as evident from the pronounced X-ray diffraction peak (Fig. 11b, c). This layered molecular structure facilitated ion transport within the electrode and

induced a homogeneous stress distribution in the polymer films, both of which improved the cycling stability of PPy.

Coating conducting polymer films onto flexible substrates is a strategy of making flexible electrodes for wearable supercapacitors. Huang et al. demonstrated a stretchable stainless steel mesh as an electrically conductive substrate to endow the deposited PPy film excellent stretchability (Fig. 11d) [132]. The PPy-coated stainless steel mesh delivered a specific capacitance of 170 F g^{-1} at 0.5 A g^{-1} , and the capacitance augmented to 214 F g^{-1} when the electrode was applied a 20% strain. The strain improved the contact between PPy and stainless steel and reduced the contact resistance, which augmented the specific capacitance (Fig. 11e).

It should be noted that thin films are usually obtained at the early stage of electrode polymerization, and prolonging deposition time may modify the film morphology due to overgrowth. For instance, Song et al. observed that instead of thin films, PPy cauliflowers formed (Fig. 11f) after 10 cycles scanning from 0 to 0.8 V vs. SCE at 50 mV s^{-1} [105].

Soft templates (e.g., surfactant) can introduce porosity in electrodeposited conducting polymer films. Kurra et al. used a potentiostatic method to deposit a thin layer of PEDOT on an Au-coated, interdigitated electrode (Fig. 12a,

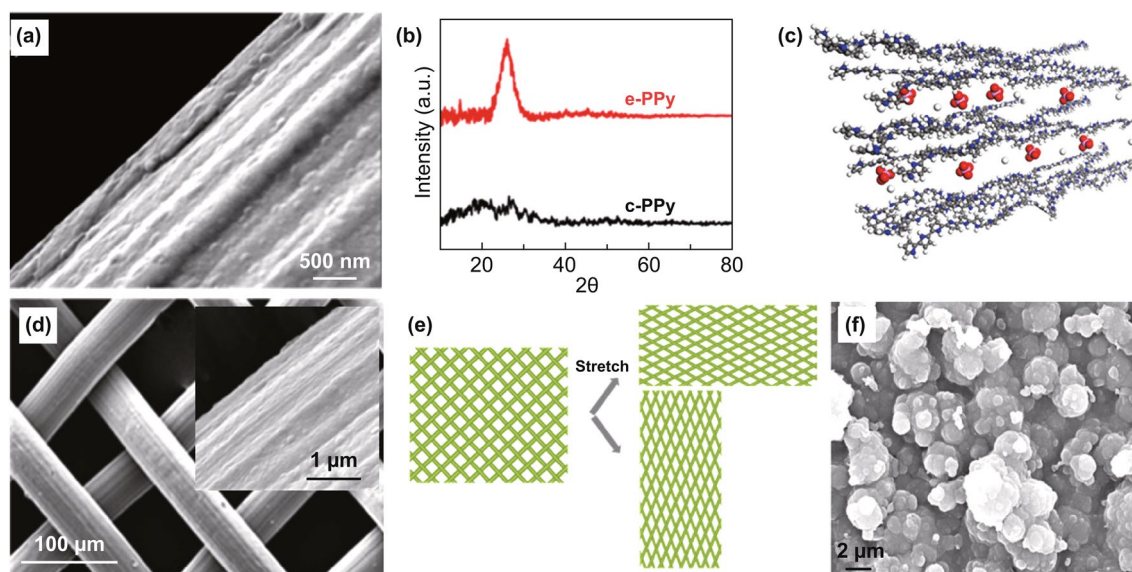


Fig. 11 **a** SEM image of electrodeposited PPy film on an oxygen-functionalized carbon fiber. **b** XRD patterns of electrochemically and chemically deposited PPy. **c** A possible molecular structure of electrodeposited PPy. **d** PPy film electrochemically deposited on a flexible stainless steel mesh. **e** Schematic illustration of the stretched mesh structure. **f** Cauliflower-like PPy film. Adapted from **a–c** Ref. [143], **d, e** Ref. [132], **f** Ref. [105] with permission

b) [144]. Sodium dodecyl sulfate, an anionic surfactant, was used to increase the solubility of 3,4-ethylenedioxythiophene (EDOT) in water and thus decreased the polymerization potential of EDOT. The surfactant molecules also served as soft templates that created cracks in the PEDOT film (Fig. 12c, d). These cracks provided electrolyte ion percolation pathways and benefited rate capability at high frequencies. A symmetric micro-supercapacitor consisting of two identical interdigitated electrodes displayed a typical capacitive behavior as reflected from the plateau-free galvanostatic charge–discharge profiles (Fig. 12e). This micro-supercapacitor exhibited a positive trend between its areal capacitance and the electropolymerization time, but the volumetric capacitance peaked after 15 min polymerization (Fig. 12f). The drop in the volumetric capacitance was attributed to the increased PEDOT thickness that impeded ion diffusion.

4.2.2 Nanowires and Nanorods

One-dimensional (1D) conducting polymers, such as polyaniline nanofibers [145–147] and polypyrrole nanorods

[148–150], are popular morphologies of pseudocapacitor electrodes. Their merits include the wide-open interfiber space that facilitates electrolyte infiltration and ion diffusion, as well as minimizes dead volumes (materials that are unusable for charge storage).

In the absence of any structure-directing agents, polyaniline preferentially forms randomly intertwined nanofibers [151]. Liu et al. electrodeposited polyaniline (PANI) nanowires on carbon cloth using cyclic voltammetry within a potential window between -0.2 and 0.8 V in aqueous electrolytes containing 0.1 M aniline and 1 M H_2SO_4 [25]. PANI nanowires were uniformly grown on carbon cloth fibers (Fig. 13a). To address the intrinsic cycling instability of PANI, the researchers conformally coated the deposited PANI nanowires with 5 -nm-thick carbonaceous shells by hydrothermally decomposing glucose. The coated PANI electrode exhibited a high theoretical areal capacitance of 787.4 mF cm^{-2} (estimated by the Trasatti method) and excellent cycling stability of $\sim 95\%$ after $10,000$ charge–discharge cycles. SEM revealed that the carbonaceous shell mitigated the volumetric deformation-induced structural pulverization of PANI.

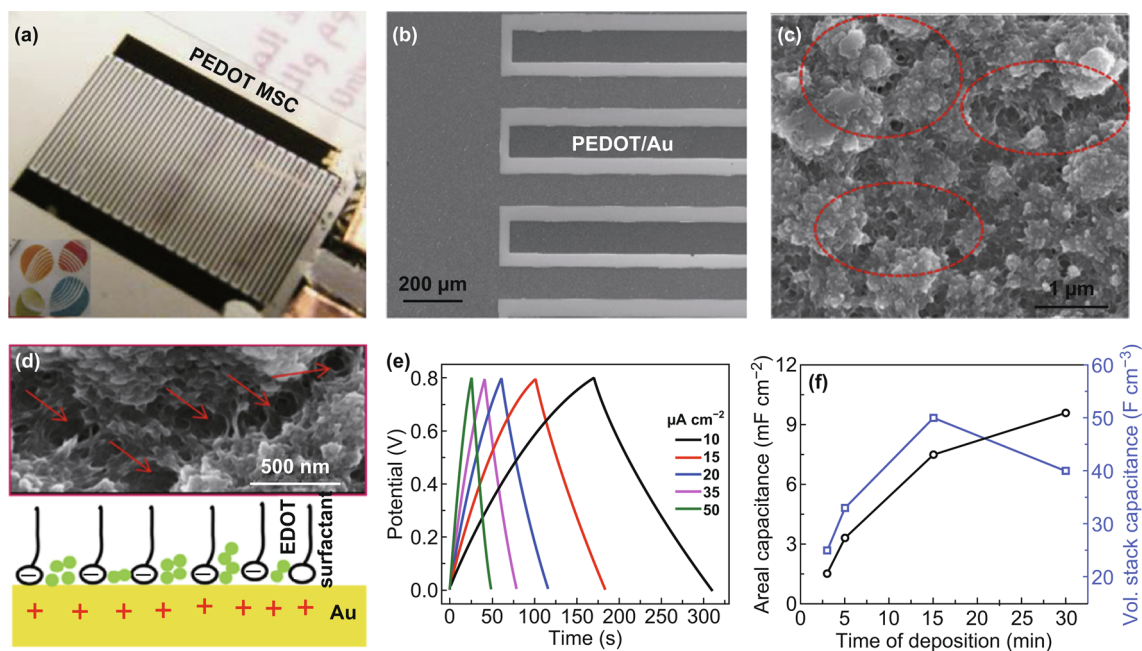


Fig. 12 **a** Photograph and **b** SEM image of PEDOT-coated interdigitated electrode. **c** Magnified view SEM image of the electrodeposited PEDOT film. The red circles highlight the cracks formed by soft templates. **d** Scheme illustrating the surfactant-induced crack formation. **e** Galvanostatic charge–discharge profiles of a symmetric micro-supercapacitor consisting of two PEDOT-coated interdigitated electrodes. Electrolyte: 1 M H_2SO_4 aqueous solutions. **f** Areal and volumetric capacitances of the symmetric micro-supercapacitor as a function of polymer deposition time. Adapted from Ref. [144] with permission

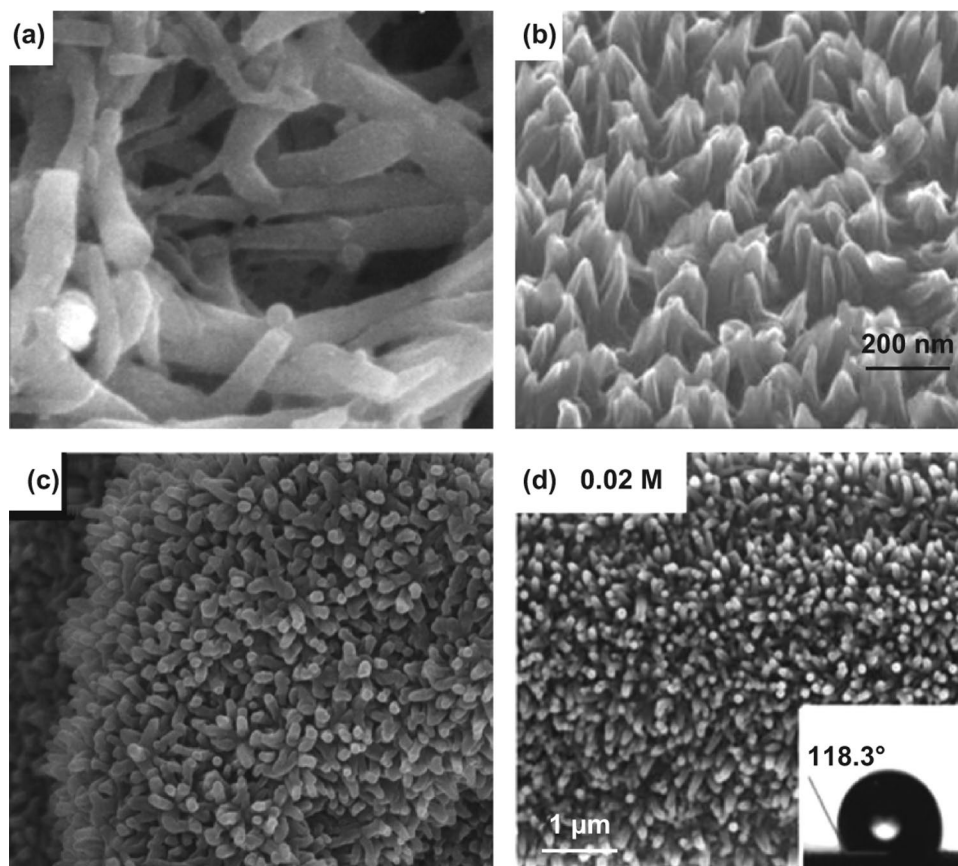


Fig. 13 Electrochemically deposited 1D polymer structures. **a** PANI nanofibers on carbon cloth; **b** PANI nanorod arrays on Au plates; **c** PANI nanorod arrays on carbon nanotube paper; **d** PPy nanorod arrays on carbon cloth. Adapted from **a** Ref. [25], **b** Ref. [153], **c** Ref. [145], **d** Ref. [149] with permission

Confining the growth of conducting polymers from current collector surfaces is a prerequisite to obtaining binder-free supercapacitor electrodes. To suppress electropolymerization of monomers in bulk electrolytes, small current, low potential, and dilute monomer solutions are preferred. Once polymer nucleates on substrate surfaces, they minimize the energy barrier for the subsequent growth of conducting polymer nanostructures [152, 153]. For example, PANI nanorod arrays were grown on a gold plate using a galvanostatic method with a small current density of 0.01 mA cm^{-2} (Fig. 13b) [153]. The formation mechanism followed the nucleation-initiated growth process. The electrodeposited PANI nanorod array electrode exhibited a high specific capacitance of 950 F g^{-1} at 1 A g^{-1} . Following the same protocol, PANI nanorod arrays were grown on other conductive substrates, such as carbon nanotubes (Fig. 13c) [145], exfoliated graphene sheets [154], as well as graphene papers [155, 156]. The generality of substrates indicated that

the nucleation growth process is independent of substrate properties.

In addition to PANI, electrochemical technology also produces polypyrrole (PPy) nanorod arrays on conductive substrates. Huang et al. fabricated PPy nanorod arrays via a one-step galvanostatic deposition at 1 mA cm^{-2} with *p*-toluenesulfonate acid (TsOH) as a soft template (Fig. 13d) [149]. The TsOH anions prevented the as-formed PPy oligomers from growing in random directions, promoting the growth of PPy nanorods on carbon cloth. Significantly, the PPy nanorods exhibited capacitance of 699 F g^{-1} at 1 A g^{-1} . When the current density increased from 1 to 20 A g^{-1} , 81.5% capacitance retained, indicating its excellent rate capability.

The use of hard templates enables the growth of sophisticated 1D nanostructures, such as nanotubes. Using nickel nanotube array (NiNTA) hard templates, Chen et al. made perchlorate-doped PPy nanotubes (Fig. 14) [157]. First, Ni

nanoparticles were dispersed on ZnO nanorod arrays to form ZnO@NiNRAs, followed by dissolving the ZnO templates to produce NiNTAs. Second, the electropolymerization of PPy on NiNTAs generated NiNTAs@PPy (Fig. 14a, b). High-resolution TEM showed abundant mesopores throughout

the PPy layer (Fig. 14c, d). Possibly, the mesopores formed during the polymerization process when the anions were inserted into PPy, and the cations were extracted. The highly porous hollow nanotube arrays in NiNTAs@PPy acted as ion reservoirs that shortened ion diffusion distance.

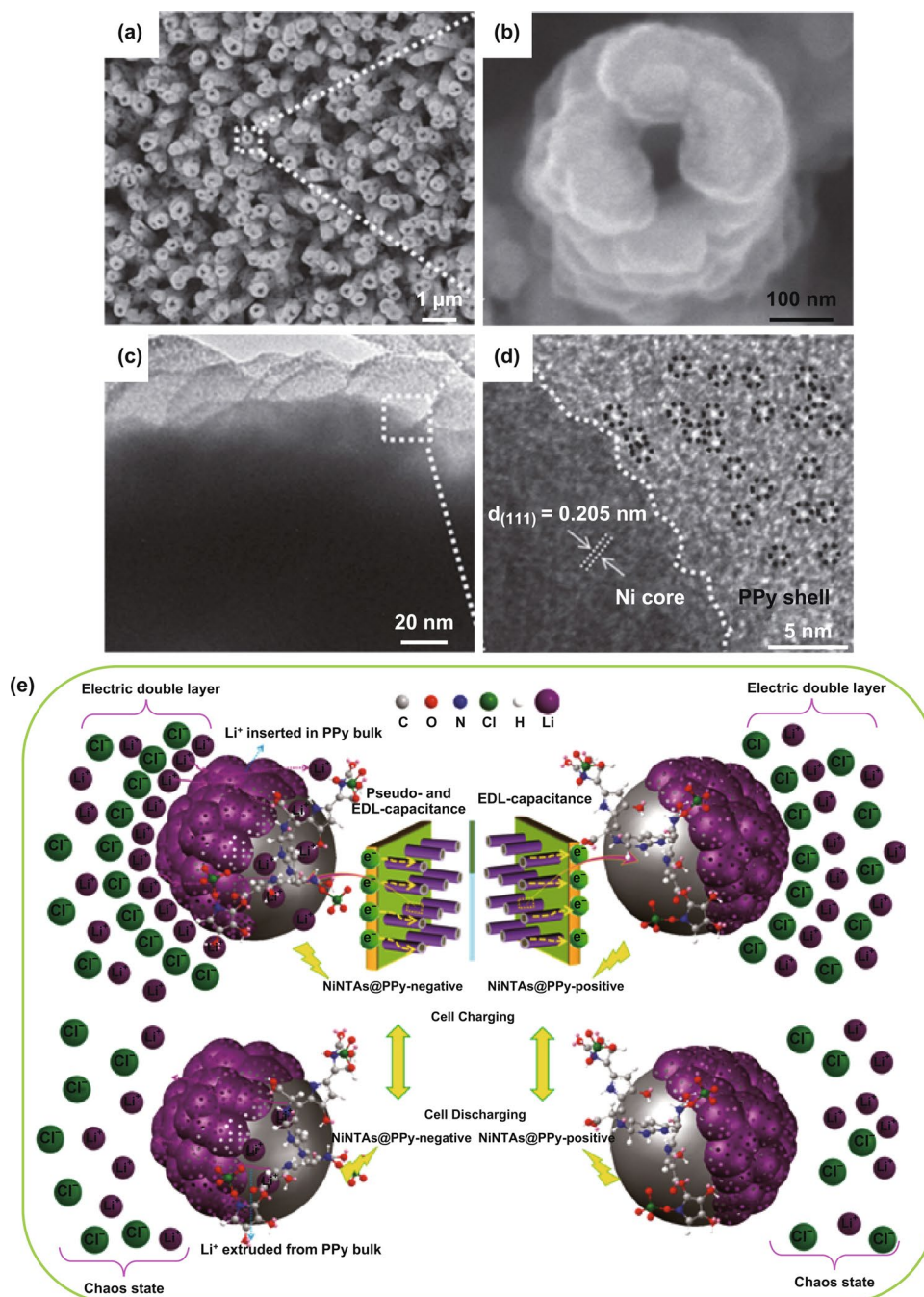


Fig. 14 a, b SEM and c, d TEM images of NiNTAs@PPy. The black dotted circles in d highlight micropores in PPy. e Schemes showing the charge storage mechanism of NiNTAs@PPy in supercapacitors during (top) charging and (bottom) discharging. Adapted from Ref. [157] with permission

Therefore, NiNTAs@PPy electrode displayed a high specific capacitance of 474.4 F g^{-1} at 5 mV s^{-1} . The PPy nanotubes also had excellent electrochemical stability with 75.3% capacitance retention after 10,000 charge–discharge cycles. The nanotube morphology and many pores and voids in PPy buffered the volumetric change of PPy and facilitated ion diffusion (Fig. 14e), which ensured excellent cycling stability.

4.2.3 Nanoplates

Electrochemically synthesized two-dimensional (2D) conducting polymers are rare because conducting polymers intrinsically prefer to grow into fibers or films. One typical example of 2D conducting polymer made by electropolymerization is pyrene nanosheets (Fig. 15a). They were grown in a mixed electrolyte containing boron trifluoride diethyl etherate (BFEE), trifluoroacetic acid (TFA), and

polyethylene glycol (PEG), using a potentiostatic technique (1.2 V vs. SCE) [158]. Spectroscopy revealed that the formation of nanosheets was due to oligomer growth via α – α coupling of pyrene rings. Besides pyrene, PPy nanosheets (Fig. 15b) were synthesized using cyclic voltammetry at a high scan rate of 200 mV s^{-1} in an aqueous electrolyte containing 0.05 M pyrrole and 0.1 M KNO_3 [159]. These PPy nanosheets interconnected with each other and assembled into a macroporous structure. It had a specific surface area of $37.1 \text{ m}^2 \text{ g}^{-1}$ and a specific capacitance of 584 F g^{-1} at 5 mA cm^{-2} .

Hard template methods can also synthesize 2D polymer materials (Fig. 15c, d). These 2D templates (e.g., graphene sheets [160] and layered double hydroxides [161]) are structural scaffolds to direct the growth of conducting polymers in 2D fashion, endowing fast ion diffusion pathways in the electrode materials that results in excellent rate capability.

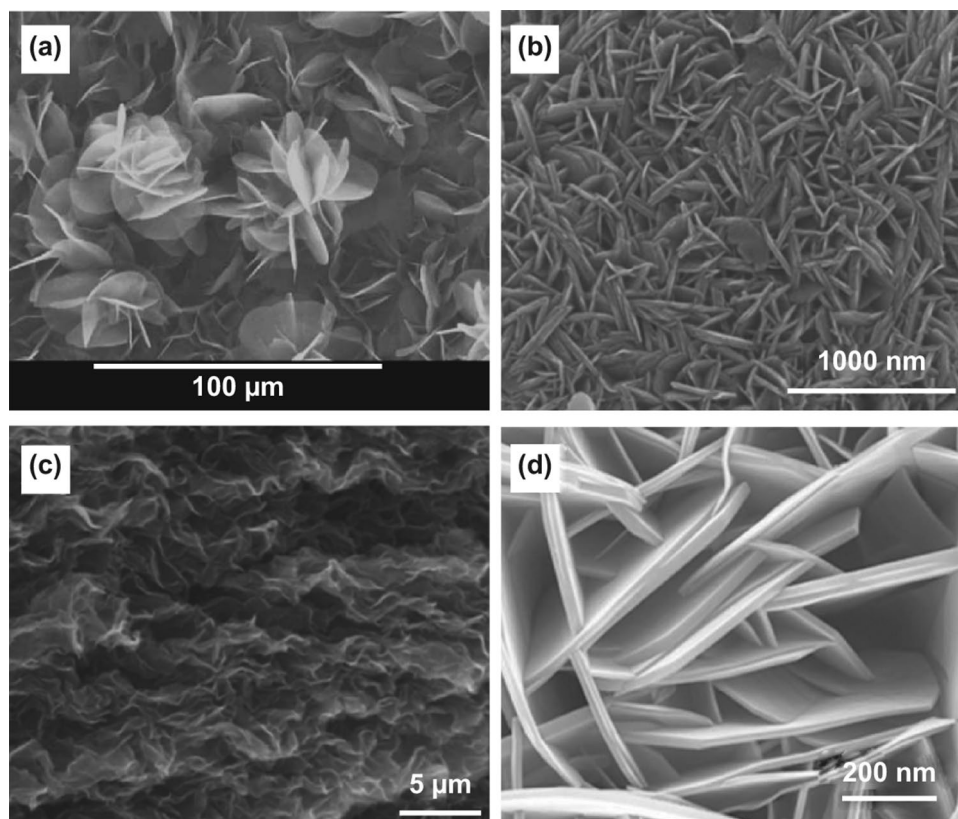


Fig. 15 Electrodeposited two-dimensional conducting polymers. **a** Oligopyrene nanosheets; **b** PPy nanosheets; **c** PANI nanosheets on graphene sheets; **d** PEDOT thin films on CoAl layered double hydroxide nanoplates. Adapted from **a** Ref. [162], **b** Ref. [159], **c** Ref. [160], **d** Ref. [161] with permission

4.2.4 3D Networks

Three-dimensional (3D) conductive structures provide large ion-accessible surface areas and abundant pores compared to 2D architectures and, thus, are increasingly popular morphologies of electrochemically deposited conducting polymers. High surface area can effectively reduce the local current density and polarization in bulk electrodes and thus improve the electrodes' charge storage kinetics. Unfortunately, ideal 3D structures composed merely of conducting polymers are challenging to acquire, due to their preferably random growth into films or fibers during electropolymerizations.

To circumvent this challenge, researchers adopt templates to construct 3D conducting polymers. Demonstrated templates, including carbon nanotube foam [163] (Fig. 16a, b), graphene foam [164] (Fig. 18c), partial exfoliated graphite [26] (Fig. 16d), as well as Ni foam [165] (Fig. 16e–g), have been used to construct 3D polymer-based electrodes. For example, Park et al. deposited a PPy film on graphene foam (Fig. 16c) [164]. The high surface area of graphene foam and the pseudocapacitance of PPy synergistically improved the performance of the electrode. Wang et al. reported a PPy

foam using a sacrificial Ni foam template (Fig. 16e) [165]. PPy was first electrodeposited on a Ni foam (Fig. 16f), and subsequently, the Ni foam was etched away, leaving a free-standing 3D PPy foam (Fig. 16g). This as-prepared 3D PPy foam was mechanically strong and highly flexible, making it a multifunctional 3D material in sensors, supercapacitors, and supports for graphene. Moreover, the freestanding 3D PPy exhibited a capacitance of 316.2 F g^{-1} at 2 mV s^{-1} , and the graphene-coated 3D PPy achieved a higher capacitance of 702.9 F g^{-1} at the same scan rate. The incorporation of graphene created highly conductive surface coatings as well as increasing specific surface area from 72 to $113.4 \text{ m}^2 \text{ g}^{-1}$.

5 Metal Oxides and Hydroxides

5.1 Manganese Oxides

Manganese oxides, particularly manganese dioxide (MnO_2), have attracted immense interest as one of the most commercially promising pseudocapacitive materials, due to its high theoretical capacitance ($\sim 1000 \text{ F g}^{-1}$), cost efficiency, source abundance, and environmental friendliness [166, 167]. A variety of chemical and electrochemical techniques

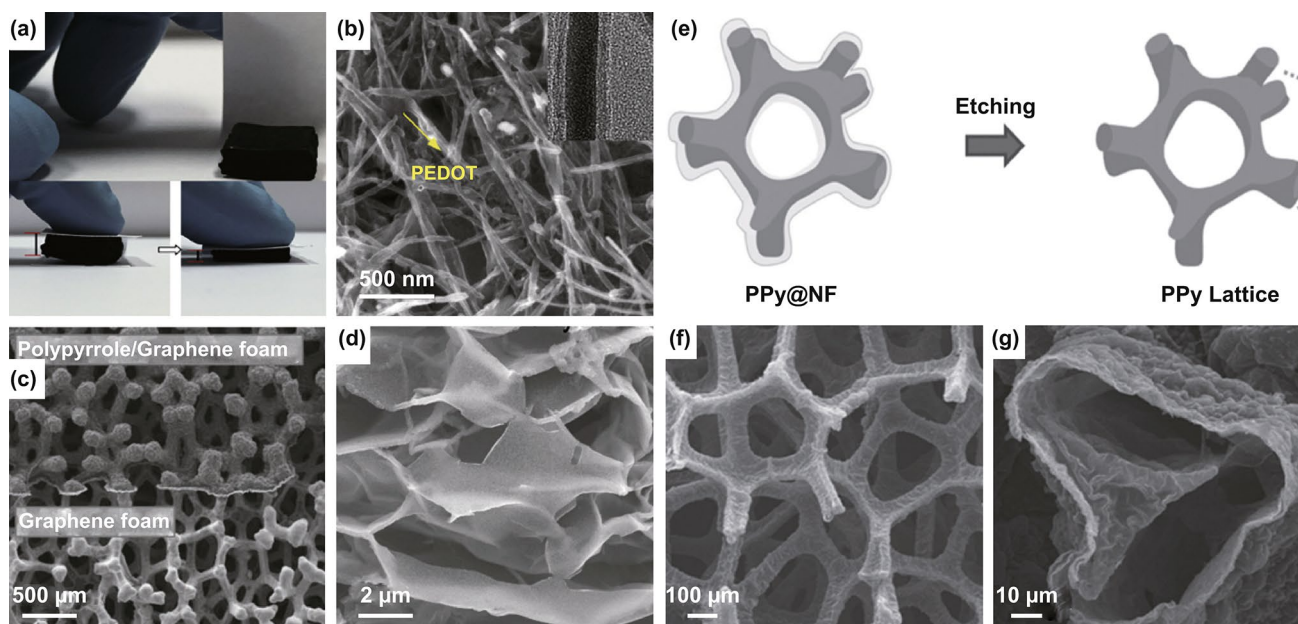
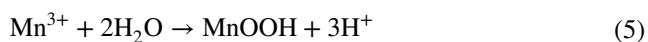


Fig. 16 **a** Photographs and **b** SEM and TEM (inset) images of a compressible, PEDOT-coated carbon nanotube sponge. **c** SEM image of PPy-coated graphene (top) and bare graphene (bottom) foams. **d** PPy film deposited on electrochemically exfoliated graphite foil. **e** Scheme of the fabrication process of 3D PPy foam. **f**, **g** SEM images of 3D PPy foam at different magnifications. Adapted from **a**, **b** Ref. [163], **c** Ref. [164], **d** Ref. [26], **e–g** Ref. [165] with permission

have synthesized manganese oxides. Among them, anodic electrodeposition is the most time-efficient. This technique deposited MnO_x by consecutive oxidation of Mn^{2+} , as illustrated in the following equations [168, 169]:



The nanostructures of electrodeposited MnO_x are tunable by varying the electrolyte composition, temperature, potential, and current density. For example, Feng et al. demonstrated that complexing agents such as CH_3COO^- and NH_4^+ significantly reduced the charge transfer resistance of the electrooxidation of Mn^{2+} [166], changing the morphology of MnO_x from 2D nanosheets to 1D nanoneedles. These observations indicate that diminishing charge transfer resistance of MnO_x electrodeposition impedes its lateral growth.

Wei et al. proposed a theory of the supersaturation ratio of Mn^{2+} to rationalize the diverse morphologies of anodically electrodeposited MnO_x (Fig. 17a) [170]. Supersaturation ratio is defined as the ratio of the actual concentrations (or more vigorously speaking, activities) of all the ions associated with electrodeposition to the equilibrium concentrations of the same set of ions. The authors observed that high concentrations of $\text{Mn}(\text{NO}_3)_2$ and large current densities induced high supersaturation ratios that led to uniform coatings. In contrast, low concentrations of $\text{Mn}(\text{NO}_3)_2$ and small current densities favored epitaxial growth into interconnected nanosheets (Fig. 17b–f). These different morphologies were associated with the number of nucleates formed at the beginning of electrodeposition. High supersaturation ratios yielded abundant nucleation sites that suppressed epitaxial growth. Parameters that lowered the supersaturation ratio decreased the number of nucleation sites and favored the formation of nanostructures.

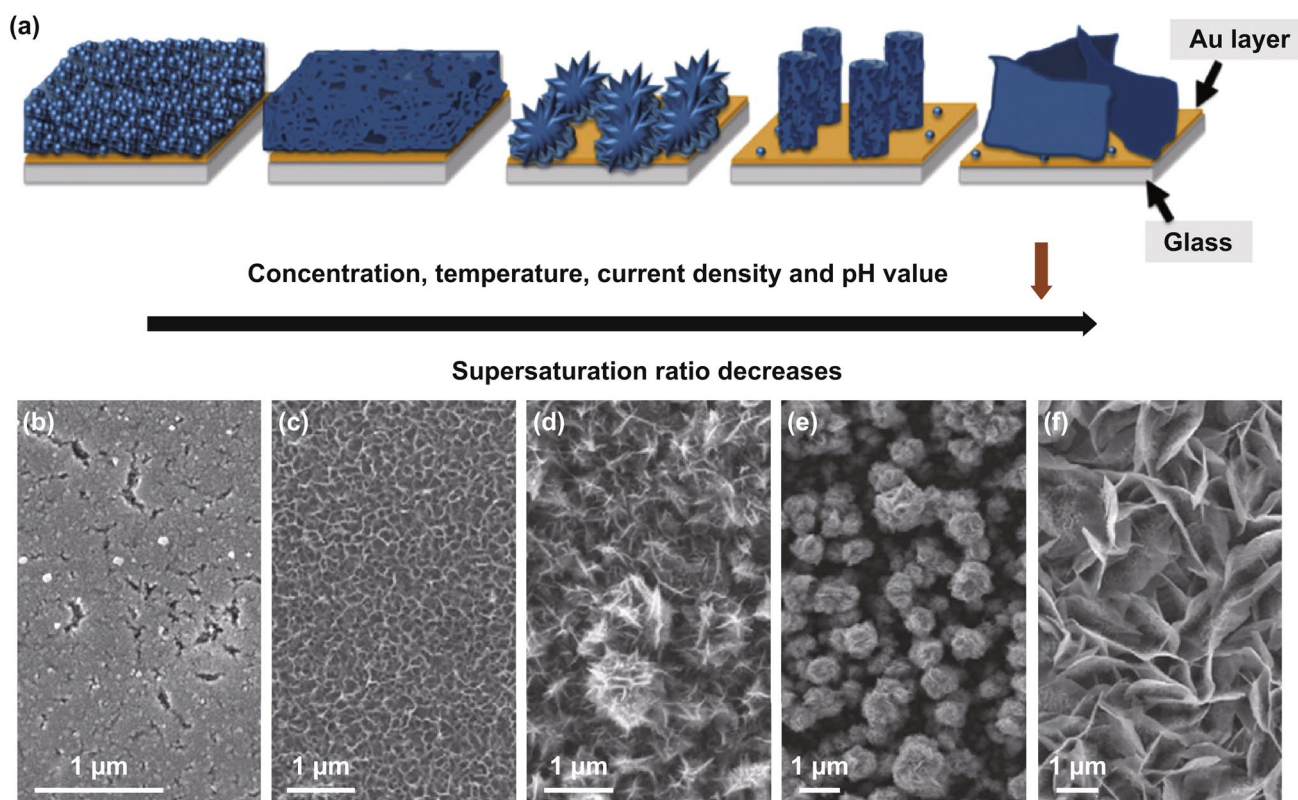


Fig. 17 a Schemes of the morphological evolution of MnO_x across different electrodeposition supersaturation ratios. b–d Top-view SEM images of MnO_x electrodeposited in 0.1 M $\text{Mn}(\text{NO}_3)_2$ aqueous solutions at various current densities: b 20 mA cm^{-2} , c 1 mA cm^{-2} , and d 0.1 mA cm^{-2} . e–f SEM images of MnO_x prepared in 0.0025 M $\text{Mn}(\text{NO}_3)_2$ at e 0.1 mA cm^{-2} and f 0.05 mA cm^{-2} . Adapted from Ref. [170] with permission

5.1.1 Nanorods and Nanotubes

Templating is a typical strategy to prepare 1D MnO_x nanostructures [171, 172]. ZnO nanorods [173], anodized alumina [174, 175], hydrogenated TiO_2 nanorods [176], and silicon square pillars [177] are reported templates for electrodepositing MnO_x nanorod or nanotube arrays. For example, Li and coworkers synthesized double-walled carbon/ MnO_2 nanotube arrays using ZnO nanorods as sacrificial templates [173] (Fig. 18a). First, ZnO nanorod arrays were grown on Ti plates via electrodeposition, and thin layers of carbon were coated on the nanorods to render the ZnO nanorods electrically conductive. Afterward, a uniform MnO_2 film was electrodeposited on the carbon-coated ZnO nanorod arrays (Fig. 18b). Finally, dissolving the ZnO nanorod arrays using 0.5 M NaOH solution generated the double-walled carbon/ MnO_2 nanotube arrays (Fig. 18c). These double-walled nanotubes displayed a high specific capacitance of 793 F g^{-1} at 1.5 A g^{-1} , and a rate capability of 83% when the scan rate increased from 5 to 50 mV s^{-1} . The excellent electrochemical performances were ascribed to factors including: (1) the hollow structure of the nanotube arrays exposed plentiful active sites of MnO_2 and provided

ions with fast diffusion pathways; (2) the conformal carbon coating served as electron transport expressways, minimizing capacitance loss at elevated scan rates; and (3) the high weight fraction of MnO_2 (~98.94 wt%) in the electrodes was beneficial to achieve high specific capacitance and energy density.

Besides templating, template-free methods could also synthesize 1D nanostructured MnO_x . These methods are time-efficient and can synthesize products of high purity because they lift the needs for template incorporation and removal [178, 179]. For example, Lu and coworkers demonstrated that adding dimethyl sulfoxide (DMSO) in the deposition solution of MnO_2 led to MnO_2 nanorod arrays without any templates [180]. They applied a constant anodic current of 0.2 mA cm^{-2} at $70 \text{ }^\circ\text{C}$ and used aqueous electrolytes containing 0.01 M manganese(II) acetate, 0.02 M ammonium acetate, and 10 wt% DMSO. The resultant MnO_2 nanorods had diameters between 70 and 100 nm, and lengths up to $\sim 1.5 \mu\text{m}$ (Fig. 18d). Electrodeposition without DMSO only yielded MnO_2 herringbones (Fig. 18e). Though the authors did not justify how DMSO changed the deposit morphology, we hypothesized that the addition of DMSO reduced the supersaturation ratio of Mn^{2+} , and thus promoted epitaxial

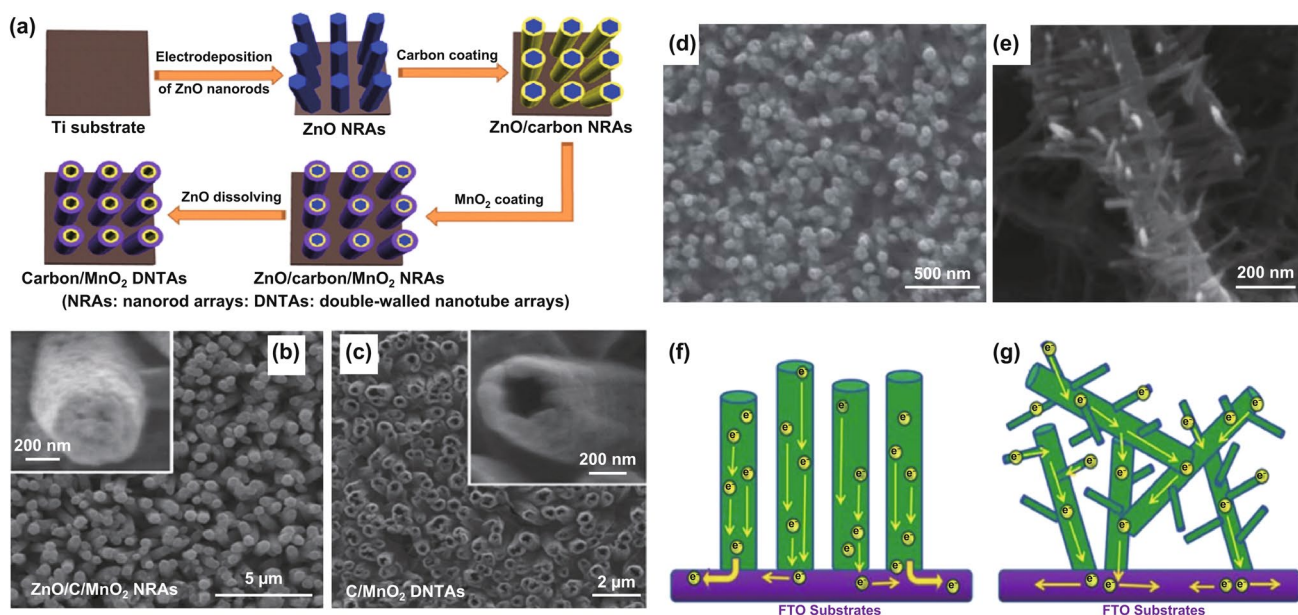


Fig. 18 **a** Schemes of the synthesis procedures of double-walled MnO_2 nanotube arrays on carbon cloth. **b** SEM image of ZnO/C/ MnO_2 nanorod arrays. Inset: Magnified view of a single nanorod. **c** SEM image of C-coated MnO_2 double-walled nanotubes. Inset: Magnified view showing a C-coated MnO_2 nanotube. **d**, **e** SEM images of MnO_x **d** nanorods and **e** herringbones. **f**, **g** Schemes of the charge transfer pathways in **f** MnO_x nanorod arrays and **g** MnO_x herringbones. Adapted from **a–c** Ref. [173] and **d–g** Ref. [180] with permission

growth of MnO_2 into nanorods. The specific capacitance of the MnO_2 nanorod array was 660.7 F g^{-1} at 10 mV s^{-1} , which was $\sim 100 \text{ F g}^{-1}$ higher than that of the herringbone structured MnO_2 (564.3 F g^{-1}). This capacitance discrepancy was associated with the morphology: The ordered vertically aligned nanorods, compared with the herringbones, reduced the tortuosity and distances for electron transport, which boosted capacitance (Fig. 18f, g).

5.1.2 Nanosheets and Nanoplates

Ultrathin 2D MnO_x nanosheets were other common morphologies of electrodeposited MnO_x [181–185]. Anodic deposition is widely demonstrated to prepare MnO_x nanosheets [186–195]. For example, Yao et al. deposited

MnO_2 nanosheets onto 3D printed graphene aerogel lattices through an anodic galvanostatic deposition at 10 mA cm^{-2} (Fig. 19a) [196]. The outstanding property of these 3D printed MnO_2 /graphene composite electrodes was their uncompromised electrochemical performance at MnO_2 mass loadings as high as 182.2 mg cm^{-2} . The areal capacitance scaled linearly with the thickness of the electrode, reaching 44.13 F cm^{-2} at 0.5 mA cm^{-2} in 3 M LiCl aqueous electrolytes at a thickness of 4.0 mm (MnO_2 mass loading 182.2 mg cm^{-2}). This linear relationship indicated that the charge storage process of the electrode was not under diffusion control or limited by ion percolation even at ultrahigh mass loadings and thicknesses. This merit was attributed to the 3D-printed graphene lattices with macropores of 5–50 μm pores (Fig. 19b, c), which promoted the uniform

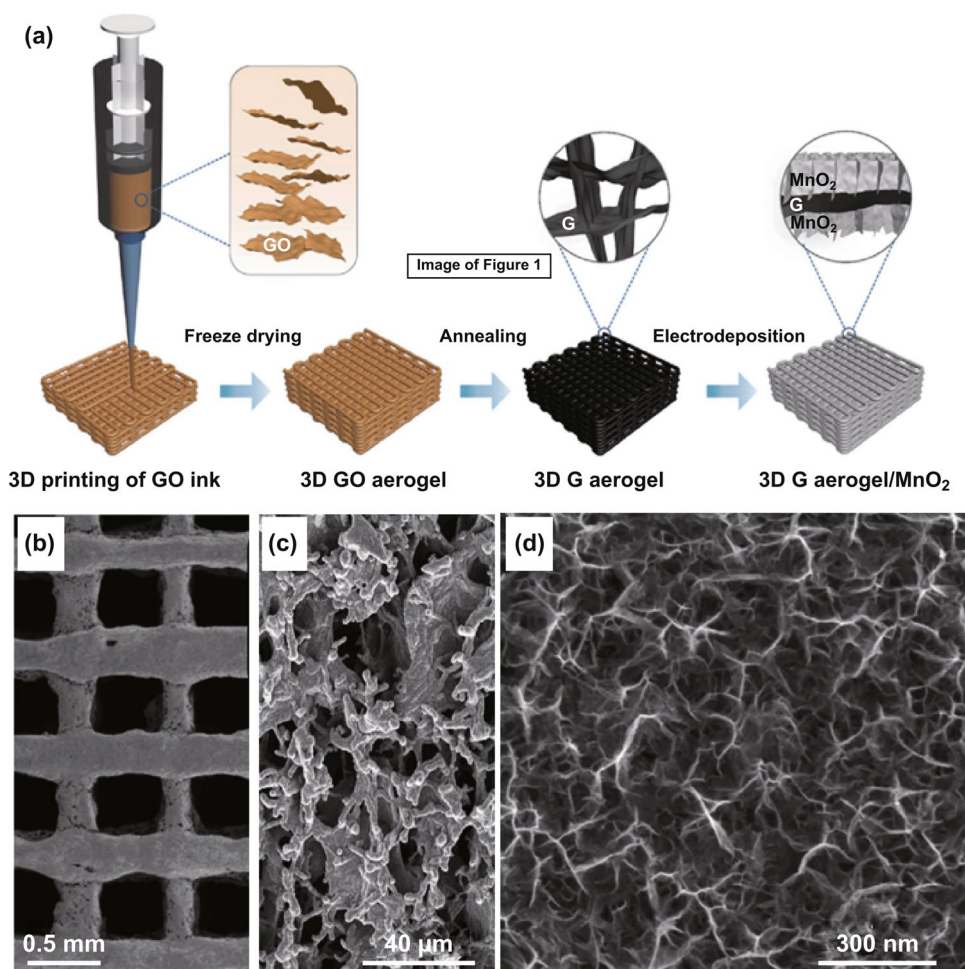


Fig. 19 a Schemes of the synthesis procedures of MnO_2 nanosheets deposited on 3D printed graphene aerogel lattices. b A top-view SEM image of MnO_2 -coated 3D printed graphene aerogel. c, d SEM images of the deposited MnO_2 nanosheets at two magnifications. Adapted from Ref. [196] with permission

deposition of MnO_2 and opened up wide ion diffusion pathways throughout the entire electrodes.

In addition to anodic electrodeposition, cathodic electrodeposition also synthesizes 2D MnO_x nanosheets. For example, Beyazay et al. used a chronoamperometry technique to deposit Mn_3O_4 hexagonal nanosheets on graphene paper. This electrode delivered a maximal specific capacitance of 546 F g^{-1} at 0.5 A g^{-1} . Interestingly, the capacitance increased about 1.5 times after being charged and discharged for 10,000 times. XPS analysis after the stability test found that the average valence of Mn raised from 2.7 to 3.2, indicating that part of Mn_3O_4 was oxidized to MnO_2 . Besides the valence change, some hexagonal nanosheets transformed into particles and needles. These results suggested that the hexagonal Mn_3O_4 nanosheets were both chemically and structurally unstable during long-term cycling tests.

5.1.3 Hierarchical Structures

Hierarchical MnO_x integrates nanostructures of different dimensions, e.g., 1D nanorod, 2D nanosheet, and 2D nanoplate. Electrodepositing hierarchical structures often begins with one specific structure. For example, Jabeen et al. synthesized Mn_3O_4 nanosheet-on-nanowall arrays via a cathodic potentiostatic method ($-1.8 \text{ V vs. Ag/AgCl}$) in an aqueous solution containing 0.1 M manganese acetate and 0.1 M sodium sulfate. High-resolution scanning electron microscopy revealed that these nanowalls were composed of interconnected nanoparticles (Fig. 20a) [14]. After 500 cycles of electrochemical oxidation in 10 M sodium sulfate aqueous solutions, the nanoparticles disappeared, and nanosheets appeared on the surface of the nanowalls, assembling the nanosheet-on-nanowall hierarchical structure (Fig. 20b, c). Meanwhile, the composition of the electrode changed from Mn_3O_4 to $\text{Na}_{0.5}\text{MnO}_2$. The hierarchically structured $\text{Na}_{0.5}\text{MnO}_2$ exhibited a specific capacitance of 366 F g^{-1} at 1 A g^{-1} . Besides, the redox peak of $\text{Na}_{0.5}\text{MnO}_2$ at $\sim 0.96 \text{ V vs. Ag/AgCl}$ extended the upper limit potential to approximately $1.3 \text{ V vs. Ag/AgCl}$, enabling the development of aqueous-based supercapacitors with high voltages and energy densities.

The most significant characteristic of hierarchical structures is their capability to maintain excellent electrochemical performance at MnO_x mass loadings exceeding 10 mg cm^{-2} . Increasing the mass loadings of MnO_x (and other

pseudocapacitive materials) has become a trend in recent years, due to the consideration of practicality. Unfortunately, the capacitances of poorly conductive pseudocapacitive materials, including MnO_x , are greatly compromised when enhancing their mass loadings, particularly under fast charge and discharge rates. Hierarchical structures could resolve this challenge. For example, Song et al. developed an Ostwald ripening strategy that improved the rate capability of electrodeposited MnO_x thick films with a high mass loading of $\sim 10 \text{ mg cm}^{-2}$ (Fig. 20d–f) [197]. The authors first coated carbon fibers with MnO_x films of $\sim 4.5 \mu\text{m}$ thick using a constant current of 10 mA cm^{-2} in 0.1 M manganese acetate aqueous solutions (Fig. 20d). They then hydrothermally treated the electrodeposited MnO_x at $90 \text{ }^\circ\text{C}$, which appreciably altered the morphology of the MnO_x films. First, many crystalline MnO_x nanosheets formed on the surface. Second, the porosity of the MnO_x core increased (Fig. 20e, f). The porous MnO_x core and oxide shell together constituted a core-shell hierarchical structure. The crystalline surface ensured good electrical conductivity, and the porous MnO_x core sped up ion diffusion. Therefore, the electrode exhibited improved rate performance even at a high mass loading of 10 mg cm^{-2} . Recently, Huang et al. have demonstrated a facile electrochemical technology that synthesized a nanorod-on-nanosheet hierarchical structure. The structure consisted of primary two-dimensional $\epsilon\text{-MnO}_2$ nanosheets and secondary one-dimensional $\alpha\text{-MnO}_2$ nanorod arrays (Fig. 20g–i) [50]. Morphology studies indicated that elevating the deposition temperature to $60 \text{ }^\circ\text{C}$ and $80 \text{ }^\circ\text{C}$ added nucleation sites on the as-formed nanorods, which favored the secondary growth of nanorods. This hierarchical electrode had a high MnO_2 mass loading of 10 mg cm^{-2} and delivered a high areal capacitance of 3.04 F cm^{-2} at 3 mA cm^{-2} . Significantly, the areal capacitance maintained at 1.9 F cm^{-2} at 30 mA cm^{-2} . The authors ascribed this excellent rate capability performance to two factors: First, the multiple connections between the nanorods and nanosheets created fast avenues for electron transport. Second, the voids among the nanorods and nanosheets throughout the hierarchical structure facilitated electrolyte ion percolation and ion diffusion.

5.2 Vanadium Oxides

Vanadium oxides (VO_x), mainly vanadium pentoxide (V_2O_5), have the advantages of high specific capacitance

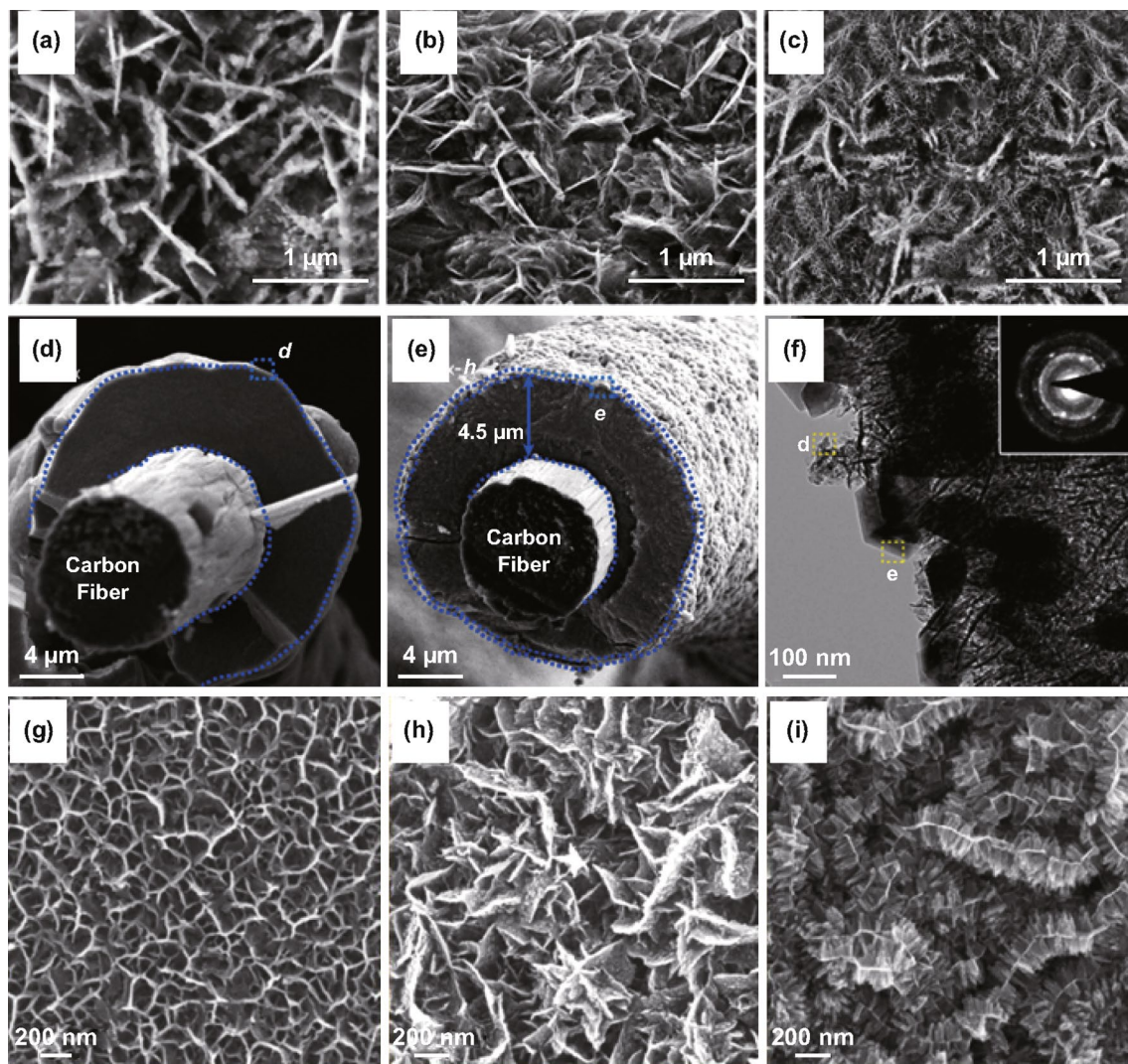
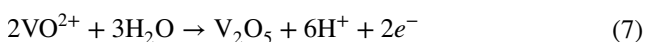


Fig. 20 a–c SEM image of a Mn_3O_4 nanowall arrays, b intermediates during electrochemical oxidation, and c hierarchical $\text{Na}_{0.5}\text{MnO}_2$ nanowall arrays. d, e SEM images of d as-deposited and e hydrothermally treated MnO_x thick layer on carbon fiber. f TEM image of hydrothermally treated MnO_x . g–i SEM images of MnO_2 deposited at g 25 °C, h 40 °C, and i 60 °C. Adapted from a–c Ref. [14]; d–f Ref. [197]; g–i Ref. [50] with permission

(multiple electron reaction, e.g., from +3 to +5), low cost, ease of fabrication, as well as wide potential windows [37, 198–202]. Electrochemical technologies are particularly suitable for synthesizing VO_x of diverse morphologies, crystal structures, and valence states [203–209]. In aqueous electrolytes, vanadium oxide is typically synthesized from the oxidation of vanadium-containing ions with the aid of water molecules. For example, oxovanadium(IV) cations, VO^{2+} , are electrooxidized to high-valence vanadium oxides (e.g., V_2O_5) through the following equation [208]:



For example, Xie et al. demonstrated that the pH value and composition of acetate salts (CH_3COONa , CH_3COOLi , CH_3COOK) were critical in tuning the deposition rate, crystal structure, and morphology of VO_x [209]. Drosos et al. studied the effects of the deposition current density on the morphology and electrochemical performance of V_2O_5 coatings on indium-doped tin oxide glass substrates in 1 M LiClO_4 polypropylene carbonate electrolytes. The V_2O_5 film deposited at 1 mA cm^{-2} exhibited the highest capacitance owing to its roughest surface [210].

Electrodeposited VO_x with mixed V valences are platforms for studying the interplays between V valence and cycling stability. Recent studies indicated that the

performance degradation was linked to dissolution, structural pulverization, and irreversible phase transition of VO_x [34, 37, 199]. Investigating the cycling behavior of electrodeposited VO_x electrodes in various aqueous environments, Engstrom and Doyle concluded that the formation of water-soluble V-containing species, including H_2VO_4^- , HVO_4^{2-} , HV_2O_5^- , VO^{2+} , HVO^{2+} , and VO^+ (Fig. 21a), was the primary cause of capacitive decay of VO_x during extensive cycling tests [199]. Though chemical strategies such as surface coating [211, 212] and electrolyte pH value tuning [199] minimized dissolution of VO_x , the altered electrode kinetics usually compromised capacitance. To circumvent these limitations, Song et al. utilized a potentiostatic electrochemical method to tune the V valence in VO_x and achieved record-high cycling stability without capacitive decay over 100,000 cycles (Fig. 21b–d) [37]. VO_x nanorods were first electrodeposited on electrochemically exfoliated carbon cloth fibers using cyclic voltammetry between -1.5 and 1.4 V vs. SCE (Fig. 21c). The authors then reduced the as-deposited VO_x at a constant potential of -1.5 V vs. SCE for 1 min. This reduction raised the $\text{V}^{4+}/\text{V}^{5+}$ ratio from 0.4 to an optimal value of around 0.5. The optimized $\text{V}^{4+}/\text{V}^{5+}$

ratio in VO_x effectively suppressed the chemical dissolution of VO_x . Meanwhile, the firm anchoring of the reduced VO_x nanorods on oxygenated, exfoliated carbon cloth fibers via C–O–V bonds retained the structural integrity of VO_x . Both factors contributed to the excellent cycling stability (ECC/RVO_x in Fig. 21d).

The easy valence tuning of VO_x by electrochemical techniques allowed the synthesis of heterojunctions between VO_x of two valences. These configurations help facilitate electron transfer within VO_x electrodes having large thicknesses or high mass loadings [34]. For instance, Dong et al. performed a density functional theory (DFT) calculation and discovered that a built-in electric field formed at the $\text{V}_5\text{O}_{12}/\text{VO}_2$ heterojunction. The charge redistribution between the two oxides led to an electric field pointing from VO_2 to V_5O_{12} (Fig. 22a) [34]. This built-in electrical field facilitated electron transfer and modulated ion absorption during charge storage processes, which improved electrochemical performance. Inspired by this calculation result, the authors adopted cyclic voltammetry (-1.5 to 1.5 V vs. SCE) to electrodeposit $\text{V}_5\text{O}_{12}/\text{VO}_2$ nanorods on an exfoliated graphite substrate. V_5O_{12} first formed during the positive scan, and

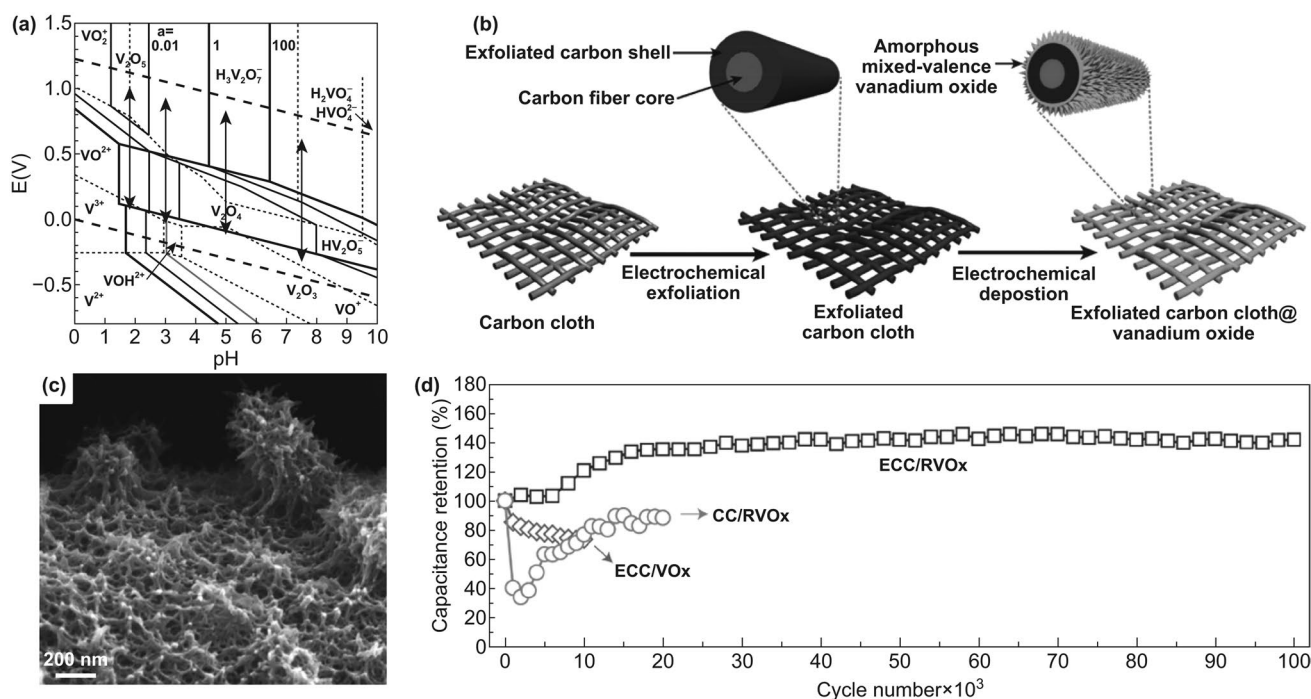


Fig. 21 **a** E -pH diagram of vanadium oxide–water system with various V-based species at activities (the letter “a” in the figure) of 0.01, 1 and 100. **b** Schemes of the synthesis steps, **c** SEM image, and **d** cycling stability of amorphous, mixed-valence vanadium oxide (RVO_x) deposited on exfoliated carbon cloth fibers. Adapted from **a** Ref. [199] and **b–d** Ref. [37] with permission

it was partially reduced to VO_2 in the subsequent negative scan (Fig. 22b). $\text{V}_5\text{O}_{12}/\text{VO}_2$ with a high mass loading of about 10.8 mg cm^{-2} delivered a high areal capacitance of 5.03 F cm^{-2} (465 F g^{-1}) at 1 mA cm^{-2} , outperforming pure V_5O_{12} and VO_2 (Fig. 22c). Significantly, $\text{V}_5\text{O}_{12}/\text{VO}_2$ also exhibited enhanced cycling stability compared to V_5O_{12} and VO_2 alone (Fig. 22d). Two reasons could account for this stability enhancement. First, EIS indicated that $\text{V}_5\text{O}_{12}/\text{VO}_2$ exhibited reduced charge transfer resistance due to the heterojunction (Fig. 22e). Second, ex situ XRD confirmed that $\text{V}_5\text{O}_{12}/\text{VO}_2$ underwent no phase transitions

after charging and discharging, while the phases of V_5O_{12} and VO_2 changed dramatically (Fig. 22f–h). The reduced resistance and suppressed phase change of $\text{V}_5\text{O}_{12}/\text{VO}_2$ both enhanced cycling stability.

5.3 Molybdenum Oxides

Molybdenum oxides (MoO_x) are another group of electrodeposited pseudocapacitive materials [213–215]. Unlike MnO_x discussed in the previous sections, MoO_x is acid-resistant and thus can work in acidic electrolytes [216].

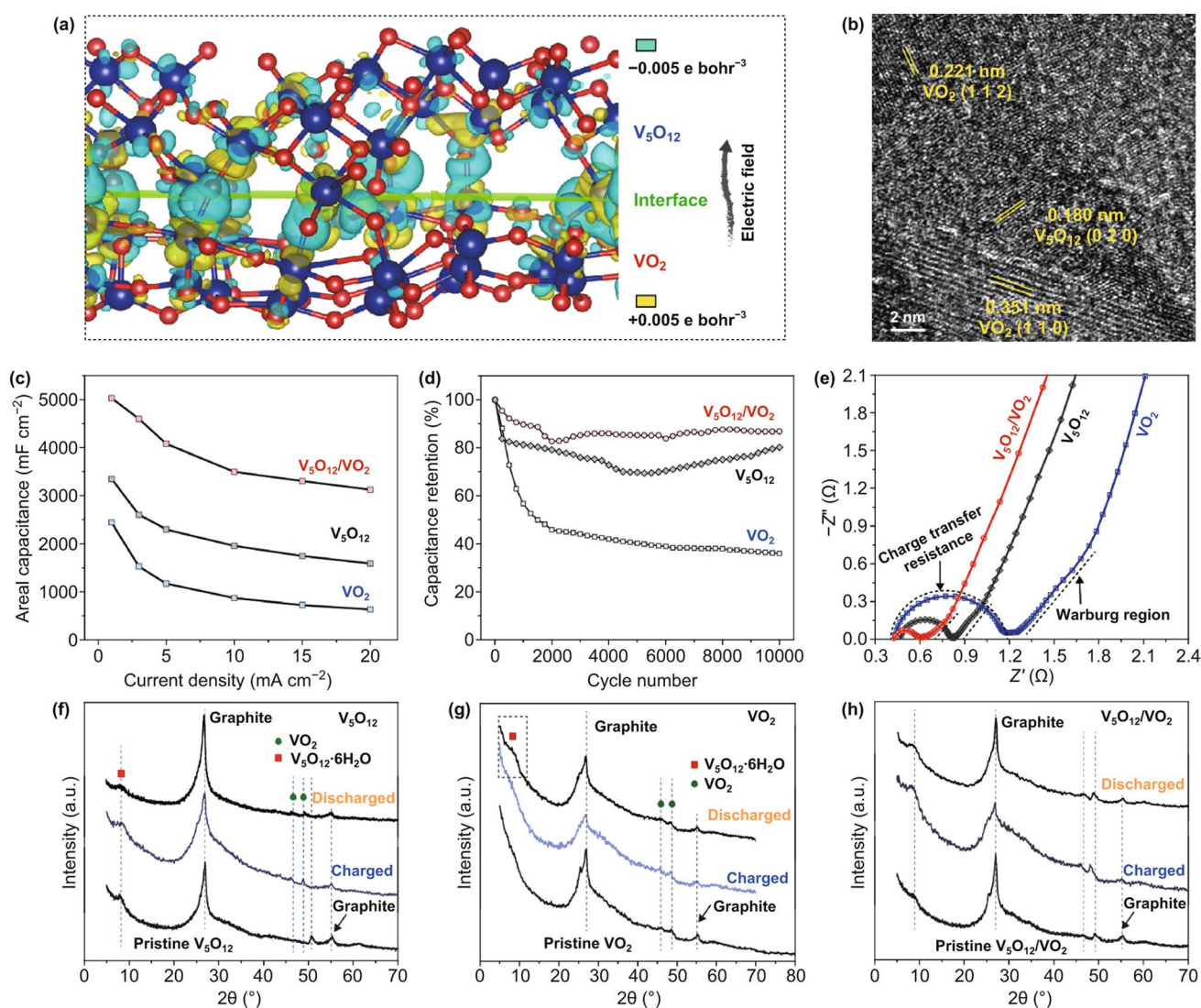


Fig. 22 **a** Charge density distribution along the interface of $\text{V}_5\text{O}_{12}/\text{VO}_2$. **b** TEM image of $\text{V}_5\text{O}_{12}/\text{VO}_2$ junction. **c** Areal capacitance of $\text{V}_5\text{O}_{12}/\text{VO}_2$, V_5O_{12} , and VO_2 as a function of current density. **d** Cycling stability of $\text{V}_5\text{O}_{12}/\text{VO}_2$, V_5O_{12} , and VO_2 electrodes in 3 M LiCl aqueous electrolyte. **e** Nyquist plots of $\text{V}_5\text{O}_{12}/\text{VO}_2$, V_5O_{12} , and VO_2 . **f–h** Ex situ XRD patterns of **f** V_5O_{12} , **e** VO_2 and **h** $\text{V}_5\text{O}_{12}/\text{VO}_2$ without charging (pristine), charged (-1 V), and discharged (0 V). Reproduced from Ref. [34] with permission

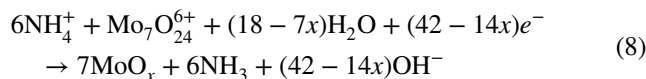
Besides surface redox reactions, some MoO_x , e.g., $\alpha\text{-MoO}_3$, possess layered structures that allow ion insertion and deinsertion that contribute intercalative pseudocapacitance [217]. Specifically, $\alpha\text{-MoO}_3$ can accommodate up to 1.5 Li^+ per Mo, having a high theoretical capacity of 1117 mAh g^{-1} [218].

MoO_x is usually deposited by cathodic electrodeposition in aqueous electrolytes containing molybdates (e.g., sodium molybdate and ammonium molybdate) [38], iso-/peroxo-polymolybdates [213], and ammonium paramolybdates [219]. Electrodeposited MoO_x are typically quasi-amorphous, non-stoichiometric oxide films [38, 220–222]. Its composition, structure, and electrochemical performance of the deposited MoO_x materials highly depend on electrolyte composition, pH value, and magnitudes of the applied current density and voltage [223–225].

Nanostructured substrates with large ion-accessible surface areas are preferred electrodeposition scaffolds for MoO_x . For example, a $\sim 18\text{-nm}$ -thick layer of MoO_x (3 mg cm^{-2}) was deposited on tungsten oxide nanowires, forming a $\text{WO}_{3-x}/\text{MoO}_{3-x}$ core/shell structure (Fig. 23a–d) [226]. This core/shell electrode delivered an areal capacitance of 500 mF cm^{-2} . Li et al. electrodeposited a 40-nm -thick MoO_3 layer (2.43 mg cm^{-2}) on ZnO nanorod arrays (Fig. 23e, f). The ZnO-supported MoO_3 displayed a specific capacitance of 241 F g^{-1} at 5 mV s^{-1} and 198 F g^{-1} at 100 mV s^{-1} [227]. Liu et al. demonstrated that functionalized, partially exfoliated graphite foil substrates could support MoO_x films with high mass loadings (18.4 mg cm^{-2}) (Fig. 23g) [228]. The exfoliated graphene sheets and the laminar structure of the graphite base addressed the negative impact of the poor electrical conductivity of the atop MoO_x . This highly conductive carbon-based structure permitted efficient ion diffusion and fast electron transport. Besides, the O-functional groups on the exfoliated graphite foil formed covalent C–O–Mo bonds with MoO_3 , which served as bridges that permitted fast charge transport from MoO_x to the substrate. All the above factors led to excellent rate capability: The optimized electrode with a high MoO_x mass loading of 15.4 mg cm^{-2} delivered an areal capacitance of 4.34 F cm^{-2} at 1 mA cm^{-2} and retained 67.8% of the initial capacitance at 20 mA cm^{-2} .

Films deposited onto fibers can develop unique morphologies, such as helical cracks demonstrated by Lu et al. They utilized a combined electrochemistry–annealing strategy and deposited hierarchical porous MoO_2 films composed of

mesoporous nanoparticles on carbon cloth fibers (Fig. 23h, i) [229]. First, mixed-valence MoO_x was electrochemically deposited on carbon cloth by reducing $\text{Mo}_7\text{O}_{24}^{6-}$:



Subsequently, the as-formed MoO_x was annealed in NH_3 at 700°C to obtain MoO_2 films. Scanning electron microscopy revealed that the MoO_2 films exhibited helical cracks of $\sim 100\text{--}200 \text{ nm}$ wide. Owing to the helical openings that reduced the dead volume of MoO_2 , the electrode delivered a high areal capacitance of 175 mF cm^{-2} at 1.43 mA cm^{-2} in Na_2SO_4 aqueous electrolytes. The formation mechanism of the helical cracks remained unclear, but we hypothesized that it might be associated with dehydration of the electrodeposited films during the thermal treatment in NH_3 . The cracks were initiated by volume shrinkage during annealing and propagated around carbon fibers following a helical path.

Like other pseudocapacitive materials, electrodeposited MoO_x exhibits high capacitance, but unsatisfactory cycling instability. To extend the life span of electrodeposited MoO_x , Cai et al. reported a potential window tuning strategy for MoO_x [38]. They discovered that the potential window within -1 to -0.4 V vs. SCE permitted the redox reaction associated with Mo^{4+} and Mo^{5+} and prevented the formation of Mo^{6+} . This feature resulted in no capacitance decay in 30,000 cycles. In contrast, the same electrode scanned between -1.0 and 0 V vs. SCE irreversibly generated Mo^{6+} and its capacitance decayed by more than 25% within 500 charge–discharge cycles. Electrochemical impedance spectroscopy revealed that the accumulation of Mo^{6+} increased the combined series resistance of MoO_x , which made the electrode electrically insulating. Besides, optimizing the composition of electrodeposited MoO_x materials via electrochemical technologies could provide new opportunities for enhancing their durability, as already proved to be successful in stabilizing VO_x [34].

5.4 Tungsten Oxides

Another transition metal oxide is tungsten oxides (WO_x) [230–233]. WO_x is usually deposited by cathodic deposition (e.g., applying a CV scan of $-0.5\text{--}0 \text{ V vs. SCE}$) [234] in aqueous electrolytes containing peroxy-tungstate species (e.g., $\text{W}_2\text{O}_{11}^{2-}$) [235–237]:

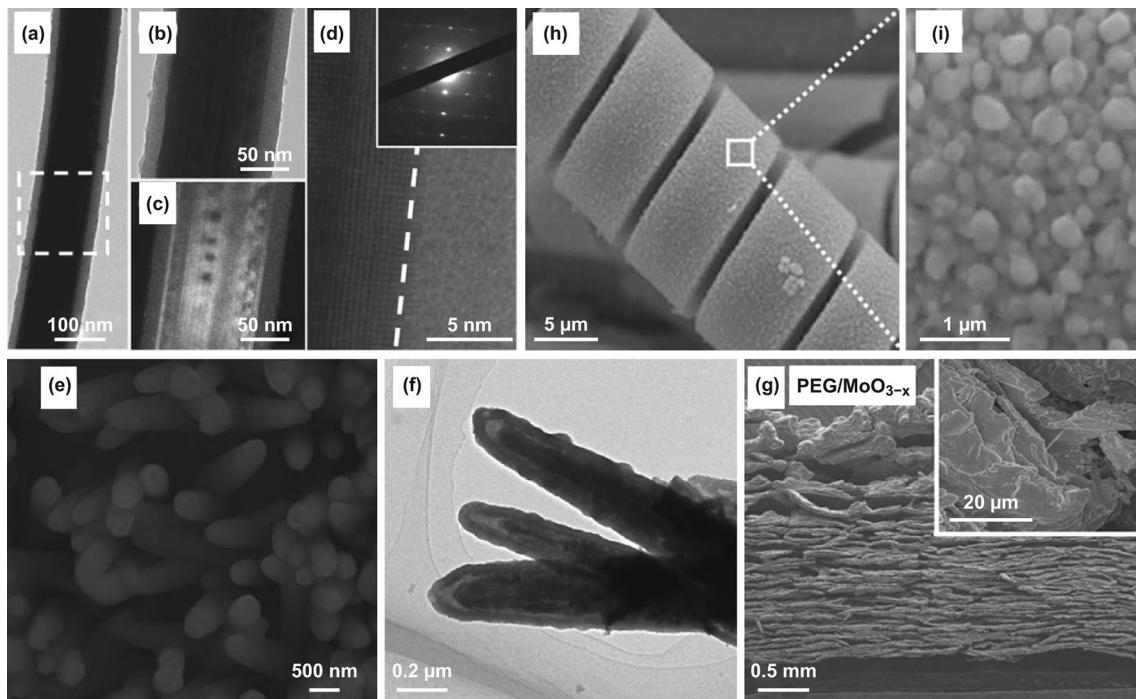
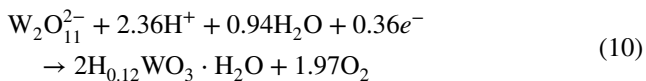
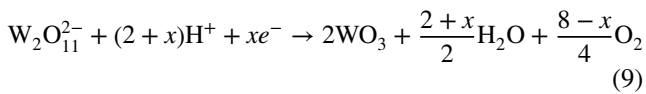


Fig. 23 **a–c** TEM images of a MoO_{3-x}-coated WO_{3-x} nanowire: **a, b** bright and **c** dark fields. **d** High-resolution TEM image of a MoO_{3-x}-coated WO_{3-x} nanowire. Inset: Selected electron diffraction pattern of WO_{3-x}. **e** An SEM and **f** TEM images of ZnO@MoO₃ core-shell structure. **g** A SEM image of MoO_{3-x} film deposited on an exfoliated graphite substrate. **h, i** SEM images of the helical porous MoO₂ with different magnifications. Adapted from **a–d** Ref. [226], **e, f** Ref. [227], **g** Ref. [228], **h** Ref. [229] with permission



Most as-deposited WO_x materials are amorphous with stacked, hydrated nanoparticles, WO_x·nH₂O [234, 238, 239]. Thermal annealing of WO_x·nH₂O at temperatures above 400 °C in air dehydrates the nanoparticles to crystalline WO_x [239, 240]. However, the annealing treatment usually triggers particle coalescence that decreases surface area. To circumvent this problem, Sun et al. developed an electrochemical post-crystallization process to convert electrodeposited amorphous, mixed-valence WO_x into crystalline tungsten bronze H_xWO₃ (Fig. 24a–c) [234]. The electrochemical crystallization process turned the non-porous film into highly porous nanosheets, enhancing specific surface area (Fig. 24d).

Changing electrolyte composition to extend the lower potential limit of WO_x electrodes is necessary to increase the capacitance and energy density of WO_x-based

supercapacitors. As a hydrogen evolution reaction (HER) catalyst, WO_x has a low potential of around –0.5 V vs. SCE [233]. Reducing pH values of electrolytes could push this limit to –1 V vs. SCE, but at the cost of cycling stability (Fig. 24e) [234, 241]. Sun et al. achieved both a low cut-off potential to –0.9 V vs. SCE and good cycling stability with 98% capacitance retained after 30,000 charge–discharge cycles by testing H_xWO₃ in a mixed electrolyte containing 1 M Na₂SO₄ and 0.01 M H₂SO₄ (Fig. 24f) [234]. XRD indicated that a new crystal phase (Na₆WO₆) formed after cycling in the Na₂SO₄ electrolyte (Fig. 24g), creating internal stress and detaching the active material from the current collector (carbon cloth fibers). While cycled in the mixed electrolyte, the structure of H_xWO₃ was well maintained. It was because, in proton-rich electrolytes, H⁺ insertion and de-insertion became the dominant charge storage mechanism, which was less destructive for the structure of H_xWO₃. Moreover, the mixed electrolyte enhanced the capacitance of H_xWO₃, as illustrated by the expanded area enclosed by the CV curve (Fig. 24h). Specifically, when tested in the mixed electrolyte, the electrode exhibited a high areal capacitance

of 860 mF cm^{-2} , corresponding to 143 F g^{-1} , at 5 mV s^{-1} (Fig. 24i). The rational design of electrolyte composition enabled electrodeposited WO_x electrodes with mutually high capacitance and excellent cycling stability.

5.5 Iron Oxides and Hydroxides

Iron oxides and hydroxides are one of the most attractive, low-cost negative electrode active materials for supercapacitors

[242–244]. Electrodeposition is a simple strategy to prepare nanostructured iron oxide and hydroxide [245]. Typically, Fe^{2+} (e.g., $\text{Fe}(\text{NH}_4)_2(\text{SO}_4)_2 \cdot 6\text{H}_2\text{O}$) is the iron source [35, 36, 246, 247]. During electrodeposition, Fe^{2+} is first oxidized to Fe^{3+} on positive electrodes, which then combines with OH^- that was present in weakly alkaline electrolytes ($\text{pH} \sim 8$) or dissociated from water reduction to form $\text{Fe}(\text{OH})_3$ deposits. The as-deposited $\text{Fe}(\text{OH})_3$ further dehydrates to FeOOH in air. The associated chemical reactions are [248]:

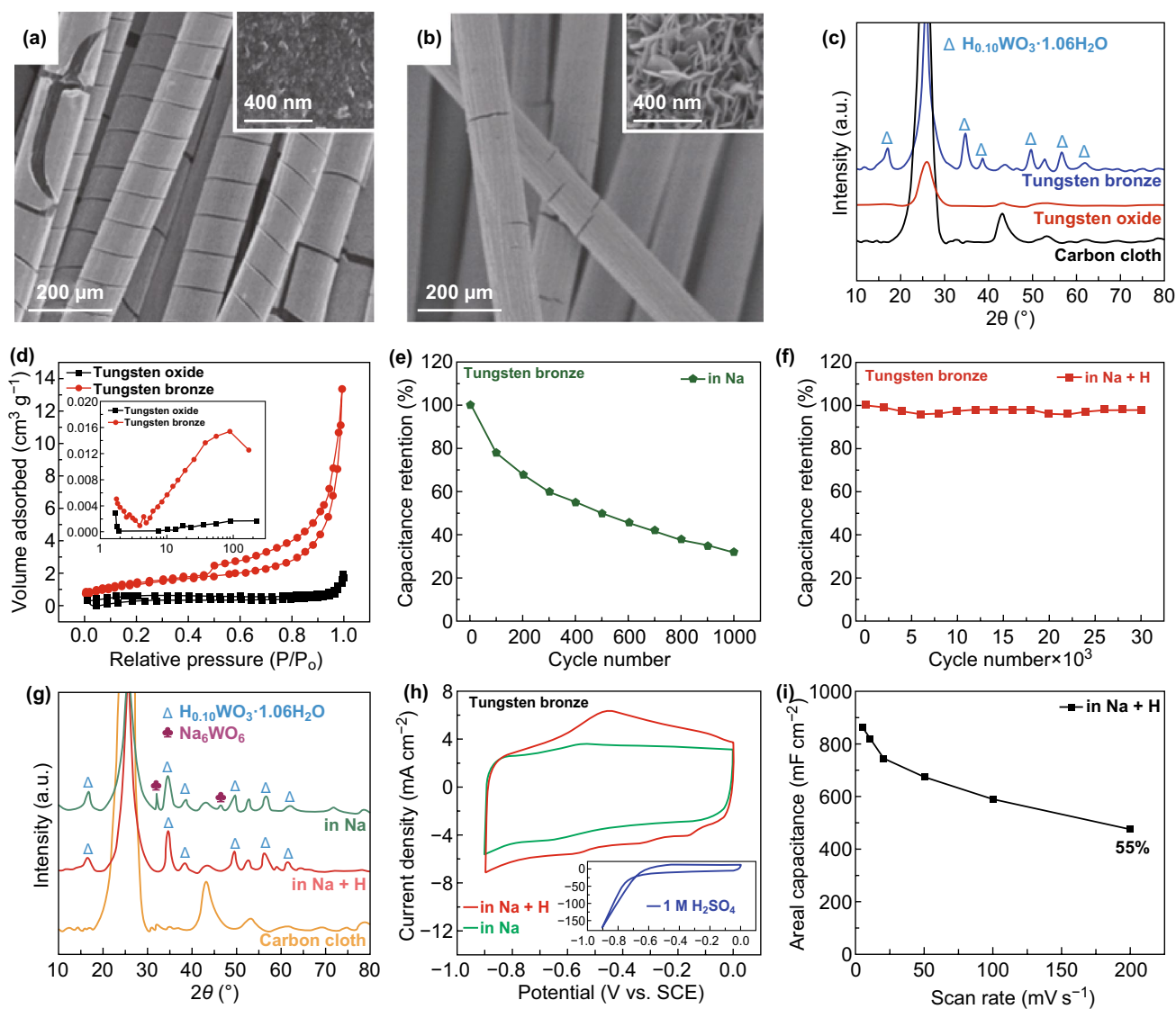
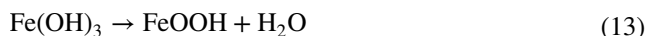


Fig. 24 **a, b** SEM images of **a** electrodeposited tungsten oxide and **b** tungsten bronze films on carbon cloth. **c** XRD patterns of tungsten oxide, tungsten bronze, and carbon cloth. **d** N_2 adsorption–desorption isotherms of tungsten oxide and tungsten bronze. Inset: pore size distributions. **e, f** Cycling stability of tungsten bronze in **e** $1 \text{ M Na}_2\text{SO}_4$ and **f** $\text{Na}_2\text{SO}_4/\text{H}_2\text{SO}_4$ ($1 \text{ M}/0.01 \text{ M}$) mixed aqueous electrolytes. **g** XRD patterns of tungsten bronze after cycled in Na_2SO_4 and $\text{Na}_2\text{SO}_4/\text{H}_2\text{SO}_4$. **h** CV curves of tungsten bronze in Na_2SO_4 (green), $\text{Na}_2\text{SO}_4/\text{H}_2\text{SO}_4$ (red), and H_2SO_4 (blue) aqueous electrolytes. **i** Rate capability of tungsten bronze in $\text{Na}_2\text{SO}_4/\text{H}_2\text{SO}_4$. Adapted from Ref. [234] with permission



To date, iron oxides of different dimensionalities, including 0D nanoparticles (Fig. 25a) [249], 1D nanorods (Fig. 25b) [250], 2D nanosheets (Fig. 25c) [251], and 3D hierarchical structures (Fig. 25d) [35], have been synthesized electrochemically. For example, Mai et al. reported a cyclic voltammetry method that transformed highly crystalline Fe_2O_3 nanoparticles into low-crystalline FeOOH nanoparticles (Fig. 25a) [249]. The resultant FeOOH electrode, with a high mass loading of 9.1 mg cm^{-2} , exhibited an outstanding specific capacitance of 716 F g^{-1} at 1 A g^{-1} in 2 M KOH electrolyte. The specific capacitance was attributed to the facilitated ion diffusion kinetics in the FeOOH electrode, but further studies were needed to unveil the mechanism fully.

As electrodeposited iron species are typically $\text{Fe}(\text{OH})_3$ and FeOOH, thermal conversion to Fe_2O_3 with enhanced electrochemical activity is usually performed for processing supercapacitor electrodes [252]. For example, FeOOH nanoneedles were first deposited on Ni-plated ZnO nanorods using a constant potential of $1.5 \text{ V vs. Ag/AgCl}$ [253]. During the electrodeposition, the acidic environment created by Fe^{3+} hydrolysis corroded the ZnO nanorods, forming Ni@FeOOH. Subsequent annealing Ni@FeOOH in Ar at $450 \text{ }^\circ\text{C}$ dehydrated FeOOH to Ni@ Fe_2O_3 nanoneedles. The Ni nanotubes swiftly conducted electrons between Fe_2O_3 and the substrate, while the ultrathin thickness of Fe_2O_3 nanosheets endowed fast charge transfer kinetics. Benefiting from these merits, Ni@ Fe_2O_3 achieved a high specific capacitance of 418 F g^{-1} at 10 mV s^{-1} in the potential window from -0.8 to 0 V vs. Ag/AgCl , excellent rate capability (215 F g^{-1} at 64 A g^{-1}), and cycling stability (93% capacitance retention after 5000 charge–discharge cycles).

In addition to thermal annealing, chemical conversion in hot alkaline solutions represents another means to convert electrodeposited FeOOH into iron oxides. Chemical conversion avoids high-temperature annealing that may trigger structural deformation and particle agglomeration. One excellent example was demonstrated by Sun et al. [35]. They utilized a post-chemical transition method to obtain composite mesoporous iron oxides (Fe_3O_4 and Fe_2O_3) from electrodeposited FeOOH nanosheets on a 3D exfoliated

graphite substrate (EG). First, FeOOH nanosheets were deposited on EG using a potentiostatic method (-0.5 V vs. SCE for 80 min in an aqueous electrolyte containing $0.05 \text{ M Fe}(\text{NH}_4)_2(\text{SO}_4)_2$ and $0.05 \text{ M }(\text{NH}_4)_2\text{SO}_4$). Afterward, the as-deposited nanosheets were immersed in a 1 M NaOH aqueous solution for 1 h at $70 \text{ }^\circ\text{C}$ to convert iron oxy-hydroxides to iron oxide (containing Fe_2O_3 and Fe_3O_4) nanosheets interconnected into a honeycomb-like structure (Fig. 25d). The conversion mechanism is unclear, but we hypothesize that it is associated with dehydration of iron oxy-hydroxides during the treatment. High-resolution SEM image presented that each oxide nanosheet was composed of nanoparticles (Fig. 25d inset). The EG@ $\text{Fe}_3\text{O}_4/\text{Fe}_2\text{O}_3$ electrode delivered an ultrahigh areal capacitance of 1.57 F cm^{-2} at 5 mA cm^{-2} , corresponding to 165 F g^{-1} based on the total mass of the electrode. The excellent capacitive performance of the EG@ $\text{Fe}_3\text{O}_4/\text{Fe}_2\text{O}_3$ electrode was ascribed to several factors. First, the hierarchically porous structure with mesopores and macropores in the electrode shortened ion diffusion distance. Second, the heterojunction between $\text{Fe}_3\text{O}_4/\text{Fe}_2\text{O}_3$ introduced a built-in electric field that facilitated charge transfer between different oxide particles. Third, the interconnected graphene sheets on EG constructed highly conductive electron transport networks that minimized capacitance loss at fast discharging rates.

5.6 Nickel/Cobalt Oxides and Hydroxides

A critical issue that we would like to highlight first in this section is the concepts of intrinsic and extrinsic pseudocapacitive materials. Intrinsic pseudocapacitive materials refer to materials that always show pseudocapacitive characteristics (CV curves with broad or no redox peaks and plateau-free charge–discharge profiles) irrespective of size. Extrinsic pseudocapacitive materials exhibit pseudocapacitive signatures only at nanoscales. This transition of the electrochemical behaviors of extrinsic pseudocapacitive materials was due to the reduced ion diffusion distance that accelerated charge storage kinetics and, in some cases, suppressed phase transformations [13].

Nickel and cobalt oxides and hydroxides are extrinsic pseudocapacitive materials [254]. Charge storage in their bulk forms involves phase transitions, resulting in apparent redox peaks in CV curves (Fig. 26a) and plateaus in galvanostatic charge–discharge profiles (Fig. 26b) [255]. Therefore, these battery-like materials have been used as electrodes in

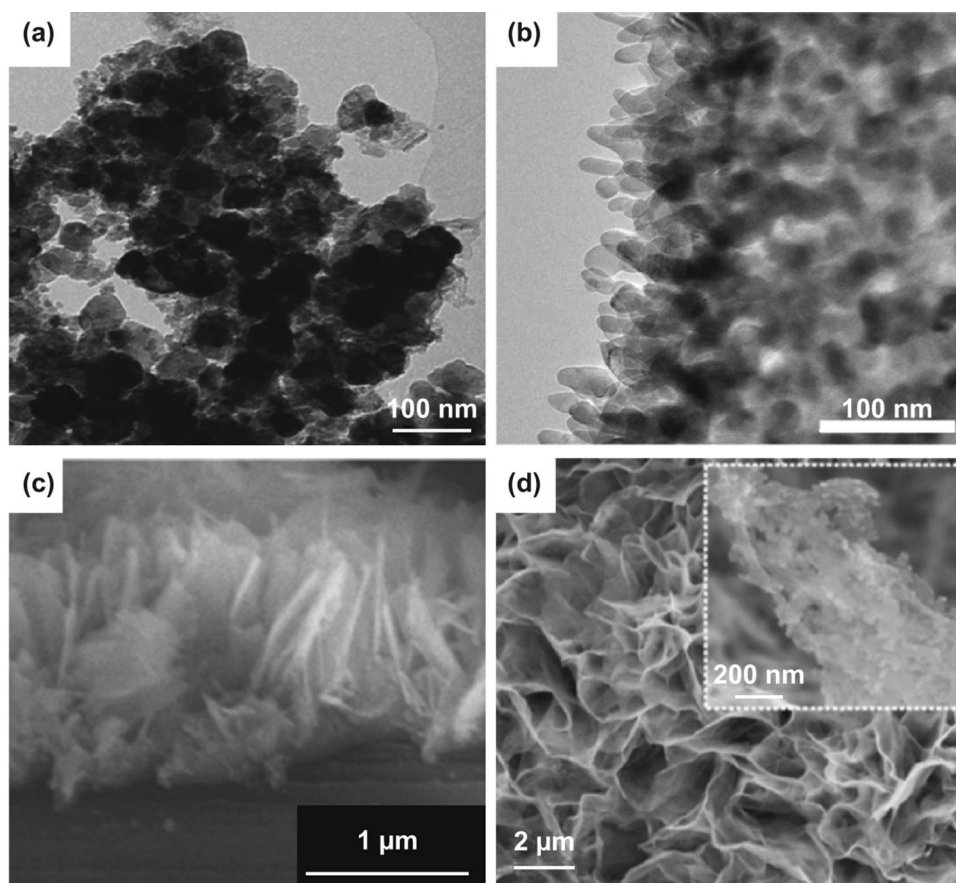
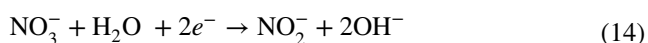


Fig. 25 **a, b** TEM images of **a** electrodeposited FeOOH nanoparticles and **b** Fe₂O₃ nanorods. **c, d** SEM images of electrodeposited FeOOH nanosheets and **d** chemically converted Fe₃O₄/Fe₂O₃ nanosheets. Inset: Magnified view of a nanosheet. Adapted from **a** Ref. [249], **b** Ref. [250], **c** Ref. [251], **d** Ref. [35] with permission

aqueous batteries [256–258] or battery-type electrodes in hybrid supercapacitors [96, 259–261], but cannot be studied in the context of pseudocapacitors. However, once their size shrinks to nanoscales, their pseudocapacitive features will emerge [262–266], as indicated by the broad redox peaks in CV curves (Fig. 26c) and sloping charge–discharge profiles (Fig. 26d) [267].

Nickel and cobalt (hydro)oxides are electrochemically synthesized via cathodic deposition in aqueous solutions. Ni²⁺ or Co²⁺ combines with OH[−] produced from water or anions in electrolytes. Taking Co(OH)₂ as an example, one reported electrodeposition mechanism in Co(NO₃)₂ aqueous solutions is [268]:



Guo et al. have recently demonstrated a converse voltage strategy to activate electrodeposited Co(OH)₂ nanosheets on carbon fibers (Fig. 27a) [268]. First, Co(OH)₂ nanosheets were electrodeposited with a constant potential of −1.5 V vs. SCE (Fig. 27b). The voltage then reversed (1.5 V vs. SCE) (Fig. 27c), triggering a phase transition from Co(OH)₂ to low-crystalline CoOOH (denoted as EA-CoOOH) containing abundant structural defects (oxygen vacancies, lattice disorders, and interconnected mesopores) (Fig. 27d). Quantitative analyses on the electrode kinetics revealed that the capacitance of EA-CoOOH contributing from kinetically fast, surface-controlled processes occupied 93% at 5 mV s^{−1}, and further increased to 99% at 100 mV s^{−1}. The nanosheets and defects altered the intrinsic battery-type behavior of CoOOH to pseudocapacitive characteristics. Outstandingly, EA-CoOOH electrode exhibited substantially enhanced capacitance than Co(OH)₂ and deeply oxidized O-CoOOH

electrode (Fig. 27e), delivering a high specific capacitance of 832 F g^{-1} at 1 A g^{-1} and retained 78% of the capacitance (649 F g^{-1}) at 200 A g^{-1} (Fig. 27f).

Introducing a secondary cation, such as Fe^{3+} and Al^{3+} , in Ni/Co hydroxides to form double hydroxides have been proved to enhance capacitive performance due to charge hopping or valence interchange between different cations [96, 266, 269, 270]. Double hydroxides usually possess layered structures with large interlayer spacings (e.g., $\sim 1 \text{ nm}$), which resulted in their high specific capacitance (e.g., $> 2000 \text{ F g}^{-1}$) [96, 106, 271]. Unfortunately, their limited potential windows in alkaline electrolytes ($\sim 0.5 \text{ V}$) and poor rate performance still hinder their large-scale applications in aqueous batteries and supercapacitors. Neutral aqueous electrolytes can suppress appreciable oxygen evolution in alkaline solutions and thus extend the potential window of layered double hydroxides (LDHs) to $\sim 1 \text{ V}$.

Since anions residing between the interlayer space and the electrostatic repulsion from positively charge LDH laminate, cation intercalation into LDHs in neutral electrolytes

remains thermodynamically unfavorable, resulting in unsatisfactory electrochemical performance. Recently, Li et al. have demonstrated an electrochemical strategy to ease the cation intercalation into LDHs in neutral electrolytes [272]. Co–Fe LDH nanoplates were first electrodeposited on Ni foam using a cathodic electrodeposition method (Fig. 28a). Subsequently, electrochemical activation (EA) of the Co–Fe LDH nanosheets was conducted by CV between 0 and 0.6 V vs. SCE in KOH or NaOH electrolyte (denoted as EA–Co–Fe LDH). The obtained electrode exhibited pronounced electrochemical activity in various aqueous electrolytes, including NaNO_3 , KNO_3 , $\text{Ca}(\text{NO}_3)_2$, $\text{Mg}(\text{NO}_3)_2$, $\text{Zn}(\text{NO}_3)_2$ between 0 and 1 V vs. SCE (Fig. 28b, c). The specific capacitance of EA–Co–Fe LDH in NaNO_3 reached 417 F g^{-1} , which was 27 times higher than that of as-deposited Co–Fe LDH nanoplates. XRD, XPS, FTIR, and X-ray absorption near-edge structure (XANES) all indicated that during the electrochemical activation, $\text{Co}(\text{OH})_2$ in CoFe-LDH was oxidized to CoOOH , resulting in hydrogen vacancies and removal of carbonate anions residing within the interlayer space of

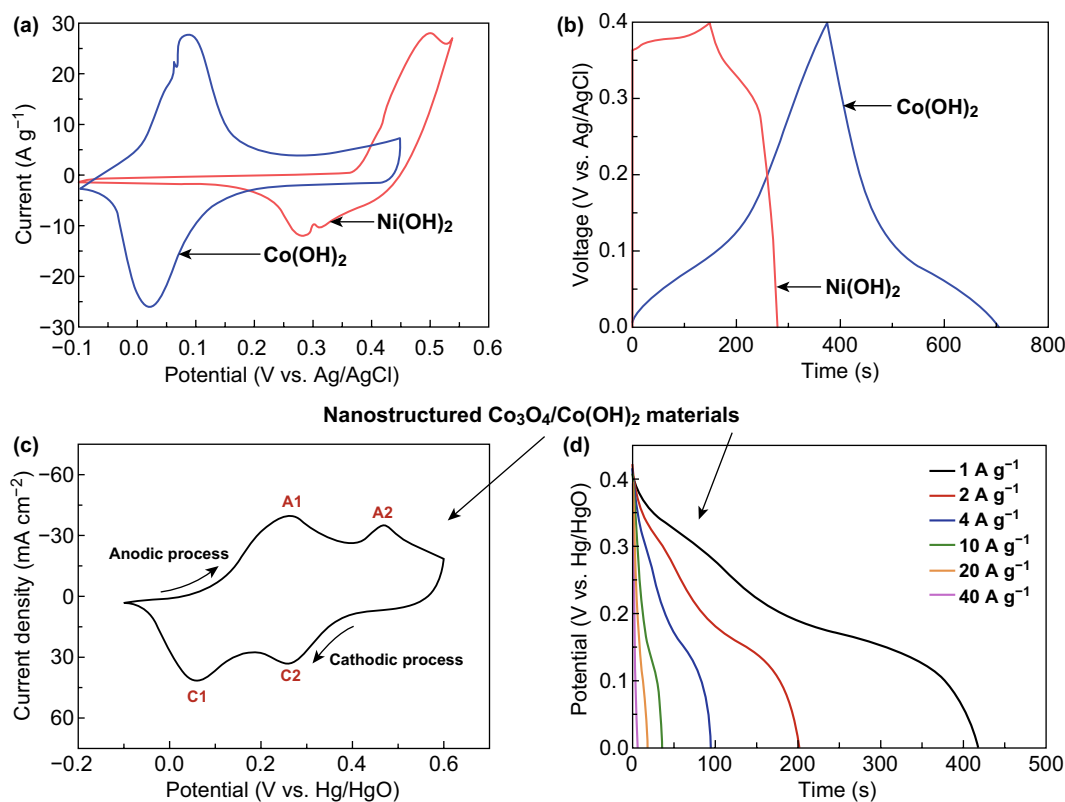


Fig. 26 **a** CV curves and **b** galvanostatic charge–discharge profiles of $\text{Co}(\text{OH})_2$ (blue) and $\text{Ni}(\text{OH})_2$ (red). **c** CV curves and **d** galvanostatic charge–discharge profiles of $\text{Co}_3\text{O}_4/\text{Co}(\text{OH})_2$ core/shell nanowire arrays. Adapted from **a**, **b** Ref. [255], **c**, **d** Ref. [267] with permission

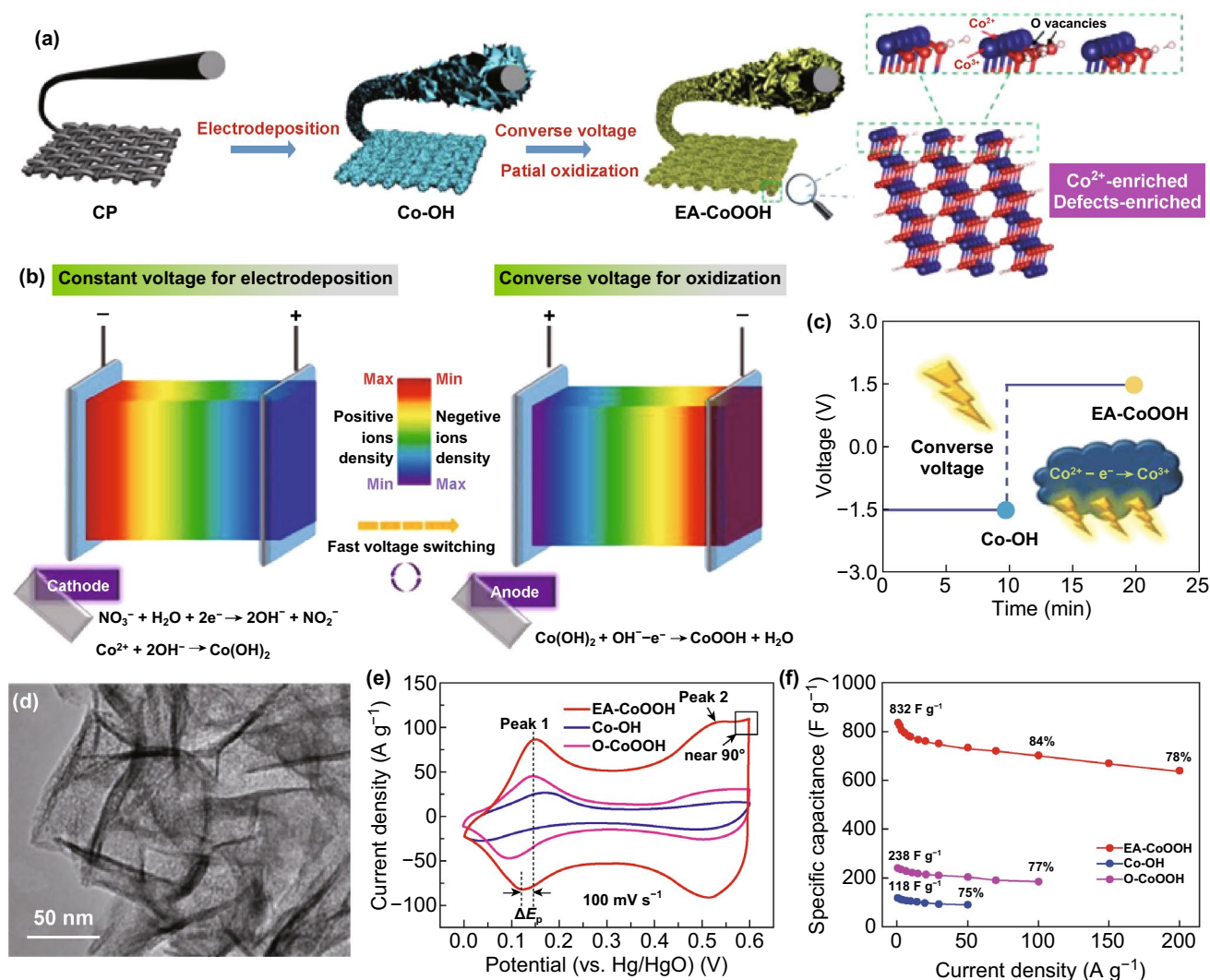


Fig. 27 a Schemes of the synthesis steps of EA-CoOOH by a converse voltage method and the molecular structure of Co²⁺- and defect-rich EA-CoOOH. b Schemes showing the ion concentration gradients during constant voltage for electrodeposition (left) and converse voltage for oxidation (right). c Voltage profiles of electrodeposition and converse voltage stages. d TEM image of EA-CoOOH. e CV curves and g rate capability of EA-CoOOH in comparison with other electrodes. Adapted from Ref. [268] with permission

CoFe-LDH (Fig. 28d). Density functional theory calculations elucidated the adsorption sites of metal ions in LDH and EA-LDH materials (Fig. 28e). The results suggested that the adsorption of metal ions (Li⁺, Na⁺, K⁺, Ca²⁺, Mg²⁺, and Zn²⁺) on terminal H was unfavorable, whereas adsorptions of the same set of ions on O termination were thermodynamically stable, as reflected from the negative adsorption energy (Fig. 28e, blue bars). The enhanced adsorption tendency with O terminals was ascribed to the H vacancies formed during the activation step. Taking together, the formation of H vacancies and extraction of interlayer anions

after the electrochemical activation together imparted the ion intercalation capability of CoFe-LDH in neutral electrolytes.

6 Composites

Composites that combine the merits of two or more materials are versatile electrode candidates for supercapacitor electrodes. These composites are typically electrodeposited through a one-step co-electrodeposition. The reported electrodeposited composites are classified according to their

constituent species, including composites having the same group of materials, such as oxide/oxide (manganese oxide/molybdenum oxide [273, 274], nickel manganese oxide [275], molybdenum oxide/tungsten oxide [276]), and composites with different types of materials, including oxide/conducting polymer (polypyrrole/manganese oxide [277, 278], manganese oxide/polyaniline [279, 280], manganese

oxide/poly(3,4-ethylenedioxythiophene):poly(styrenesulfonate) [281, 282], polyaniline/vanadium oxide [27], polypyrrole/vanadium oxide [283, 284], polypyrrole/molybdenum oxide [285], polyaniline/tungsten oxide [286]) and oxide/hydroxide (NiAl-layered double hydroxide/manganese oxide [287] and manganese oxide/nickel hydroxide [288]). Their capacitance and corresponding synthesis methods

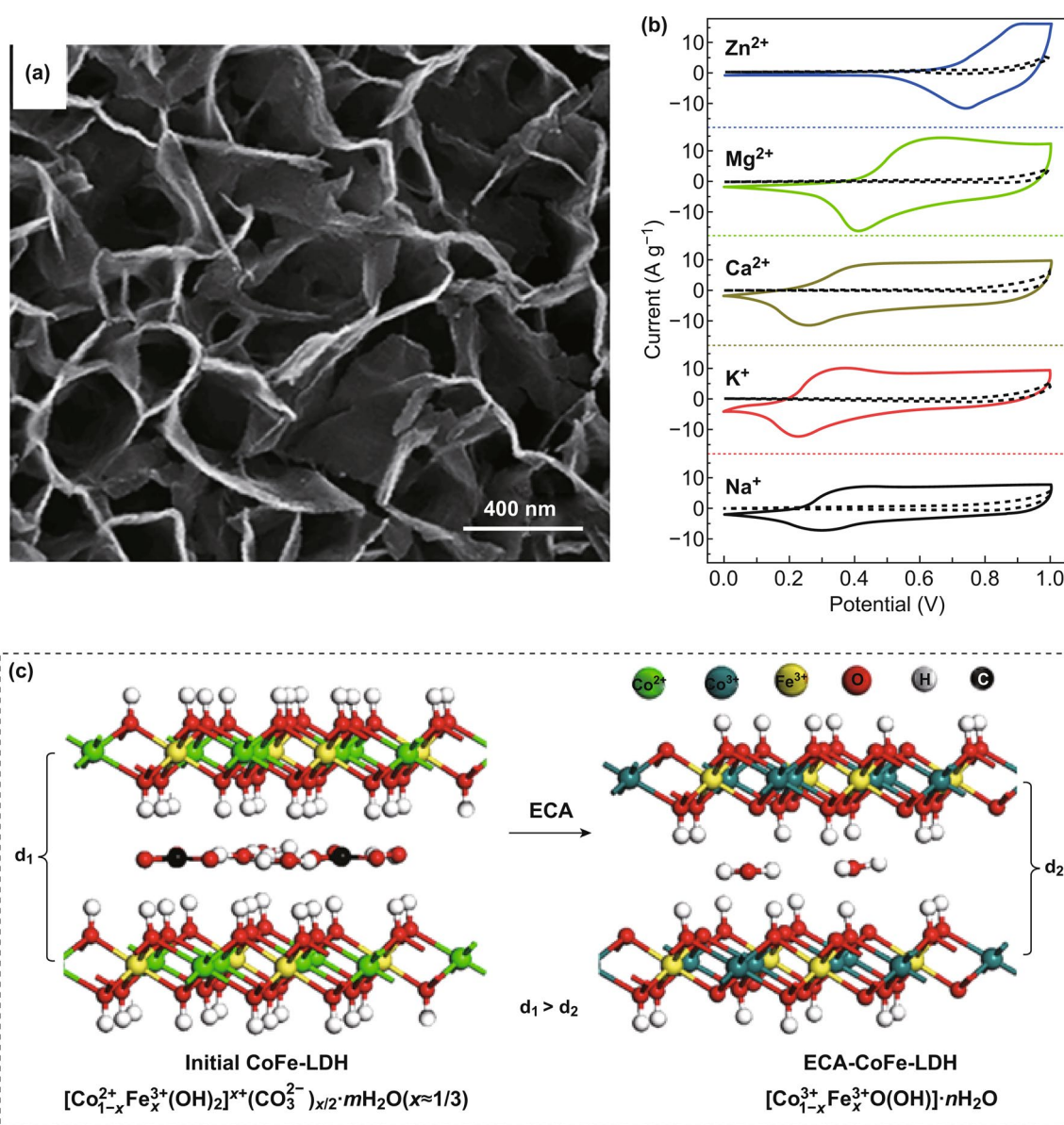


Fig. 28 **a** SEM image of CoFe layered double hydroxide (LDH) nanoplates. **b** CV curves and **c** galvanostatic charge–discharge profiles of CoFe-LDH in different aqueous solutions. **d** Evolution of the crystal structure and composition of CoFe-LDH before and after electrochemical activation. **e** Adsorption energies of various metal ions over H-terminated (magenta) and O-terminated (blue) LDH laminates. Reproduced from Ref. [272] with permission

are summarized in Table 2. Electrodeposited composites usually exhibit advantages of synergies and strong interactions among the incorporated materials that exhibit superior capacitive performance to the corresponding single-component counterparts.

Not all the active materials are co-electrodepositable in one step. One prerequisite is that the materials to be compounded must be synthesizable under similar electrochemical conditions, including pH value, polarization potential, current density, and temperature. For example, Zou et al. electrodeposited a tungsten oxide and polyaniline composite via one-step cyclic voltammetry in a mixed acidic electrolyte containing tungstic acid and aniline monomers [289]. The success of the co-deposition was owing to the acidic environment needed for both tungsten oxide and polyaniline. In contrast to the densely stacked tungsten oxide particles, the composite possessed widened pores and interconnected particles. This difference in the morphology was ascribed to the incorporated polyaniline, which acted as a structural scaffold that prevented the aggregation of tungsten oxide particles. The composite electrode exhibited enhanced pseudocapacitive performance over a wide potential window from -0.5 to 0.7 vs. SCE, which combined the potential windows of polyaniline (-0.1 – 0.7 V vs. SCE) and tungsten

oxide (-0.5 – 0.3 V vs. SCE). The synergistic effects between polyaniline and tungsten oxide improved the capacitive performance of the composite. Tungsten oxide offered high pseudocapacitance. Polyaniline created interparticle pores that increased surface area and conducted electrons to maintain superior rate capability to those of bare tungsten oxide or polyaniline.

Another example is a series of molybdenum–tungsten mixed oxide composites co-electrodeposited into titanium dioxide nanotube arrays using a one-step galvanostatic plating [276]. The plating electrolyte was an aqueous mixture of different concentrations of sodium molybdate dihydrate, sodium tungstate dihydrate, ethylenediamine tetra-acetic acid disodium, and ammonium acetate. The as-electrodeposited amorphous Mo–W mixed oxide film was thermally annealed at 450 °C in air to improve its crystallinity. The similarities in the valence state, ionic radius, and electronegativity of W^{6+} and Mo^{6+} were the keys to the successful co-deposition. XRD and Raman spectroscopy indicated that the fabricated Mo–W mixed oxides were monoclinic, and the crystal structure transitioned from m - WO_3 -like to β - MoO_3 -like when increasing the Mo/W ratio (Fig. 29a). Though pure MoO_3 exhibited higher capacitance than the composite electrodes at 20 $mV s^{-1}$ (Fig. 29b), its rate capability

Table 2 Different types of composites synthesized via electrochemical methods

Component #1	Component #2	Synthesis method	Capacitance	References
<i>Conducting polymer–metal oxide</i>				
Polypyrrole	MnO_x	Galvanostatic deposition	$463 F g^{-1}@2 A g^{-1}$	[277]
Polyaniline	MnO_x	Cyclic voltammetry	$415 F g^{-1}@1.67 mA cm^{-2}$	[279]
		Pulse potential	$90.25 F g^{-1}@1 mA g^{-1}$	[280]
Poly(3,4-ethylenedioxythiophene):poly(styrenesulfonate)	MnO_x	Constant potential	$1.67 F cm^{-2}@0.5 mA cm^{-2}$	[281]
		Constant potential	$386 mF cm^{-2}@1 mA cm^{-2}$	[282]
Polyaniline	VO_x	Cyclic voltammetry	$0.66 F cm^{-2}@0.5 mA cm^{-2}$	[27]
Polypyrrole	VO_x	Constant potential	$750 F g^{-1}@5 A g^{-1}$	[283]
		Constant potential	$412 F g^{-1}@4.5 mA cm^{-2}$	[284]
Polypyrrole	MoO_x	Cyclic voltammetry	$398 F g^{-1}@1 A g^{-1}$	[285]
Polyaniline	WO_x	Cyclic voltammetry	$408 F g^{-1}@1 A g^{-1}$	[286]
<i>Metal oxide–metal oxide</i>				
MnO_x	MoO_x	Cyclic voltammetry	$21 mF cm^{-2}@50 mV s^{-1}$	[273]
		Galvanostatic deposition	$408 F g^{-1}@2 mV s^{-1}$	[274]
$NiMnO_x$		Cyclic voltammetry	$961.5 F g^{-1}@10 mV s^{-1}$	[275]
MoO_x	WO_x	Galvanostatic deposition	$517.4 F g^{-1}@1 A g^{-1}$	[276]
<i>Hydroxide–metal oxide</i>				
NiAl-layered double hydroxide	MnO_x	Constant potential	$1554 F g^{-1}@1 A g^{-1}$	[287]
Nickel hydroxide	MnO_x	Constant potential	$344 F g^{-1}@0.5 A g^{-1}$	[288]

(Fig. 29c) and cycling stability (Fig. 29d) were inferior to those of the composites. Among all the synthesized Mo–W mixed oxides, 0.5MoW with a Mo/W ratio of 1 achieved the best electrochemical performance: high specific capacitance of 517.4 F g^{-1} at 1 A g^{-1} and good capacitance retention of 89.3% at 10 A g^{-1} . The enhanced rate capability of the composites over that of MoO_3 was attributed to two factors. First, the long-range ordered structure of pure oxides was disrupted in the mixed oxides, which decreased crystal size, increased surface area, and facilitated ion diffusion. Second, the disordered monoclinic crystal structure of the mixed oxides yielded a larger lattice space than those of WO_3 and MoO_3 alone, resulting in decreased ion diffusion resistance.

Recently, Zhang et al. have demonstrated a facile cyclic voltammetry method capable of depositing coupled strongly, layer-by-layer PPy/ MoO_x composite films on 3D exfoliated graphite substrates (Fig. 30a) [285]. MoO_x layer was first deposited on graphite foil during the cathodic scan, while the PPy layer was subsequently grown on MoO_x in the following anodic scan. Therefore, a layer-by-layer PPy/ MoO_x structure was obtained after multiple depositions (Fig. 30b–d). In addition, Fourier transform infrared spectroscopy and X-ray

photoelectron spectroscopy detected the reduction in Mo valence and the enhancement of protonation level of PPy, both of which resulted from the strong coupling between PPy and MoO_x (Fig. 30h) that are beneficial for enhancing the electrochemical performance. The composite electrode exhibited a specific capacitance of 398 F g^{-1} at 1 A g^{-1} , higher than those of PPy (160 F g^{-1}) and MoO_x (320 F g^{-1}) at identical current density (Fig. 30i–k).

Besides one-step co-electrodeposition, composites have been prepared using multistep electrodeposition methods [290–294]. For example, Wang and Cai et al. synthesized a $\text{VO}_x@/\text{MoO}_3$ composite through a two-step electrochemical deposition. VO_x nanorods were first grown on carbon cloth by cyclic voltammetry (Fig. 31a) [295]. Subsequently, a thin layer of MoO_3 was coated on the VO_x nanorods by a constant current deposition for 9 s (Fig. 31b, c). The composite electrode $\text{VO}_x@/\text{MoO}_3$ displayed an areal capacitance of 1980 mF cm^{-2} at 2 mA cm^{-2} , against 1309 mF cm^{-2} of VO_x and 233 mF cm^{-2} of MoO_3 under identical testing conditions. Fourier transform infrared spectroscopy revealed that the V–O–V peaks of $\text{VO}_x@/\text{MoO}_3$ blueshifted in comparison with that of VO_x (Fig. 31d). The V $2p_{3/2}$ XPS spectrum

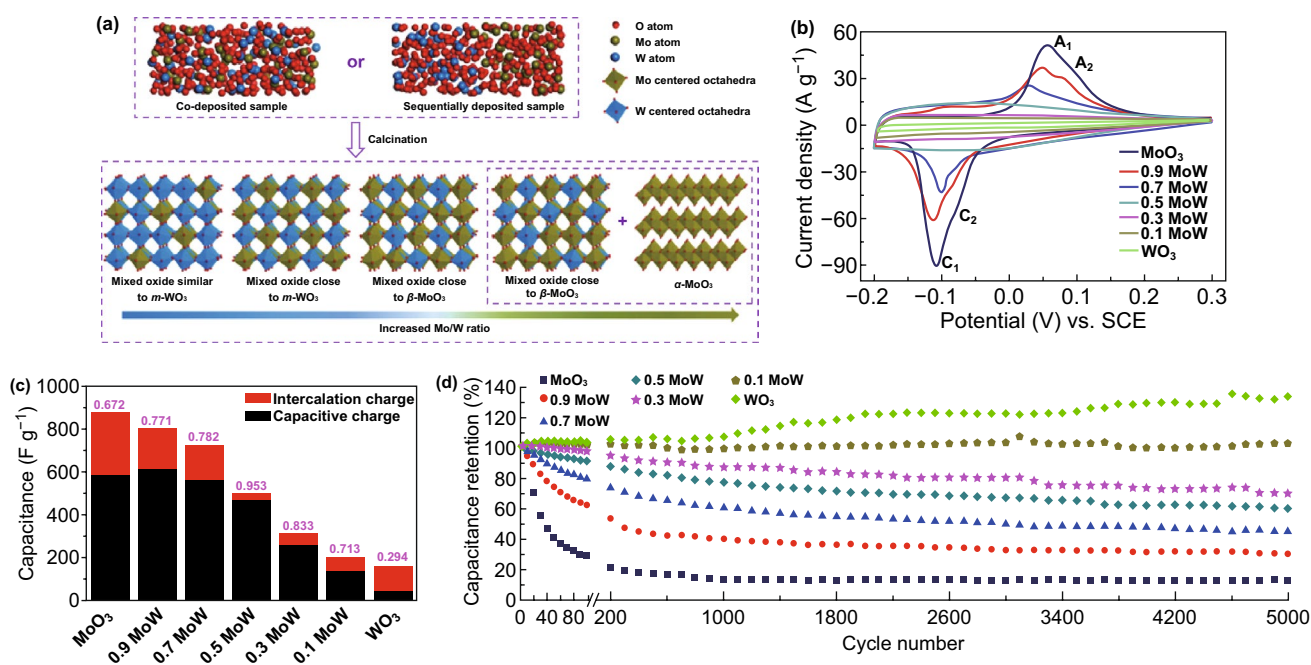


Fig. 29 a Schemes of the formation mechanism and crystal structure of Mo–W mixed oxides. b CV curves, c capacitance contributions (capacitive vs. diffusion-controlled processes), d cycling stability, and e ion transport patterns of different Mo–W mixed oxides. Reproduced from Ref. [276] with permission

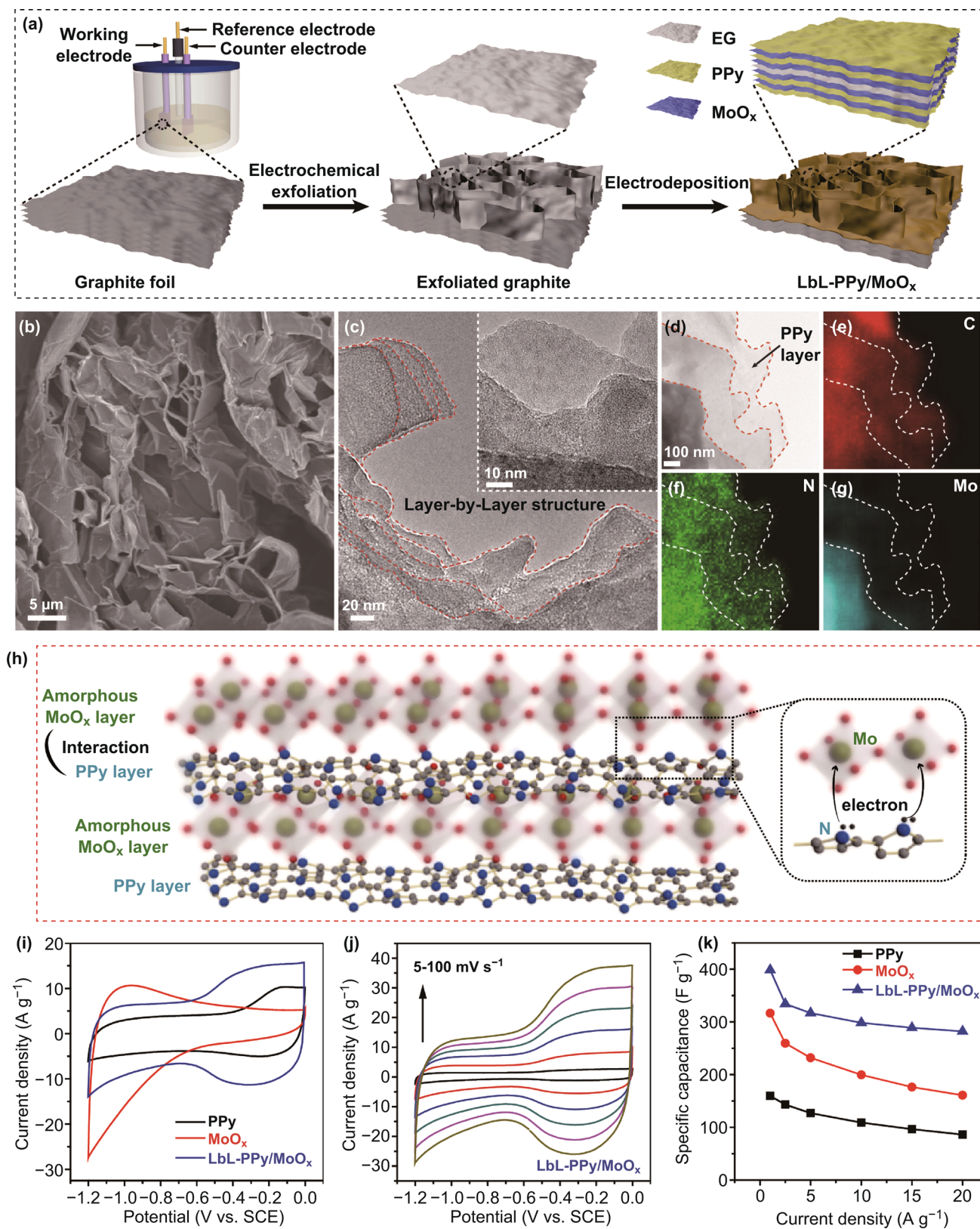


Fig. 30 **a** Schemes of the synthesis steps, **b** SEM image, **c** TEM image, and **d-g** elemental mappings of layer-by-layer PPy/MoO_x. **h** Interactions between PPy and MoO_x layers. **i** CV curves of PPy, MoO_x, and PPy/MoO_x. **j** CV curves of PPy/MoO_x at different scan rates. **k** Rate capability of PPy, MoO_x, and PPy/MoO_x. Reproduced from Ref. [285] with permission

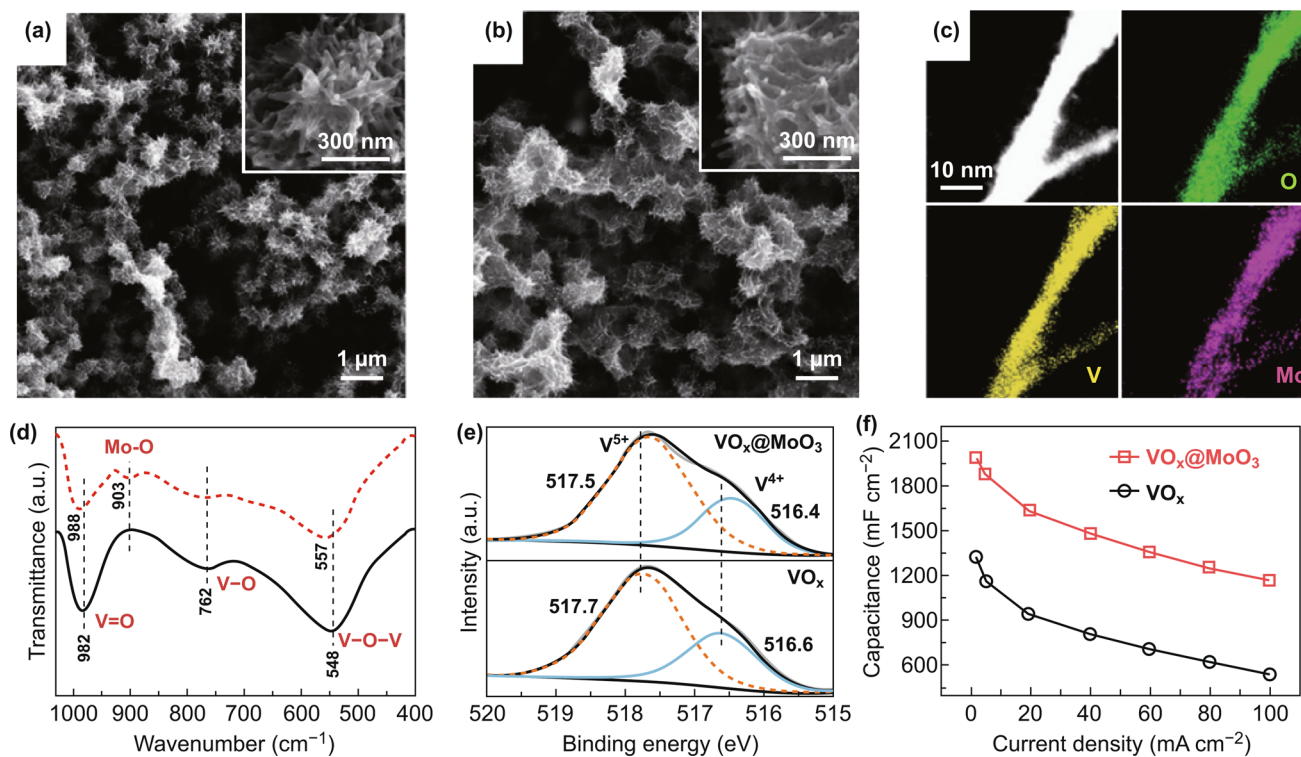


Fig. 31 **a, b** SEM images of **a** VO_x and **b** $\text{VO}_x@MoO_3$. **c** Elemental mappings of $\text{VO}_x@MoO_3$. **d** FTIR spectra of VO_x and $\text{VO}_x@MoO_3$. **e** $V 2p_{3/2}$ XPS spectra of VO_x and $\text{VO}_x@MoO_3$. **f** Areal capacitances of VO_x and $\text{VO}_x@MoO_3$ as a function of current density. Reproduced from Ref. [295] with permission

showed that the binding energies of both V^{5+} and V^{4+} of $\text{VO}_x@MoO_3$ downshifted by 0.2 eV. Both results indicated that the electronic structure and chemical environment of VO_x in $\text{VO}_x@MoO_3$ were modified by the strong interaction between VO_x and MoO_3 , accounting for the improved capacitive performance. Specifically, $\text{VO}_x@MoO_3$ reached a high areal capacitance of 1980 mF cm^{-2} at 2 mA cm^{-2} , exceeding 1309 mF cm^{-2} of VO_x (Fig. 31f). Strong interaction among the incorporated materials is indispensable in realizing the synergy of the composite electrodes. Poor interactions will not only interrupt electron transport but also induce structural instability of composite [296].

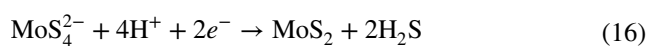
7 Other Materials

Electrodeposition has occasionally been used to synthesize nano-/microstructured sulfides [297–300], polyanionic compounds [28], and selenides [301]. These materials typically exhibit higher capacitance than their corresponding oxides due to the different chemical environments created

by substituting oxygen near the redox sites, which enhanced electrical conductivity or led to crystal structures favorable for fast ion diffusion, e.g., channels, slits, and pores [28, 297, 302, 303]. Electrochemical syntheses of these materials usually proceed in electrolytes containing precursors of sulfide, phosphate, or selenide.

Using a one-step electrochemical co-deposition method, Chen et al. electrodeposited ternary nickel–cobalt sulfide nanosheets on carbon cloth [302]. The electrodeposition was conducted in a three-electrode electrolytic cell containing 5 mM CoCl_2 with different concentrations of NiCl_2 (1, 2.5, 5, 7.5, and 10 mM) and 0.75 M thiourea. The deposition technique was cyclic voltammetry within a potential range between -1.2 and 0.2 V vs. Ag/AgCl at 5 mV s^{-1} for 15 cycles. SEM displayed that the electrodeposited materials formed a dense array of highly porous nanosheets. High-angle annular dark-field scanning transmission electron microscopy (HAADF-STEM) and energy-dispersive X-ray spectroscopy (EDS) confirmed the uniform distributions of Co, Ni, and S in the deposited nanosheets. The as-deposited sulfide exhibited extrinsic pseudocapacitive characteristics

of symmetric and plateau-free charge–discharge profiles. The sulfide with an optimal Ni-to-Co ratio (Ni–Co–S-4) showed the highest specific capacitance of 1418 F g^{-1} at 5 A g^{-1} among all Ni–Co–S compounds. It retained 90.6% of its initial capacitance when the current density increased to 100 A g^{-1} . Falola et al. synthesized MoS_2 film on a glass carbon electrode using an electrochemical deposition coupled with thermal annealing [300]. The electrochemical deposition was conducted via a CV scan from -1.2 to 1 V vs. Ag/AgCl in an aqueous electrolyte containing 10 mM $(\text{NH}_4)_2\text{MoS}_4$ and 0.2 M KCl at $\text{pH} = 6.8$, following the reaction [304]:



The as-deposited MoS_2 was thermally annealed under Ar at $600 \text{ }^\circ\text{C}$ to increase its crystallinity. The resultant MoS_2 film exhibited a gravimetric capacitance of $\sim 500 \text{ F g}^{-1}$ at 0.75 A g^{-1} . Increasing the film thickness from 50 to 200 nm decreased the capacitance to $\sim 100 \text{ F g}^{-1}$, which could be due to the sluggish ion diffusion kinetics throughout the thick films.

Molybdenophosphate (A–Mo–O–P, A = Na, K, etc.) materials are a family of polyanionic phosphate compounds with open frameworks, which have recently aroused great interest in rechargeable batteries [305–308]. Similar promising performance is also expected in capacitive applications, albeit seldomly reported. Recently, Song et al. have electrosynthesized a polyanionic molybdenophosphate film on a 3D exfoliated graphite substrate (EG) using a galvanostatic method [28]. The deposition electrolyte was 0.025 M ammonium molybdate mixed with 0.2 M phosphate buffer. The polyanion PO_4^{3-} in the electrolyte were incorporated into the mixed-valence Mo oxide lattice (containing Mo^{5+} and Mo^{6+}), replacing O atoms and forming Mo–O–P bonds (denoted as MoPO/EG). MoPO/EG was in situ electrochemically activated in 3 M KCl using cyclic voltammetry for $10,000$ cycles at a scan rate of 200 mV s^{-1} (denoted as A-MoPO/EG). This process allowed repeated K^+ intercalation and de-intercalation. A-MoPO/EG exhibited a film morphology with an average thickness of 100 nm (Fig. 32a). EDS indicated the even contributions of Mo, O, P, and K elements in A-MoPO/EG (Fig. 32b–e). The stable P signal after the activation indicated the electrochemical stability of Mo–O–P bonds. Inductively coupled plasma mass spectroscopy (ICP-OES) suggested the chemical formulae

of MoPO and A-MoPO were $\text{K}_{0.7}\text{Na}_{0.35}\text{Mo}_2\text{O}_{4.5}\text{PO}_4$ and $\text{K}_{1.55}\text{Mo}_2\text{O}_{4.2}\text{PO}_4$, respectively. Due to the incorporation of Mo^{4+} after the activation, the average valence state of Mo in MoPO/EG was reduced from $+5.38$ to $+4.84$ (Fig. 32f, g). Meanwhile, the content of O vacancy increased, as indicated by the enhanced intensity in the electron spin resonance (EPR) spectra (Fig. 32h). Additionally, all Na^+ in MoPO/EG was fully exchanged by K^+ and additional K^+ incorporated, both expanding the lattice spacing of molybdophosphate. Benefiting from the widened layers, as well as the enhanced electrical conductivity brought by the O vacancy, A-MoPO/EG showed better charge transfer kinetics than MoPO/EG (Fig. 32i). A-MoPO/EG exhibited quasi-rectangular CV curves, even at scan rates up to 200 mV s^{-1} (Fig. 32j). CV (Fig. 32k), XPS, and inductively coupled plasma mass spectroscopy (ICP-MS) indicated that cation (e.g., Li^+ , Na^+ , and K^+) intercalation was the primary charge storage mechanism of A-MoPO/EG. This polyanionic negative electrode exhibited a high specific capacitance of 556 F g^{-1} at 4.5 A g^{-1} , a low cutoff potential window limit of -1.5 V vs. SCE, as well as high electrochemical durability without capacitance decay after $100,000$ charge–discharge cycles (Fig. 32l). The authors speculated that the stable potential window of A-MoPO/EG down to -1.5 V vs. SCE could be due to the reversible K^+ -intercalation (around -1.4 V vs. SCE) near the water splitting potential, which suppressed hydrogen gas evolution [309].

Besides electrodeposition, electrochemical exfoliation is applicable to synthesize high-quality two-dimensional (2D) nanomaterials, e.g., MoS_2 , boron nitride, and MXene, from their corresponding bulk materials [310]. One example is 2D titanium carbide, $\text{Ti}_3\text{C}_2\text{T}_x$ ($\text{T} = \text{O}$ and OH), belonging to the MXene family [311]. Yang et al. applied a constant potential of 5 V for 5 h that delaminated bulk TiAlC_2 into $\text{Ti}_3\text{C}_2\text{T}_x$. The experimental setup was a two-electrode system with the first exfoliation step in an aqueous electrolyte composed of 1.0 M ammonium chloride (NH_4Cl) and 0.2 M tetramethylammonium hydroxide ($\text{TMA}\cdot\text{OH}$). The subsequent delamination in $25 \text{ wt } \%$ $\text{TMA}\cdot\text{OH}$ yielded single- or double-layer $\text{Ti}_3\text{C}_2\text{T}_x$ flakes with sizes up to $18.6 \text{ }\mu\text{m}$. During the electrochemical etching, Cl^- ions etched Al and broke the Ti–Al bonds. The intercalation of ammonium hydroxide subsequently opened the edges of the etched materials and triggered the etching. This fluoride-free electrochemical exfoliation process provided a safe and scalable way to synthesize MXenes. As a supercapacitor electrode, the $\text{Ti}_3\text{C}_2\text{T}_x$

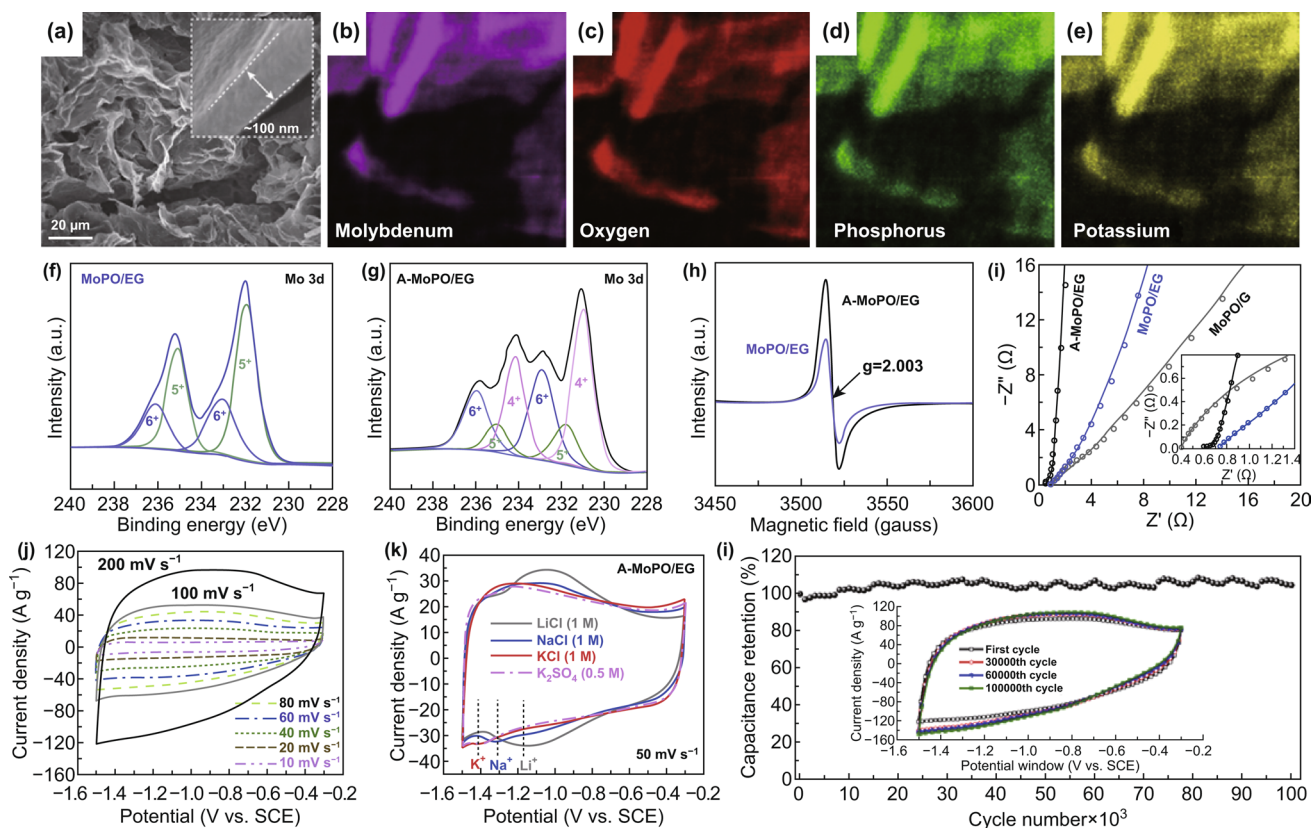


Fig. 32 **a** SEM image of activated polyanionic molybdenophosphate (A-MoPO/EG) on electrochemically exfoliated graphite foil. Inset: Magnified view showing the thickness of A-MoPO. **b–e** EDS elemental mappings of Mo, O, P, and K in A-MoPO/EG. **f, g** Mo 3d XPS spectra of **f** MoPO/EG and **g** A-MoPO/EG. **h** EPR spectra of oxygen deficiency signals of MoPO/EG and A-MoPO/EG. **i** Nyquist plots of A-MoPO/EG, MoPO/EG, and MoPO/non-exfoliated graphite foil electrodes. **j** CV curves of MoPO/EG at different scan rates in 3 M aqueous KCl electrolyte. **k** CV curves of MoPO/EG recorded in various aqueous electrolytes. **l** Cycling stability of A-MoPO/EG in 100,000 charge–discharge cycles. Adapted from Ref. [28] with permission

film exhibited an areal capacitance of 220 mF cm⁻² (volumetric capacitance 439 F cm⁻³) at 10 mV s⁻¹, comparable or even superior to those made from traditional wet chemical etching methods.

8 Summary and Outlook

Electrochemical methods constitute a family of facile, economic, and versatile synthesis technology for a plethora of nano-/microstructured materials as active materials in supercapacitors. It has its unique advantages, challenges, and opportunities as a synthesis tool (Fig. 33). In this review article, we have demonstrated that electrodeposition strategies can synthesize active materials consisting of zero-dimensional, one-dimensional, two-dimensional, and three-dimensional nano-/micromaterials, including particles, rods, tubes, wires, plates, sheets, and hierarchical structures.

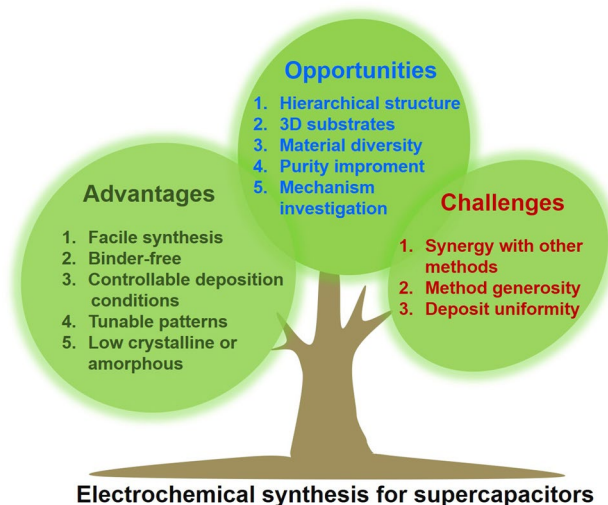


Fig. 33 Advantages, challenges, and future opportunities of electrochemical synthesis for supercapacitors

To sum up, we have listed below the advantages of electrochemical technologies in preparing nano-/microstructured materials for supercapacitors or, broadly speaking, electrochemical energy storage devices.

- (1) Their synthesis conditions are often mild (e.g., under room temperature) without elevated temperatures or ultrahigh pressures that might damage the structural integrity or alter the composition of the deposits and substrates. Additionally, electrochemical synthesis requires no advanced instruments and sophisticated operations, making it highly attainable and readily achievable.
 - (2) Electrodeposition directly and seamlessly incorporates active materials onto current collectors, a feature eliminating the need for polymer binders and conductive additives and easing electrode preparations.
 - (3) Electrodeposition offers facile tunability over the composition, crystal phase, and morphology of the deposited materials via changing depositing conditions, electrolyte compositions, current, voltage, and temperature.
 - (4) Electrodeposition is possible to direct the growth of active components onto user-designed patterns, as it only deposits materials in electrically conductive regions. This deposition selectivity makes electrodeposition particularly suitable to coat active materials on supercapacitors with delicate electrode architectures, such as micro-supercapacitors with interdigitated electrodes [196, 312, 313]. Additionally, the preferred deposition at ion-accessible locations ensures the high utilization efficiency of the active materials.
 - (5) Electrochemically synthesized materials are usually poorly crystalline or completely amorphous. The amorphous nature and abundant defects sometimes are beneficial for enhancing capacitance.
- (2) As discussed in Sect. 7, some active materials, e.g., metal sulfides, have not been extensively synthesized directly by electrodeposition. Converting metal oxides into the corresponding sulfides through sulfurization is one possible way. Still, this post-conversion usually involves high temperatures that might encounter problems with thermally unstable compounds or loss of structural water that are critical for charge transport [314].
 - (3) Controlling the uniformity of deposits remains a grand hurdle for electrodeposition, as edges of the deposition substrates are usually deposited first due to the strong local electrical field.

Projecting forward, we believe the following issues, if adequately addressed, could considerably enhance the electrochemical performance of electrodeposited materials and the practicality of electrodeposition.

Despite the above strengths, electrochemical techniques are facing many challenges and difficulties, including:

- (1) Post-treatments after electrodeposition, which are usually needed to improve the crystallinities of deposits, might alter the mechanical strength, functionality concentrations, crystal structures, or porous structure. For example, electrochemically exfoliated graphene sheets are usually stacks of 2–20 nm thick, instead of few- or single-layer graphene. Therefore, ultrasonication is needed to delaminate the exfoliated graphene into few-layer graphene sheets. This process, however, will inevitably break the resultant graphene sheets into pieces that will increase sheet-to-sheet contact resistance.
- (1) Rational design and realization of hierarchical structures with one-step electrodepositions is highly attractive to make high-performance supercapacitor electrodes with high mass loadings. Alternatively, combining electrodeposition strategies with other established materials synthesis methods (e.g., hydrothermal reactions to induce Ostwald ripening [197]) could also be explored to achieve hierarchical structures.
- (2) Developing substrates with mutually high surface areas and excellent electrical conductivity is preferred to improve the ion diffusion kinetics in supercapacitors, but one must be meticulous about the deposition time and rate to avoid pore clogging. In this respect, self-limiting electrodeposition to control the deposit thickness is necessary [315].
- (3) Diversifying the materials synthesized by electrodeposition. For example, metal sulfides have gained increasing attention as a new generation of electrochemical energy storage materials [316–318], but it is a pity that electrochemical methods can hardly synthesize them without post-treatments. Besides metal sulfides, electrodeposition can grow electrochemically active, 2D materials beyond graphene (e.g., layered metal oxides/hydroxides, boron nitride, and $g\text{-C}_3\text{N}_4$) [319], porous polymers and organic compounds, or pseudocapacitive materials compatible with non-aqueous electrolytes. The room for the development of electrochemical synthesis technologies is undoubtedly immense.
- (4) The purity of electrodeposited materials is often subpar to those made by vapor phase depositions. The multi-

valence could benefit charge storage, but might pose challenges for studies on charge storage mechanisms because differentiating outcomes resulting from collective behaviors of all the active components is non-trivial.

- (5) Deepening the understandings of the electrodeposition mechanism, including electrochemical nucleation and growth processes, will be highly rewarding to propel the development of electrochemical synthesis. For example, understanding the microscopic, complicated, and transient nucleation processes is imperative for controlling the morphology and uniformity of deposits. Mechanistic studies of electrodeposition, especially those developed recently, are limited. With the aid of in situ imaging technologies practiced in battery communities, the gain of insights into the early stages of electrodeposition will accumulate steadily.

Finally, we would like to stress that electrochemical synthesis technologies by no means can replace any existing materials synthesis methods. On the contrary, electrochemical strategies need to cooperate with other techniques to facilitate the explorations and development of high-performance electrodes in supercapacitors. Considering that electrodes play a central role in charge storage performances, we envision that the advancement and diversification of electrochemical synthesis technologies will directly push the development of electrochemical energy storage devices within and beyond electrochemical energy storage fields.

Acknowledgements Y.S. acknowledges the financial support from the National Natural Science Foundation of China (51804066) and the China Postdoctoral Science Foundation (2019T120214). X.-X.L. acknowledges the financial support from the National Natural Science Foundation of China (21673035).

Open Access This article is licensed under a Creative Commons Attribution 4.0 International License, which permits use, sharing, adaptation, distribution and reproduction in any medium or format, as long as you give appropriate credit to the original author(s) and the source, provide a link to the Creative Commons licence, and indicate if changes were made. The images or other third party material in this article are included in the article's Creative Commons licence, unless indicated otherwise in a credit line to the material. If material is not included in the article's Creative Commons licence and your intended use is not permitted by statutory regulation or exceeds the permitted use, you will need to obtain permission directly from the copyright holder. To view a copy of this licence, visit <http://creativecommons.org/licenses/by/4.0/>.

References

1. C. Choi, D.S. Ashby, D.M. Butts, R.H. DeBlock, Q. Wei, J. Lau, B. Dunn, Achieving high energy density and high power density with pseudocapacitive materials. *Nat. Rev. Mater.* **5**, 5–19 (2019). <https://doi.org/10.1038/s41578-019-0142-z>
2. J. Pu, Z. Shen, C. Zhong, Q. Zhou, J. Liu, J. Zhu, H. Zhang, Electrodeposition technologies for Li-based batteries: new frontiers of energy storage. *Adv. Mater.* (2019). <https://doi.org/10.1002/adma.201903808>
3. P. Simon, Y. Gogotsi, B. Dunn, Materials science. Where do batteries end and supercapacitors begin? *Science* **343**, 1210–1211 (2014). <https://doi.org/10.1126/science.1249625>
4. T. Liu, F. Zhang, Y. Song, Y. Li, Revitalizing carbon supercapacitor electrodes with hierarchical porous structures. *J. Mater. Chem. A* **5**, 17705–17733 (2017). <https://doi.org/10.1039/c7ta05646j>
5. B.E. Conway, *Electrochemical Supercapacitors: Scientific Fundamentals and Technological Applications* (Springer, New York, 2013), pp. 11–31
6. Y. Jiang, J. Liu, Definitions of pseudocapacitive materials: a brief review. *Energy Environ. Mater.* **2**, 30–37 (2019). <https://doi.org/10.1002/eem2.12028>
7. J. Miller, Introduction to electrochemical capacitor technology. *IEEE Electr. Insul. Mag.* **26**, 40–47 (2010). <https://doi.org/10.1109/mei.2010.5511188>
8. Y. Huang, Z. Tang, Z. Liu, J. Wei, H. Hu, C. Zhi, Toward enhancing wearability and fashion of wearable supercapacitor with modified polyurethane artificial leather electrolyte. *Nano-Micro Lett.* **10**, 38 (2018). <https://doi.org/10.1007/s40820-018-0191-7>
9. Z. Bo, C. Li, H. Yang, K. Ostrikov, J. Yan, K. Cen, Design of supercapacitor electrodes using molecular dynamics simulations. *Nano-Micro Lett.* **10**, 33 (2018). <https://doi.org/10.1007/s40820-018-0188-2>
10. Y. Liu, B. Soucaze-Guillous, P.-L. Taberna, P. Simon, Understanding of carbon-based supercapacitors ageing mechanisms by electrochemical and analytical methods. *J. Power Sources* **366**, 123–130 (2017). <https://doi.org/10.1016/j.jpowsour.2017.08.104>
11. J.R. Miller, P. Simon, Materials science. Electrochemical capacitors for energy management. *Science* **321**, 651–652 (2008). <https://doi.org/10.1126/science.1158736>
12. P. Simon, Y. Gogotsi, Materials for electrochemical capacitors. *Nat. Mater.* **7**, 845–854 (2008). <https://doi.org/10.1038/nmat2297>
13. V. Augustyn, P. Simon, B. Dunn, Pseudocapacitive oxide materials for high-rate electrochemical energy storage. *Energy Environ. Sci.* **7**, 1597–1614 (2014). <https://doi.org/10.1039/c3ee44164d>
14. N. Jabeen, A. Hussain, Q. Xia, S. Sun, J. Zhu, H. Xia, High-performance 2.6 V aqueous asymmetric supercapacitors based on in situ formed Na_{0.5}MnO₂ nanosheet assembled nanowall arrays. *Adv. Mater.* **29**, 1700804 (2017). <https://doi.org/10.1002/adma.201700804>



15. W. Wei, X. Cui, W. Chen, D.G. Ivey, Manganese oxide-based materials as electrochemical supercapacitor electrodes. *Chem. Soc. Rev.* **40**, 1697–1721 (2011). <https://doi.org/10.1039/c0cs00127a>
16. Y. Wu, Y. Yang, X. Zhao, Y. Tan, Y. Liu, Z. Wang, F. Ran, A novel hierarchical porous 3D structured vanadium nitride/carbon membranes for high-performance supercapacitor negative electrodes. *Nano-Micro Lett.* **10**, 63 (2018). <https://doi.org/10.1007/s40820-018-0217-1>
17. L.L. Zhang, X.S. Zhao, Carbon-based materials as supercapacitor electrodes. *Chem. Soc. Rev.* **38**, 2520–2531 (2009). <https://doi.org/10.1039/b813846j>
18. D. Landolt, Electrodeposition science and technology in the last quarter of the twentieth century. *J. Electrochem. Soc.* **149**, S9 (2002). <https://doi.org/10.1149/1.1469028>
19. I.M. Dharmadasa, J. Haigh, Strengths and advantages of electrodeposition as a semiconductor growth technique for applications in macroelectronic devices. *J. Electrochem. Soc.* **153**, G47–G52 (2006). <https://doi.org/10.1149/1.2128120>
20. M.F. Montemor, S. Eugénio, N. Tuyen, R.P. Silva, T.M. Silva, M.J. Carmezim, *Nanostructured Transition Metal Oxides Produced by Electrodeposition for Application as Redox Electrodes for Supercapacitors* (Springer, Berlin, 2016), pp. 681–714. https://doi.org/10.1007/978-3-319-15266-0_14
21. J. Wang, K.K. Manga, Q. Bao, K.P. Loh, High-yield synthesis of few-layer graphene flakes through electrochemical expansion of graphite in propylene carbonate electrolyte. *J. Am. Chem. Soc.* **133**, 8888–8891 (2011). <https://doi.org/10.1021/ja203725d>
22. W. Chen, R.B. Rakhi, L. Hu, X. Xie, Y. Cui, H.N. Alsharief, High-performance nanostructured supercapacitors on a sponge. *Nano Lett.* **11**, 5165–5172 (2011). <https://doi.org/10.1021/nl2023433>
23. X. Lang, A. Hirata, T. Fujita, M. Chen, Nanoporous metal/oxide hybrid electrodes for electrochemical supercapacitors. *Nat. Nanotechnol.* **6**, 232–236 (2011). <https://doi.org/10.1038/nnano.2011.13>
24. T. Liu, Y. Ling, Y. Yang, L. Finn, E. Collazo, T. Zhai, Y. Tong, Y. Li, Investigation of hematite nanorod–nanoflake morphological transformation and the application of ultrathin nanoflakes for electrochemical devices. *Nano Energy* **12**, 169–177 (2015). <https://doi.org/10.1016/j.nanoen.2014.12.023>
25. T. Liu, L. Finn, M. Yu, H. Wang, T. Zhai, X. Lu, Y. Tong, Y. Li, Polyaniline and polypyrrole pseudocapacitor electrodes with excellent cycling stability. *Nano Lett.* **14**, 2522–2527 (2014). <https://doi.org/10.1021/nl500255v>
26. Y. Song, T.-Y. Liu, X.-X. Xu, D.-Y. Feng, Y. Li, X.-X. Liu, Pushing the cycling stability limit of polypyrrole for supercapacitors. *Adv. Funct. Mater.* **25**, 4626–4632 (2015). <https://doi.org/10.1002/adfm.201501709>
27. M.-H. Bai, T.-Y. Liu, F. Luan, Y. Li, X.-X. Liu, Electrodeposition of vanadium oxide–polyaniline composite nanowire electrodes for high energy density supercapacitors. *J. Mater. Chem. A* **2**, 10882–10888 (2014). <https://doi.org/10.1039/c3ta15391f>
28. Y. Song, P. Deng, Z. Qin, D. Feng, D. Guo, X. Sun, X.-X. Liu, A polyanionic molybdenophosphate anode for a 2.7 V aqueous pseudocapacitor. *Nano Energy* **65**, 104010 (2019). <https://doi.org/10.1016/j.nanoen.2019.104010>
29. F. Liu, Z. Chen, G. Fang, Z. Wang, Y. Cai, B. Tang, J. Zhou, V₂O₅ nanospheres with mixed vanadium valences as high electrochemically active aqueous zinc-ion battery cathode. *Nano-Micro Lett.* **11**, 25 (2019). <https://doi.org/10.1007/s40820-019-0256-2>
30. R.G. Kelly, J.R. Scully, D. Shoesmith, R.G. Buchheit, *Electrochemical Techniques in Corrosion Science and Engineering*. CRC Press, Boca Raton. (2002). <https://doi.org/10.1201/9780203909133>
31. A.J. Bard, L.R. Faulkner, J. Leddy, C.G. Zoski, *Electrochemical Methods: Fundamentals and Applications* (Wiley, New York, 1980)
32. N. Elgrishi, K.J. Rountree, B.D. McCarthy, E.S. Rountree, T.T. Eisenhart, J.L. Dempsey, A practical beginner’s guide to cyclic voltammetry. *J. Chem. Educ.* **95**, 197–206 (2017). <https://doi.org/10.1021/acs.jchemed.7b00361>
33. D.K. Gosser, *Cyclic Voltammetry: Simulation and Analysis of Reaction Mechanisms* (VCH, New York, 1993)
34. R. Dong, Y. Song, D. Yang, H.-Y. Shi, Z. Qin et al., Electrochemical in situ construction of vanadium oxide heterostructures with boosted pseudocapacitive charge storage. *J. Mater. Chem. A* **8**, 1176–1183 (2020). <https://doi.org/10.1039/c9ta12097a>
35. Z. Sun, X. Cai, D.-Y. Feng, Z.-H. Huang, Y. Song, X.-X. Liu, Hybrid iron oxide on three-dimensional exfoliated graphite electrode with ultrahigh capacitance for energy storage applications. *ChemElectroChem* **5**, 1501–1508 (2018). <https://doi.org/10.1002/celec.201800143>
36. Z. Sun, X. Cai, Y. Song, X.-X. Liu, Electrochemical deposition of honeycomb magnetite on partially exfoliated graphite as anode for capacitive applications. *J. Power Sources* **359**, 57–63 (2017). <https://doi.org/10.1016/j.jpowsour.2017.05.055>
37. Y. Song, T.Y. Liu, B. Yao, T.Y. Kou, D.Y. Feng, X.X. Liu, Y. Li, Amorphous mixed-valence vanadium oxide/exfoliated carbon cloth structure shows a record high cycling stability. *Small* **13**, 1700067 (2017). <https://doi.org/10.1002/sml.201700067>
38. X. Cai, Y. Song, S.-Q. Wang, X. Sun, X.-X. Liu, Extending the cycle life of high mass loading MoO_x electrode for supercapacitor applications. *Electrochim. Acta* **325**, 134877 (2019). <https://doi.org/10.1016/j.electacta.2019.134877>
39. M. Paunovic, *Electrochemical Deposition*. Encyclopedia of Electrochemistry: Online (2007). <https://doi.org/10.1002/9783527610426.bard050003>
40. D. Lincot, Electrodeposition of semiconductors. *Thin Solid Films* **487**, 40–48 (2005). <https://doi.org/10.1016/j.tsf.2005.01.032>
41. M. Paunovic, M. Schlesinger, *Fundamentals of Electrochemical Deposition* (Wiley, New York, 1998)
42. D.M. Kolb, M. Przasnyski, H. Gerischer, Underpotential deposition of metals and work function differences. *J.*

- Electroanal. Chem. **54**, 25–38 (1974). [https://doi.org/10.1016/s0022-0728\(74\)80377-3](https://doi.org/10.1016/s0022-0728(74)80377-3)
43. E. Herrero, L.J. Buller, H.D. Abruna, Underpotential deposition at single crystal surfaces of Au, Pt, Ag and other materials. *Chem. Rev.* **101**, 1897–1930 (2001). <https://doi.org/10.1021/cr9600363>
44. Z. Shi, S. Wu, J. Lipkowski, Investigations of Cl^- adsorption at the Au(111) electrode in the presence of underpotentially deposited copper atoms. *J. Electroanal. Chem.* **384**, 171–177 (1995). [https://doi.org/10.1016/0022-0728\(94\)03747-q](https://doi.org/10.1016/0022-0728(94)03747-q)
45. J.C. Ballesteros, E. Chañet, P. Ozil, G. Trejo, Y. Meas, Electrochemical studies of Zn underpotential/overpotential deposition on a nickel electrode from non-cyanide alkaline solution containing glycine. *Electrochim. Acta* **56**, 5443–5451 (2011). <https://doi.org/10.1016/j.electacta.2011.02.106>
46. M. Palomar-Pardavé, I. González, N. Batina, New insights into evaluation of kinetic parameters for potentiostatic metal deposition with underpotential and overpotential deposition processes. *J. Phys. Chem. B* **104**, 3545–3555 (2000). <https://doi.org/10.1021/jp9931861>
47. R.E. Rettew, J.W. Guthrie, F.M. Alamgir, Layer-by-layer Pt growth on polycrystalline Au: surface-limited redox replacement of overpotentially deposited Ni monolayers. *J. Electrochem. Soc.* **156**, D513–D516 (2009). <https://doi.org/10.1149/1.3224113>
48. M.G. Pavlović, L.J. Pavlović, N.D. Nikolić, K.I. Popov, The effect of some parameters of electrolysis on apparent density of electrolytic copper powder in galvanostatic deposition. *Mater. Sci. Forum* **352**, 65–72 (2000). <https://doi.org/10.4028/www.scientific.net/MSF.352.65>
49. R. Salazar, C. Lévy-Clément, V. Ivanova, Galvanostatic deposition of ZnO thin films. *Electrochim. Acta* **78**, 547–556 (2012). <https://doi.org/10.1016/j.electacta.2012.06.070>
50. Z.H. Huang, Y. Song, D.Y. Feng, Z. Sun, X. Sun, X.X. Liu, High mass loading MnO_2 with hierarchical nanostructures for supercapacitors. *ACS Nano* **12**, 3557–3567 (2018). <https://doi.org/10.1021/acsnano.8b00621>
51. E.J. Podlaha, Selective electrodeposition of nanoparticulates into metal matrices. *Nano Lett.* **1**, 413–416 (2001). <https://doi.org/10.1021/nl015508u>
52. G. Zhu, C. Pan, W. Guo, C.Y. Chen, Y. Zhou, R. Yu, Z.L. Wang, Triboelectric-generator-driven pulse electrodeposition for micropatterning. *Nano Lett.* **12**, 4960–4965 (2012). <https://doi.org/10.1021/nl302560k>
53. Y. Su, I. Zhitomirsky, Pulse electrosynthesis of MnO_2 electrodes for supercapacitors. *Adv. Eng. Mater.* **16**, 760–766 (2014). <https://doi.org/10.1002/adem.201400077>
54. M. Ghaemi, Effects of direct and pulse current on electrodeposition of manganese dioxide. *J. Power Sources* **111**, 248–254 (2002). [https://doi.org/10.1016/s0378-7753\(02\)00309-9](https://doi.org/10.1016/s0378-7753(02)00309-9)
55. H. Cheh, Electrodeposition of gold by pulsed current. *J. Electrochem. Soc.* **118**, 551 (1971). <https://doi.org/10.1149/1.2408110>
56. H.M.M.N. Hennayaka, H.S. Lee, Structural and optical properties of ZnS thin film grown by pulsed electrodeposition. *Thin Solid Films* **548**, 86–90 (2013). <https://doi.org/10.1016/j.tsf.2013.09.011>
57. A. Davies, P. Audette, B. Farrow, F. Hassan, Z. Chen, J.-Y. Choi, A. Yu, Graphene-based flexible supercapacitors: pulse-electropolymerization of polypyrrole on free-standing graphene films. *J. Phys. Chem. C* **115**, 17612–17620 (2011). <https://doi.org/10.1021/jp205568v>
58. L. Besra, M. Liu, A review on fundamentals and applications of electrophoretic deposition (EPD). *Prog. Mater. Sci.* **52**, 1–61 (2007). <https://doi.org/10.1016/j.pmatsci.2006.07.001>
59. P. Sarkar, P.S. Nicholson, Electrophoretic deposition (EPD): mechanisms, kinetics, and application to ceramics. *J. Am. Ceram. Soc.* **79**, 1987–2002 (1996). <https://doi.org/10.1111/j.1151-2916.1996.tb08929.x>
60. C. Du, N. Pan, Supercapacitors using carbon nanotubes films by electrophoretic deposition. *J. Power Sources* **160**, 1487–1494 (2006). <https://doi.org/10.1016/j.jpowsour.2006.02.092>
61. C. Du, N. Pan, High power density supercapacitor electrodes of carbon nanotube films by electrophoretic deposition. *Nanotechnology* **17**, 5314–5318 (2006). <https://doi.org/10.1088/0957-4484/17/21/005>
62. D. Pech, M. Brunet, H. Durou, P. Huang, V. Mochalin, Y. Gogotsi, P.L. Taberna, P. Simon, Ultrahigh-power micrometre-sized supercapacitors based on onion-like carbon. *Nat. Nanotechnol.* **5**, 651–654 (2010). <https://doi.org/10.1038/nnano.2010.162>
63. Y. Su, I. Zhitomirsky, Electrophoretic nanotechnology of composite electrodes for electrochemical supercapacitors. *J. Phys. Chem. B* **117**, 1563–1570 (2013). <https://doi.org/10.1021/jp304358q>
64. Y. Wang, I. Zhitomirsky, Electrophoretic deposition of manganese dioxide-multiwalled carbon nanotube composites for electrochemical supercapacitors. *Langmuir* **25**, 9684–9689 (2009). <https://doi.org/10.1021/la900937e>
65. H. Zhang, X. Zhang, D. Zhang, X. Sun, H. Lin, C. Wang, Y. Ma, One-step electrophoretic deposition of reduced graphene oxide and $\text{Ni}(\text{OH})_2$ composite films for controlled syntheses supercapacitor electrodes. *J. Phys. Chem. B* **117**, 1616–1627 (2013). <https://doi.org/10.1021/jp305198j>
66. Z.Y. Xia, S. Pezzini, E. Treossi, G. Giambastiani, F. Corticelli et al., The exfoliation of graphene in liquids by electrochemical, chemical, and sonication-assisted techniques: a nanoscale study. *Adv. Funct. Mater.* **23**, 4684–4693 (2013). <https://doi.org/10.1002/adfm.201203686>
67. A.M. Abdelkader, I.A. Kinloch, R.A. Dryfe, Continuous electrochemical exfoliation of micrometer-sized graphene using synergistic ion intercalations and organic solvents. *ACS Appl. Mater. Interfaces*. **6**, 1632–1639 (2014). <https://doi.org/10.1021/am404497n>
68. A.M. Abdelkader, A.J. Cooper, R.A. Dryfe, I.A. Kinloch, How to get between the sheets: a review of recent works on the electrochemical exfoliation of graphene materials from bulk graphite. *Nanoscale* **7**, 6944–6956 (2015). <https://doi.org/10.1039/c4nr06942k>



69. A. Ambrosi, M. Pumera, Exfoliation of layered materials using electrochemistry. *Chem. Soc. Rev.* **47**, 7213–7224 (2018). <https://doi.org/10.1039/c7cs00811b>
70. R. Kumar, S. Sahoo, E. Joanni, R.K. Singh, W.K. Tan, K.K. Kar, A. Matsuda, Recent progress in the synthesis of graphene and derived materials for next generation electrodes of high performance lithium ion batteries. *Prog. Energy Combust.* **75**, 100786 (2019). <https://doi.org/10.1016/j.pecs.2019.100786>
71. A. Ambrosi, M. Pumera, Electrochemically exfoliated graphene and graphene oxide for energy storage and electrochemistry applications. *Chemistry* **22**, 153–159 (2016). <https://doi.org/10.1002/chem.201503110>
72. P. Yu, S.E. Lowe, G.P. Simon, Y.L. Zhong, Electrochemical exfoliation of graphite and production of functional graphene. *Curr. Opin. Colloid Interface Sci.* **20**, 329–338 (2015). <https://doi.org/10.1016/j.cocis.2015.10.007>
73. S. Yang, M.R. Lohe, K. Mullen, X. Feng, New-generation graphene from electrochemical approaches: production and applications. *Adv. Mater.* **28**, 6213–6221 (2016). <https://doi.org/10.1002/adma.201505326>
74. W. Wei, G. Wang, S. Yang, X. Feng, K. Mullen, Efficient coupling of nanoparticles to electrochemically exfoliated graphene. *J. Am. Chem. Soc.* **137**, 5576–5581 (2015). <https://doi.org/10.1021/jacs.5b02284>
75. L. Wu, W. Li, P. Li, S. Liao, S. Qiu et al., Powder, paper and foam of few-layer graphene prepared in high yield by electrochemical intercalation exfoliation of expanded graphite. *Small* **10**, 1421–1429 (2014). <https://doi.org/10.1002/sml.201302730>
76. A. Ejigu, K. Fujisawa, B.F. Spencer, B. Wang, M. Terrones, I.A. Kinloch, R.A.W. Dryfe, On the role of transition metal salts during electrochemical exfoliation of graphite: antioxidants or metal oxide decorators for energy storage applications. *Adv. Funct. Mater.* **28**, 1804357 (2018). <https://doi.org/10.1002/adfm.201804357>
77. K.S. Rao, J. Sentilnathan, H.-W. Cho, J.-J. Wu, M. Yoshimura, Soft processing of graphene nanosheets by glycine-bisulfate ionic-complex-assisted electrochemical exfoliation of graphite for reduction catalysis. *Adv. Funct. Mater.* **25**, 298–305 (2015). <https://doi.org/10.1002/adfm.201402621>
78. C.Y. Su, A.Y. Lu, Y. Xu, F.R. Chen, A.N. Khlobystov, L.J. Li, High-quality thin graphene films from fast electrochemical exfoliation. *ACS Nano* **5**, 2332–2339 (2011). <https://doi.org/10.1021/nn200025p>
79. J. Lu, J.X. Yang, J. Wang, A. Lim, S. Wang, K.P. Loh, One-pot synthesis of fluorescent carbon nanoribbons, nanoparticles, and graphene by the exfoliation of graphite in ionic liquids. *ACS Nano* **3**, 2367–2375 (2009). <https://doi.org/10.1021/nn900546b>
80. W. Cai, X. Feng, W. Hu, Y. Pan, Y. Hu, X. Gong, Functionalized graphene from electrochemical exfoliation for thermoplastic polyurethane: thermal stability, mechanical properties, and flame retardancy. *Ind. Eng. Chem. Res.* **55**, 10681–10689 (2016). <https://doi.org/10.1021/acs.iecr.6b02579>
81. M. Mao, M. Wang, J. Hu, G. Lei, S. Chen, H. Liu, Simultaneous electrochemical synthesis of few-layer graphene flakes on both electrodes in protic ionic liquids. *Chem. Commun.* **49**, 5301–5303 (2013). <https://doi.org/10.1039/c3cc41909f>
82. H. Huang, Y. Xia, X. Tao, J. Du, J. Fang, Y. Gan, W. Zhang, Highly efficient electrolytic exfoliation of graphite into graphene sheets based on Li ions intercalation–expansion–microexplosion mechanism. *J. Mater. Chem.* **22**, 10452–10456 (2012). <https://doi.org/10.1039/c2jm00092j>
83. Y. Yang, F. Lu, Z. Zhou, W. Song, Q. Chen, X. Ji, Electrochemically cathodic exfoliation of graphene sheets in room temperature ionic liquids N-butyl, methylpyrrolidinium bis(trifluoromethylsulfonyl)imide and their electrochemical properties. *Electrochim. Acta* **113**, 9–16 (2013). <https://doi.org/10.1016/j.electacta.2013.09.031>
84. K. Parvez, R. Li, S.R. Puniredd, Y. Hernandez, F. Hinkel, S. Wang, X. Feng, K. Mullen, Electrochemically exfoliated graphene as solution-processable, highly conductive electrodes for organic electronics. *ACS Nano* **7**, 3598–3606 (2013). <https://doi.org/10.1021/nn400576v>
85. W. Wang, W. Liu, Y. Zeng, Y. Han, M. Yu, X. Lu, Y. Tong, A novel exfoliation strategy to significantly boost the energy storage capability of commercial carbon cloth. *Adv. Mater.* **27**, 3572–3578 (2015). <https://doi.org/10.1002/adma.201507070>
86. Y. Song, S. Duan, D. Yang, R. Dong, D. Guo, X. Sun, X.-X. Liu, 3D exfoliated carbon paper toward highly loaded aqueous energy storage applications. *Energy Technol.* **7**, 1900892 (2019). <https://doi.org/10.1002/ente.201900892>
87. F. Zeng, Z. Sun, X. Sang, D. Diamond, K.T. Lau, X. Liu, D.S. Su, In situ one-step electrochemical preparation of graphene oxide nanosheet-modified electrodes for biosensors. *Chemosuschem* **4**, 1587–1591 (2011). <https://doi.org/10.1002/cssc.201100319>
88. Y. Song, D.Y. Feng, T.Y. Liu, Y. Li, X.X. Liu, Controlled partial-exfoliation of graphite foil and integration with MnO₂ nanosheets for electrochemical capacitors. *Nanoscale* **7**, 3581–3587 (2015). <https://doi.org/10.1039/c4nr06559j>
89. K. Parvez, Z.S. Wu, R. Li, X. Liu, R. Graf, X. Feng, K. Mullen, Exfoliation of graphite into graphene in aqueous solutions of inorganic salts. *J. Am. Chem. Soc.* **136**, 6083–6091 (2014). <https://doi.org/10.1021/ja5017156>
90. M. Alanyahoğlu, J.J. Segura, J. Oró-Solè, N. Casañ-Pastor, The synthesis of graphene sheets with controlled thickness and order using surfactant-assisted electrochemical processes. *Carbon* **50**, 142–152 (2012). <https://doi.org/10.1016/j.carbon.2011.07.064>
91. C.-H. Chen, S.-W. Yang, M.-C. Chuang, W.-Y. Woon, C.-Y. Su, Towards the continuous production of high crystallinity graphene via electrochemical exfoliation with molecular in situ encapsulation. *Nanoscale* **7**, 15362–15373 (2015). <https://doi.org/10.1039/c5nr03669k>
92. K. Chen, D. Xue, Preparation of colloidal graphene in quantity by electrochemical exfoliation. *J. Colloid Interface Sci.* **436**, 41–46 (2014). <https://doi.org/10.1016/j.jcis.2014.08.057>

93. A.J. Cooper, N.R. Wilson, I.A. Kinloch, R.A.W. Dryfe, Single stage electrochemical exfoliation method for the production of few-layer graphene via intercalation of tetraalkylammonium cations. *Carbon* **66**, 340–350 (2014). <https://doi.org/10.1016/j.carbon.2013.09.009>
94. A. Ejigu, I.A. Kinloch, R.A. Dryfe, Single stage simultaneous electrochemical exfoliation and functionalization of graphene. *ACS Appl. Mater. Interfaces* **9**, 710–721 (2017). <https://doi.org/10.1021/acsami.6b12868>
95. S. Yang, S. Bruller, Z.S. Wu, Z. Liu, K. Parvez et al., Organic radical-assisted electrochemical exfoliation for the scalable production of high-quality graphene. *J. Am. Chem. Soc.* **137**, 13927–13932 (2015). <https://doi.org/10.1021/jacs.5b09000>
96. X. Cai, Y. Song, Z. Sun, D. Guo, X.-X. Liu, Rate capability improvement of Co–Ni double hydroxides integrated in cathodically partially exfoliated graphite. *J. Power Sources* **365**, 126–133 (2017). <https://doi.org/10.1016/j.jpowsour.2017.08.039>
97. D.-Y. Feng, Y. Song, Z.-H. Huang, X.-X. Xu, X.-X. Liu, Rate capability improvement of polypyrrole via integration with functionalized commercial carbon cloth for pseudocapacitor. *J. Power Sources* **324**, 788–797 (2016). <https://doi.org/10.1016/j.jpowsour.2016.05.112>
98. L. Hu, X. Peng, Y. Li, L. Wang, K. Huo, L.Y.S. Lee, K.Y. Wong, P.K. Chu, Direct anodic exfoliation of graphite onto high-density aligned graphene for large capacity supercapacitors. *Nano Energy* **34**, 515–523 (2017). <https://doi.org/10.1016/j.nanoen.2017.03.007>
99. T. Liu, C. Zhu, T. Kou, M.A. Worsley, F. Qian, C. Condes, E.B. Duoss, C.M. Spadaccini, Y. Li, Ion intercalation induced capacitance improvement for graphene-based supercapacitor electrodes. *ChemNanoMat* **2**, 635–641 (2016). <https://doi.org/10.1002/cnma.201600107>
100. Y. Song, T. Liu, F. Qian, C. Zhu, B. Yao, E. Duoss, C. Spadaccini, M. Worsley, Y. Li, Three-dimensional carbon architectures for electrochemical capacitors. *J. Colloid Interface Sci.* **509**, 529–545 (2018). <https://doi.org/10.1016/j.jcis.2017.07.081>
101. Y. Song, T.-Y. Liu, G.-L. Xu, D.-Y. Feng, B. Yao, T.-Y. Kou, X.-X. Liu, Y. Li, Tri-layered graphite foil for electrochemical capacitors. *J. Mater. Chem. A* **4**, 7683–7688 (2016). <https://doi.org/10.1039/c6ta02075e>
102. Y. Zou, S. Wang, Interconnecting carbon fibers with the in situ electrochemically exfoliated graphene as advanced binder-free electrode materials for flexible supercapacitor. *Sci. Rep.* **5**, 11792 (2015). <https://doi.org/10.1038/srep11792>
103. S.-H. Lee, S.-D. Seo, Y.-H. Jin, H.-W. Shim, D.-W. Kim, A graphite foil electrode covered with electrochemically exfoliated graphene nanosheets. *Electrochem. Commun.* **12**, 1419–1422 (2010). <https://doi.org/10.1016/j.elecom.2010.07.036>
104. R.M. Tamgadge, A. Shukla, A PH-dependent partial electrochemical exfoliation of highly oriented pyrolytic graphite for high areal capacitance electric double layer capacitor electrode. *Electrochim. Acta* **325**, 134933 (2019). <https://doi.org/10.1016/j.electacta.2019.134933>
105. Y. Song, J.-L. Xu, X.-X. Liu, Electrochemical anchoring of dual doping polypyrrole on graphene sheets partially exfoliated from graphite foil for high-performance supercapacitor electrode. *J. Power Sources* **249**, 48–58 (2014). <https://doi.org/10.1016/j.jpowsour.2013.10.102>
106. Y. Song, X. Cai, X. Xu, X.-X. Liu, Integration of nickel-cobalt double hydroxide nanosheets and polypyrrole films with functionalized partially exfoliated graphite for asymmetric supercapacitors with improved rate capability. *J. Mater. Chem. A* **3**, 14712–14720 (2015). <https://doi.org/10.1039/c5ta02810h>
107. Z. Liu, Z.S. Wu, S. Yang, R. Dong, X. Feng, K. Mullen, Ultraflexible in-plane micro-supercapacitors by direct printing of solution-processable electrochemically exfoliated graphene. *Adv. Mater.* **28**, 2217–2222 (2016). <https://doi.org/10.1002/adma.201505304>
108. J.M. Munuera, J.I. Paredes, M. Enterría, A. Pagan, S. Villar-Rodil, M.F.R. Pereira et al., Electrochemical exfoliation of graphite in aqueous sodium halide electrolytes toward low oxygen content graphene for energy and environmental applications. *ACS Appl. Mater. Interfaces* **9**, 24085–24099 (2017). <https://doi.org/10.1021/acsami.7b04802>
109. N. Parveen, M.O. Ansari, S.A. Ansari, M.H. Cho, Simultaneous sulfur doping and exfoliation of graphene from graphite using an electrochemical method for supercapacitor electrode materials. *J. Mater. Chem. A* **4**, 233–240 (2016). <https://doi.org/10.1039/c5ta07963b>
110. J. Liu, M. Notarianni, G. Will, V.T. Tiong, H. Wang, N. Motta, Electrochemically exfoliated graphene for electrode films: effect of graphene flake thickness on the sheet resistance and capacitive properties. *Langmuir* **29**, 13307–13314 (2013). <https://doi.org/10.1021/la403159n>
111. S.M. Jung, D.L. Mafra, C.T. Lin, H.Y. Jung, J. Kong, Controlled porous structures of graphene aerogels and their effect on supercapacitor performance. *Nanoscale* **7**, 4386–4393 (2015). <https://doi.org/10.1039/c4nr07564a>
112. X. Xiao, Y. Zeng, H. Feng, K. Xu, G. Zhong et al., Three-dimensional nitrogen-doped graphene frameworks from electrochemical exfoliation of graphite as efficient supercapacitor electrodes. *ChemNanoMat* **5**, 152–157 (2019). <https://doi.org/10.1002/cnma.201800452>
113. P. Khanra, T. Kuila, S.H. Bae, N.H. Kim, J.H. Lee, Electrochemically exfoliated graphene using 9-anthracene carboxylic acid for supercapacitor application. *J. Mater. Chem.* **22**, 24403–24410 (2012). <https://doi.org/10.1039/c2jm34838a>
114. S. Liu, J. Ou, J. Wang, X. Liu, S. Yang, A simple two-step electrochemical synthesis of graphene sheets film on the ITO electrode as supercapacitors. *J. Appl. Electrochem.* **41**, 881–884 (2011). <https://doi.org/10.1007/s10800-011-0304-1>
115. V. Thirumal, A. Pandurangan, R. Jayavel, K.S. Venkatesh, N.S. Palani, R. Ragavan, R. Ilangovan, Single pot electrochemical synthesis of functionalized and phosphorus doped graphene nanosheets for supercapacitor applications. *J. Mater. Sci.: Mater. Electron.* **26**, 6319–6328 (2015). <https://doi.org/10.1007/s10854-015-3219-5>



116. C. Li, H. Bai, G. Shi, Conducting polymer nanomaterials: electrosynthesis and applications. *Chem. Soc. Rev.* **38**, 2397–2409 (2009). <https://doi.org/10.1039/b816681c>
117. G.A. Snook, P. Kao, A.S. Best, Conducting-polymer-based supercapacitor devices and electrodes. *J. Power Sources* **196**, 1–12 (2011). <https://doi.org/10.1016/j.jpowsour.2010.06.084>
118. R. Gangopadhyay, A. De, Conducting polymer nanocomposites: a brief overview. *Chem. Mater.* **12**, 608–622 (2000). <https://doi.org/10.1021/cm990537f>
119. Z. Cai, L. Li, J. Ren, L. Qiu, H. Lin, H. Peng, Flexible, weavable and efficient microsupercapacitor wires based on polyaniline composite fibers incorporated with aligned carbon nanotubes. *J. Mater. Chem. A* **1**, 258–261 (2013). <https://doi.org/10.1039/c2ta00274d>
120. K.M. Kim, Y.-G. Lee, D.O. Shin, J.M. Ko, Supercapacitive properties of layered electrodes composed of electrodeposited RuO₂ and polyaniline. *Electrochim. Acta* **196**, 309–315 (2016). <https://doi.org/10.1016/j.electacta.2016.02.194>
121. H. Li, J. Song, L. Wang, X. Feng, R. Liu, W. Zeng, Z. Huang, Y. Ma, L. Wang, Flexible all-solid-state supercapacitors based on polyaniline orderly nanotubes array. *Nanoscale* **9**, 193–200 (2017). <https://doi.org/10.1039/c6nr07921k>
122. C. Tran, R. Singhal, D. Lawrence, V. Kalra, Polyaniline-coated freestanding porous carbon nanofibers as efficient hybrid electrodes for supercapacitors. *J. Power Sources* **293**, 373–379 (2015). <https://doi.org/10.1016/j.jpowsour.2015.05.054>
123. Y. Xie, D. Wang, J. Ji, Preparation and supercapacitor performance of freestanding polypyrrole/polyaniline coaxial nanoarrays. *Energy Technol.* **4**, 714–721 (2016). <https://doi.org/10.1002/ente.201500460>
124. C. Fu, H. Zhou, R. Liu, Z. Huang, J. Chen, Y. Kuang, Supercapacitor based on electropolymerized polythiophene and multi-walled carbon nanotubes composites. *Mater. Chem. Phys.* **132**, 596–600 (2012). <https://doi.org/10.1016/j.matchemphys.2011.11.074>
125. A. Laforgue, P. Simon, C. Sarrazin, J.-F. Fauvarque, Polythiophene-based supercapacitors. *J. Power Sources* **80**, 142–148 (1999). [https://doi.org/10.1016/s0378-7753\(98\)00258-4](https://doi.org/10.1016/s0378-7753(98)00258-4)
126. F.N. Ajjan, N. Casado, T. Rębiś, A. Elfwing, N. Solin, D. Mecerreyes, O. Inganäs, High performance PEDOT/lignin biopolymer composites for electrochemical supercapacitors. *J. Mater. Chem. A* **4**, 1838–1847 (2016). <https://doi.org/10.1039/c5ta10096h>
127. A.M. Osterholm, D.E. Shen, A.L. Dyer, J.R. Reynolds, Optimization of PEDOT films in ionic liquid supercapacitors: demonstration as a power source for polymer electrochromic devices. *ACS Appl. Mater. Interfaces* **5**, 13432–13440 (2013). <https://doi.org/10.1021/am4043454>
128. J. Xu, Z. Ku, Y. Zhang, D. Chao, H.J. Fan, Integrated photo-supercapacitor based on PEDOT modified printable perovskite solar cell. *Adv. Mater. Technol.* **1**, 1600074 (2016). <https://doi.org/10.1002/admt.201600074>
129. S.-B. Yoon, K.-B. Kim, Effect of poly(3,4-ethylenedioxythiophene) (PEDOT) on the pseudocapacitive properties of manganese oxide (MnO₂) in the PEDOT/MnO₂/multiwall carbon nanotube (MWNT) composite. *Electrochim. Acta* **106**, 135–142 (2013). <https://doi.org/10.1016/j.electacta.2013.05.058>
130. G. Cai, P. Darmawan, M. Cui, J. Wang, J. Chen, S. Magdassi, P.S. Lee, Highly stable transparent conductive silver grid/PEDOT:PSS electrodes for integrated bifunctional flexible electrochromic supercapacitors. *Adv. Energy Mater.* **6**, 1501882 (2016). <https://doi.org/10.1002/aenm.201501882>
131. D. Yang, Y. Song, Y.-J. Ye, M. Zhang, X. Sun, X.-X. Liu, Boosting the pseudocapacitance of nitrogen-rich carbon nanorod arrays for electrochemical capacitors. *J. Mater. Chem. A* **7**, 12086–12094 (2019). <https://doi.org/10.1039/c9ta01973a>
132. Y. Huang, J. Tao, W. Meng, M. Zhu, Y. Huang, Y. Fu, Y. Gao, C. Zhi, Super-high rate stretchable polypyrrole-based supercapacitors with excellent cycling stability. *Nano Energy* **11**, 518–525 (2015). <https://doi.org/10.1016/j.nanoen.2014.10.031>
133. J.G. Ibanez, M.E. Rincon, S. Gutierrez-Granados, M. Chahma, O.A. Jaramillo-Quintero, B.A. Frontana-Uribe, Conducting polymers in the fields of energy, environmental remediation, and chemical-chiral sensors. *Chem. Rev.* **118**, 4731–4816 (2018). <https://doi.org/10.1021/acs.chemrev.7b00482>
134. G. Sabouraud, S. Sadki, N. Brodie, The mechanisms of pyrrole electropolymerization. *Chem. Soc. Rev.* **29**, 283–293 (2000). <https://doi.org/10.1039/a807124a>
135. J. Jang, *Conducting Polymer Nanomaterials and Their Applications* (Springer, Berlin, 2006), pp. 189–260
136. S.C. Erwin, L. Zu, M.I. Haftel, A.L. Efros, T.A. Kennedy, D.J. Norris, Doping semiconductor nanocrystals. *Nature* **436**, 91–94 (2005). <https://doi.org/10.1038/nature03832>
137. T.F. Otero, J.G. Martinez, Structural and biomimetic chemical kinetics: kinetic magnitudes include structural information. *Adv. Funct. Mater.* **23**, 404–416 (2013). <https://doi.org/10.1002/adfm.201200719>
138. T. Liu, Y. Li, Addressing the achilles' heel of pseudocapacitive materials: long-term stability. *InfoMat* (2020). <https://doi.org/10.1002/inf2.12105>
139. Y. Shi, L. Peng, Y. Ding, Y. Zhao, G. Yu, Nanostructured conductive polymers for advanced energy storage. *Chem. Soc. Rev.* **44**, 6684–6696 (2015). <https://doi.org/10.1039/c5cs00362h>
140. B. Anothumakkool, A.T.A. Torris, S.N. Bhande, M.V. Badiger, S. Kurungot, Electrodeposited polyethylenedioxythiophene with infiltrated gel electrolyte interface: a close contest of an all-solid-state supercapacitor with its liquid-state counterpart. *Nanoscale* **6**, 5944–5952 (2014). <https://doi.org/10.1039/c4nr00659c>
141. Y. Xie, Y. Liu, Y. Zhao, Y.H. Tsang, S.P. Lau, H. Huang, Y. Chai, Stretchable all-solid-state supercapacitor with wavy shaped polyaniline/graphene electrode. *J. Mater. Chem. A* **2**, 9142–9149 (2014). <https://doi.org/10.1039/c4ta00734d>
142. S. Lehtimäki, M. Suominen, P. Damlin, S. Tuukkanen, C. Kvarnstrom, D. Lupo, Preparation of supercapacitors on flexible substrates with electrodeposited PEDOT/graphene composites. *ACS Appl. Mater. Interfaces* **7**, 22137–22147 (2015). <https://doi.org/10.1021/acsami.5b05937>

143. Y. Huang, M. Zhu, Z. Pei, Y. Huang, H. Geng, C. Zhi, Extremely stable polypyrrole achieved via molecular ordering for highly flexible supercapacitors. *ACS Appl. Mater. Interfaces* **8**, 2435–2440 (2016). <https://doi.org/10.1021/acsami.5b11815>
144. N. Kurra, M.K. Hota, H.N. Alshareef, Conducting polymer micro-supercapacitors for flexible energy storage and AC line-filtering. *Nano Energy* **13**, 500–508 (2015). <https://doi.org/10.1016/j.nanoen.2015.03.018>
145. N. Hui, F. Chai, P. Lin, Z. Song, X. Sun, Y. Li, S. Niu, X. Luo, Electrodeposited conducting polyaniline nanowire arrays aligned on carbon nanotubes network for high performance supercapacitors and sensors. *Electrochim. Acta* **199**, 234–241 (2016). <https://doi.org/10.1016/j.electacta.2016.03.115>
146. X.-Y. Peng, F. Luan, X.-X. Liu, D. Diamond, K.-T. Lau, pH-controlled morphological structure of polyaniline during electrochemical deposition. *Electrochim. Acta* **54**, 6172–6177 (2009). <https://doi.org/10.1016/j.electacta.2009.05.075>
147. B. Yao, L. Yuan, X. Xiao, J. Zhang, Y. Qi et al., Paper-based solid-state supercapacitors with pencil-drawing graphite/polyaniline networks hybrid electrodes. *Nano Energy* **2**, 1071–1078 (2013). <https://doi.org/10.1016/j.nanoen.2013.09.002>
148. Y. Wang, Y. Shi, L. Pan, Y. Ding, Y. Zhao, Y. Li, Y. Shi, G. Yu, Dopant-enabled supramolecular approach for controlled synthesis of nanostructured conductive polymer hydrogels. *Nano Lett.* **15**, 7736–7741 (2015). <https://doi.org/10.1021/acs.nanolett.5b03891>
149. Z.H. Huang, Y. Song, X.X. Xu, X.X. Liu, Ordered polypyrrole nanowire arrays grown on a carbon cloth substrate for a high-performance pseudocapacitor electrode. *ACS Appl. Mater. Interfaces* **7**, 25506–25513 (2015). <https://doi.org/10.1021/acsami.5b08830>
150. S. Huang, Y. Han, S. Lyu, W. Lin, P. Chen, S. Fang, A facile one-step approach for the fabrication of polypyrrole nanowire/carbon fiber hybrid electrodes for flexible high performance solid-state supercapacitors. *Nanotechnology* **28**, 435204 (2017). <https://doi.org/10.1088/1361-6528/aa84cb>
151. J. Huang, R.B. Kaner, Nanofiber formation in the chemical polymerization of aniline: a mechanistic study. *Angew. Chem. Int. Ed.* **43**, 5817–5821 (2004). <https://doi.org/10.1002/anie.200460616>
152. N.R. Chiou, C. Lu, J. Guan, L.J. Lee, A.J. Epstein, Growth and alignment of polyaniline nanofibres with superhydrophobic, superhydrophilic and other properties. *Nat. Nanotechnol.* **2**, 354–357 (2007). <https://doi.org/10.1038/nnano.2007.147>
153. K. Wang, J. Huang, Z. Wei, Conducting polyaniline nanowire arrays for high performance supercapacitors. *J. Phys. Chem. C* **114**, 8062–8067 (2010). <https://doi.org/10.1021/jp9113255>
154. Y.-J. Ye, Z.-H. Huang, Y. Song, J.-W. Geng, X.-X. Xu, X.-X. Liu, Electrochemical growth of polyaniline nanowire arrays on graphene sheets in partially exfoliated graphite foil for high-performance supercapacitive materials. *Electrochim. Acta* **240**, 72–79 (2017). <https://doi.org/10.1016/j.electacta.2017.04.025>
155. H.-P. Cong, X.-C. Ren, P. Wang, S.-H. Yu, Flexible graphene–polyaniline composite paper for high-performance supercapacitor. *Energy Environ. Sci.* **6**, 1185–1191 (2013). <https://doi.org/10.1039/c2ee24203f>
156. M. Yu, Y. Ma, J. Liu, S. Li, Polyaniline nanocone arrays synthesized on three-dimensional graphene network by electro-deposition for supercapacitor electrodes. *Carbon* **87**, 98–105 (2015). <https://doi.org/10.1016/j.carbon.2015.02.017>
157. G.F. Chen, X.X. Li, L.Y. Zhang, N. Li, T.Y. Ma, Z.Q. Liu, A porous perchlorate-doped polypyrrole nanocoating on nickel nanotube arrays for stable wide-potential-window supercapacitors. *Adv. Mater.* **28**, 7680–7687 (2016). <https://doi.org/10.1002/adma.201601781>
158. G. Lu, G. Shi, Electrochemical polymerization of pyrene in the electrolyte of boron trifluoride diethyl etherate containing trifluoroacetic acid and polyethylene glycol oligomer. *J. Electroanal. Chem.* **586**, 154–160 (2006). <https://doi.org/10.1016/j.jelechem.2005.10.020>
159. D.P. Dubal, S.H. Lee, J.G. Kim, W.B. Kim, C.D. Lokhande, Porous polypyrrole clusters prepared by electropolymerization for a high performance supercapacitor. *J. Mater. Chem.* **22**, 3044–3052 (2012). <https://doi.org/10.1039/c2jm14470k>
160. D.W. Wang, F. Li, J. Zhao, W. Ren, Z.G. Chen et al., Fabrication of graphene/polyaniline composite paper via in situ anodic electropolymerization for high-performance flexible electrode. *ACS Nano* **3**, 1745–1752 (2009). <https://doi.org/10.1021/nn900297m>
161. J. Han, Y. Dou, J. Zhao, M. Wei, D.G. Evans, X. Duan, Flexible CoAl LDH@PEDOT core/shell nanoplatelet array for high-performance energy storage. *Small* **9**, 98–106 (2013). <https://doi.org/10.1002/sml.201201336>
162. G. Lu, L. Qu, G. Shi, Electrochemical fabrication of neuron-type networks based on crystalline oligopyrene nanosheets. *Electrochim. Acta* **51**, 340–346 (2005). <https://doi.org/10.1016/j.electacta.2005.04.043>
163. X. He, W. Yang, X. Mao, L. Xu, Y. Zhou et al., All-solid state symmetric supercapacitors based on compressible and flexible free-standing 3D carbon nanotubes (CNTs)/poly(3,4-ethylenedioxythiophene) (PEDOT) sponge electrodes. *J. Power Sources* **376**, 138–146 (2018). <https://doi.org/10.1016/j.jpowsour.2017.09.084>
164. H. Park, J.W. Kim, S.Y. Hong, G. Lee, D.S. Kim, J.H. Oh et al., Microporous polypyrrole-coated graphene foam for high-performance multifunctional sensors and flexible supercapacitors. *Adv. Funct. Mater.* **28**, 1707013 (2018). <https://doi.org/10.1002/adfm.201707013>
165. C. Wang, Y. Ding, Y. Yuan, A. Cao, X. He, Q. Peng, Y. Li, Multifunctional, highly flexible, free-standing 3D polypyrrole foam. *Small* **12**, 4070–4076 (2016). <https://doi.org/10.1002/sml.201601905>
166. D.-Y. Feng, Z. Sun, Z.-H. Huang, X. Cai, Y. Song, X.-X. Liu, Highly loaded manganese oxide with high rate capability for capacitive applications. *J. Power Sources* **396**, 238–245 (2018). <https://doi.org/10.1016/j.jpowsour.2018.06.026>
167. T. Zhai, S. Xie, M. Yu, P. Fang, C. Liang, X. Lu, Y. Tong, Oxygen vacancies enhancing capacitive properties of MnO₂ nanorods for wearable asymmetric supercapacitors. *Nano*



- Energy **8**, 255–263 (2014). <https://doi.org/10.1016/j.nanoen.2014.06.013>
168. Z. Sun, S. Firdoz, E.Y. Yap, L. Li, X. Lu, Hierarchically structured MnO₂ nanowires supported on hollow Ni dendrites for high-performance supercapacitors. *Nanoscale* **5**, 4379–4387 (2013). <https://doi.org/10.1039/c3nr00209h>
169. W. Wei, X. Cui, W. Chen, D.G. Ivey, Phase-controlled synthesis of MnO₂ nanocrystals by anodic electrodeposition: implications for high-rate capability electrochemical supercapacitors. *J. Phys. Chem. C* **112**, 15075–15083 (2008). <https://doi.org/10.1021/jp804044s>
170. W. Wei, X. Cui, X. Mao, W. Chen, D.G. Ivey, Morphology evolution in anodically electrodeposited manganese oxide nanostructures for electrochemical supercapacitor applications—effect of supersaturation ratio. *Electrochim. Acta* **56**, 1619–1628 (2011). <https://doi.org/10.1016/j.electacta.2010.10.044>
171. F. Grote, Y. Lei, A complete three-dimensionally nanostructured asymmetric supercapacitor with high operating voltage window based on PPy and MnO₂. *Nano Energy* **10**, 63–70 (2014). <https://doi.org/10.1016/j.nanoen.2014.08.019>
172. S.B. Singh, T.I. Singh, N.H. Kim, J.H. Lee, A core-shell MnO₂@Au nanofiber network as a high-performance flexible transparent supercapacitor electrode. *J. Mater. Chem. A* **7**, 10672–10683 (2019). <https://doi.org/10.1039/c9ta00778d>
173. Q. Li, X.F. Lu, H. Xu, Y.X. Tong, G.R. Li, Carbon/MnO₂ double-walled nanotube arrays with fast ion and electron transmission for high-performance supercapacitors. *ACS Appl. Mater. Interfaces* **6**, 2726–2733 (2014). <https://doi.org/10.1021/am405271q>
174. H. Xia, J. Feng, H. Wang, M.O. Lai, L. Lu, MnO₂ nanotube and nanowire arrays by electrochemical deposition for supercapacitors. *J. Power Sources* **195**, 4410–4413 (2010). <https://doi.org/10.1016/j.jpowsour.2010.01.075>
175. J. Duay, S.A. Sherrill, Z. Gui, E. Gillette, S.B. Lee, Self-limiting electrodeposition of hierarchical MnO₂ and Mn(OH)₂/MnO₂ nanofibril/nanowires: mechanism and supercapacitor properties. *ACS Nano* **7**, 1200–1214 (2013). <https://doi.org/10.1021/nn3056077>
176. X. Lu, M. Yu, G. Wang, T. Zhai, S. Xie, Y. Ling, Y. Tong, Y. Li, H-TiO₂@MnO₂/H-TiO₂@C core-shell nanowires for high performance and flexible asymmetric supercapacitors. *Adv. Mater.* **25**, 267–272 (2013). <https://doi.org/10.1002/adma.201203410>
177. E. Eustache, C. Douard, R. Retoux, C. Lethien, T. Brousse, MnO₂ thin films on 3D scaffold: microsupercapacitor electrodes competing with “bulk” carbon electrodes. *Adv. Energy Mater.* **5**, 1500680 (2015). <https://doi.org/10.1002/aenm.201500680>
178. L. Yuan, X.H. Lu, X. Xiao, T. Zhai, J. Dai et al., Flexible solid-state supercapacitors based on carbon nanoparticles/MnO₂ nanorods hybrid structure. *ACS Nano* **6**, 656–661 (2012). <https://doi.org/10.1021/nn2041279>
179. S.H. Lee, H. Lee, M.S. Cho, J.-D. Nam, Y. Lee, Morphology and composition control of manganese oxide by the pulse reverse electrodeposition technique for high performance supercapacitors. *J. Mater. Chem. A* **1**, 14606–14611 (2013). <https://doi.org/10.1039/c3ta12828h>
180. X. Lu, D. Zheng, T. Zhai, Z. Liu, Y. Huang, S. Xie, Y. Tong, Facile synthesis of large-area manganese oxide nanorod arrays as a high-performance electrochemical supercapacitor. *Energy Environ. Sci.* **4**, 2915–2921 (2011). <https://doi.org/10.1039/c1ee01338f>
181. T. Beyazay, F. Eylul Sarac Oztuna, U. Unal, Self-standing reduced graphene oxide papers electrodeposited with manganese oxide nanostructures as electrodes for electrochemical capacitors. *Electrochim. Acta* **296**, 916–924 (2019). <https://doi.org/10.1016/j.electacta.2018.11.033>
182. Q. Chen, Y. Meng, C. Hu, Y. Zhao, H. Shao, N. Chen, L. Qu, MnO₂-modified hierarchical graphene fiber electrochemical supercapacitor. *J. Power Sources* **247**, 32–39 (2014). <https://doi.org/10.1016/j.jpowsour.2013.08.045>
183. H. Gao, F. Xiao, C.B. Ching, H. Duan, High-performance asymmetric supercapacitor based on graphene hydrogel and nanostructured MnO₂. *ACS Appl. Mater. Interfaces* **4**, 2801–2810 (2012). <https://doi.org/10.1021/am300455d>
184. S.H. Kazemi, M.A. Kiani, M. Ghaemmaghami, H. Kazemi, Nano-architected MnO₂ electrodeposited on the Cu-decorated nickel foam substrate as supercapacitor electrode with excellent areal capacitance. *Electrochim. Acta* **197**, 107–116 (2016). <https://doi.org/10.1016/j.electacta.2016.03.063>
185. M. Kundu, L. Liu, Direct growth of mesoporous MnO₂ nanosheet arrays on nickel foam current collectors for high-performance pseudocapacitors. *J. Power Sources* **243**, 676–681 (2013). <https://doi.org/10.1016/j.jpowsour.2013.06.059>
186. L. Li, X. Zhang, G. Wu, X. Peng, K. Huo, P.K. Chu, Supercapacitor electrodes based on hierarchical mesoporous MnO_x/nitrided TiO₂ nanorod arrays on carbon fiber paper. *Adv. Mater. Interfaces* **2**, 1400446 (2015). <https://doi.org/10.1002/admi.201400446>
187. S.-M. Li, Y.-S. Wang, S.-Y. Yang, C.-H. Liu, K.-H. Chang et al., Electrochemical deposition of nanostructured manganese oxide on hierarchically porous graphene-carbon nanotube structure for ultrahigh-performance electrochemical capacitors. *J. Power Sources* **225**, 347–355 (2013). <https://doi.org/10.1016/j.jpowsour.2012.10.037>
188. W. Li, K. Xu, B. Li, J. Sun, F. Jiang et al., MnO₂ nanoflower arrays with high rate capability for flexible supercapacitors. *ChemElectroChem* **1**, 1003–1008 (2014). <https://doi.org/10.1002/celec.201400006>
189. Y.-H. Lin, T.-Y. Wei, H.-C. Chien, S.-Y. Lu, Manganese oxide/carbon aerogel composite: an outstanding supercapacitor electrode material. *Adv. Energy Mater.* **1**, 901–907 (2011). <https://doi.org/10.1002/aenm.201100256>
190. Z. Pan, Y. Qiu, J. Yang, F. Ye, Y. Xu, X. Zhang, M. Liu, Y. Zhang, Ultra-endurance flexible all-solid-state asymmetric supercapacitors based on three-dimensionally coated MnO_x nanosheets on nanoporous current collectors. *Nano Energy* **26**, 610–619 (2016). <https://doi.org/10.1016/j.nanoen.2016.05.053>
191. Z. Qi, A. Younis, D. Chu, S. Li, A facile and template-free one-pot synthesis of Mn₃O₄ nanostructures as electrochemical

- supercapacitors. *Nano-Micro Lett.* **8**, 165–173 (2016). <https://doi.org/10.1007/s40820-015-0074-0>
192. A. Rafique, A. Massa, M. Fontana, S. Bianco, A. Chiodoni, C.F. Pirri, S. Hernandez, A. Lamberti, Highly uniform anodically deposited film of MnO₂ nanoflakes on carbon fibers for flexible and wearable fiber-shaped supercapacitors. *ACS Appl. Mater. Interfaces* **9**, 28386–28393 (2017). <https://doi.org/10.1021/acsami.7b06311>
193. W. Wei, X. Cui, W. Chen, D.G. Ivey, Electrochemical cyclability mechanism for MnO₂ electrodes utilized as electrochemical supercapacitors. *J. Power Sources* **186**, 543–550 (2009). <https://doi.org/10.1016/j.jpowsour.2008.10.058>
194. Z. Ye, T. Li, G. Ma, X. Peng, J. Zhao, Morphology controlled MnO₂ electrodeposited on carbon fiber paper for high-performance supercapacitors. *J. Power Sources* **351**, 51–57 (2017). <https://doi.org/10.1016/j.jpowsour.2017.03.104>
195. Y. Zheng, W. Pann, D. Zhengn, C. Sun, Fabrication of functionalized graphene-based MnO₂ nanoflower through electrodeposition for high-performance supercapacitor electrodes. *J. Electrochem. Soc.* **163**, D230–D238 (2016). <https://doi.org/10.1149/2.0341606jes>
196. B. Yao, S. Chandrasekaran, J. Zhang, W. Xiao, F. Qian, C. Zhu, E.B. Duoss, C.M. Spadaccini, M.A. Worsley, Y. Li, Efficient 3D printed pseudocapacitive electrodes with ultra-high MnO₂ loading. *Joule* **3**, 459–470 (2019). <https://doi.org/10.1016/j.joule.2018.09.020>
197. Y. Song, T. Liu, B. Yao, M. Li, T. Kou et al., Ostwald ripening improves rate capability of high mass loading manganese oxide for supercapacitors. *ACS Energy Lett.* **2**, 1752–1759 (2017). <https://doi.org/10.1021/acsenergylett.7b00405>
198. Z.-H. Huang, Y. Song, X.-X. Liu, Boosting operating voltage of vanadium oxide-based symmetric aqueous supercapacitor to 2V. *Chem. Eng. J.* **358**, 1529–1538 (2019). <https://doi.org/10.1016/j.cej.2018.10.136>
199. A.M. Engstrom, F.M. Doyle, Exploring the cycle behavior of electrodeposited vanadium oxide electrochemical capacitor electrodes in various aqueous environments. *J. Power Sources* **228**, 120–131 (2013). <https://doi.org/10.1016/j.jpowsour.2012.11.075>
200. A. Ghosh, E.J. Ra, M. Jin, H.-K. Jeong, T.H. Kim, C. Biswas, Y.H. Lee, High pseudocapacitance from ultrathin V₂O₅ films electrodeposited on self-standing carbon-nanofiber paper. *Adv. Funct. Mater.* **21**, 2541–2547 (2011). <https://doi.org/10.1002/adfm.201002603>
201. R.S. Ingole, B.J. Lokhande, Electrochemically synthesized mesoporous architecture of vanadium oxide on flexible stainless steel for high performance supercapacitor. *J. Mater. Sci.: Mater. Electron.* **28**, 10951–10957 (2017). <https://doi.org/10.1007/s10854-017-6875-9>
202. C.-H. Lai, C.-K. Lin, S.-W. Lee, H.-Y. Li, J.-K. Chang, M.-J. Deng, Nanostructured Na-doped vanadium oxide synthesized using an anodic deposition technique for supercapacitor applications. *J. Alloys Compd.* **536**, S428–S431 (2012). <https://doi.org/10.1016/j.jallcom.2011.12.038>
203. E. Armstrong, M. O'Sullivan, J. O'Connell, J.D. Holmes, C. O'Dwyer, 3D vanadium oxide inverse opal growth by electrodeposition. *J. Electrochem. Soc.* **162**, D605–D612 (2015). <https://doi.org/10.1149/2.0541514jes>
204. D.L. da Silva, R.G. Delatorre, G. Pattanaik, G. Zangari, W. Figueiredo, R.-P. Blum, H. Niehus, A.A. Pasa, Electrochemical synthesis of vanadium oxide nanofibers. *J. Electrochem. Soc.* **155**, E14 (2008). <https://doi.org/10.1149/1.2804856>
205. Y.R. Lu, T.Z. Wu, C.L. Chen, D.H. Wei, J.L. Chen, W.C. Chou, C.L. Dong, Mechanism of electrochemical deposition and coloration of electrochromic V₂O₅ nano thin films: an in situ X-ray spectroscopy study. *Nanoscale Res. Lett.* **10**, 387 (2015). <https://doi.org/10.1186/s11671-015-1095-9>
206. D. Rehnlund, M. Valvo, K. Edström, L. Nyholm, Electrodeposition of vanadium oxide/manganese oxide hybrid thin films on nanostructured aluminum substrates. *J. Electrochem. Soc.* **161**, D515–D521 (2014). <https://doi.org/10.1149/2.0511410jes>
207. K. Takahashi, S.J. Limmer, Y. Wang, G. Cao, Synthesis and electrochemical properties of single-crystal V₂O₅ nanorod arrays by template-based electrodeposition. *J. Phys. Chem. B* **108**, 9795–9800 (2004). <https://doi.org/10.1021/jp0491820>
208. Y. Wang, K. Takahashi, H. Shang, G. Cao, Synthesis and electrochemical properties of vanadium pentoxide nanotube arrays. *J. Phys. Chem. B* **109**, 3085–3088 (2005). <https://doi.org/10.1021/jp044286w>
209. J.-D. Xie, H.-Y. Li, T.-Y. Wu, J.-K. Chang, Y.A. Gandomi, Electrochemical energy storage of nanocrystalline vanadium oxide thin films prepared from various plating solutions for supercapacitors. *Electrochim. Acta* **273**, 257–263 (2018). <https://doi.org/10.1016/j.electacta.2018.04.007>
210. H. Drosos, A. Sapountzis, E. Koudoumas, N. Katsarakis, D. Vernardou, Effect of deposition current density on electrodeposited vanadium oxide coatings. *J. Mater. Chem.* **159**, E145–E147 (2012). <https://doi.org/10.1149/2.017208jes>
211. Q. Qu, Y. Zhu, X. Gao, Y. Wu, Core-shell structure of polypyrrole grown on V₂O₅ nanoribbon as high performance anode material for supercapacitors. *Adv. Energy Mater.* **2**, 950–955 (2012). <https://doi.org/10.1002/aenm.201200088>
212. J.G. Wang, H. Liu, H. Liu, W. Hua, M. Shao, Interfacial constructing flexible V₂O₅@polypyrrole core-shell nanowire membrane with superior supercapacitive performance. *ACS Appl. Mater. Interfaces.* **10**, 18816–18823 (2018). <https://doi.org/10.1021/acsami.8b05660>
213. T.M. McEvoy, K.J. Stevenson, Elucidation of the electrodeposition mechanism of molybdenum oxide from iso- and peroxy-polymolybdate solutions. *J. Mater. Res.* **19**, 429–438 (2011). <https://doi.org/10.1557/jmr.2004.19.2.429>
214. V.S. Saji, C.W. Lee, Molybdenum, molybdenum oxides, and their electrochemistry. *Chemosuschem* **5**, 1146–1161 (2012). <https://doi.org/10.1002/cssc.201100660>
215. W. Zhang, H. Li, C.J. Firby, M. Al-Hussein, A.Y. Elezzabi, Oxygen-vacancy-tunable electrochemical properties of electrodeposited molybdenum oxide films. *ACS Appl. Mater. Interfaces.* **11**, 20378–20385 (2019). <https://doi.org/10.1021/acsami.9b04386>
216. H. Farsi, F. Gobal, H. Raissi, S. Moghiminia, The pH effects on the capacitive behavior of nanostructured molybdenum



- oxide. *J. Solid State Electrochem.* **14**, 681–686 (2009). <https://doi.org/10.1007/s10008-009-0828-z>
217. H. Farsi, F. Gobal, H. Raissi, S. Moghiminia, On the pseudocapacitive behavior of nanostructured molybdenum oxide. *J. Solid State Electrochem.* **14**, 643–650 (2009). <https://doi.org/10.1007/s10008-009-0830-5>
218. T. Tsumura, Lithium insertion/extraction reaction on crystalline MoO_3 . *Solid State Ion.* **104**, 183–189 (1997). [https://doi.org/10.1016/s0167-2738\(97\)00418-9](https://doi.org/10.1016/s0167-2738(97)00418-9)
219. C.R. Clayton, Y.C. Lu, Electrochemical and XPS evidence of the aqueous formation of Mo_2O_5 . *Surf. Interface Anal.* **14**, 66–70 (1989). <https://doi.org/10.1002/sia.740140114>
220. C. Liu, Z. Xie, W. Wang, Z. Li, Z. Zhang, The Ti@MoO_x nanorod array as a three-dimensional film electrode for micro-supercapacitors. *Electrochem. Commun.* **44**, 23–26 (2014). <https://doi.org/10.1016/j.elecom.2014.04.007>
221. C. Liu, Z. Xie, W. Wang, Z. Li, Z. Zhang, Fabrication of MoO_x film as a conductive anode material for micro-supercapacitors by electrodeposition and annealing. *J. Electrochem. Soc.* **161**, A1051–A1057 (2014). <https://doi.org/10.1149/2.081406jes>
222. K.K. Upadhyay, T. Nguyen, T.M. Silva, M.J. Carmezim, M.F. Montemor, Electrodeposited MoO_x films as negative electrode materials for redox supercapacitors. *Electrochim. Acta* **225**, 19–28 (2017). <https://doi.org/10.1016/j.electacta.2016.12.106>
223. D.D. Yao, J.Z. Ou, K. Latham, S. Zhuiykov, A.P. O'Mullane, K. Kalantar-zadeh, Electrodeposited α - and β -phase MoO_3 films and investigation of their gasochromic properties. *Cryst. Growth Des.* **12**, 1865–1870 (2012). <https://doi.org/10.1021/cg201500b>
224. F. Wang, Z. Liu, X. Wang, X. Yuan, X. Wu, Y. Zhu, L. Fu, Y. Wu, A conductive polymer coated MoO_3 anode enables an Al-ion capacitor with high performance. *J. Mater. Chem. A* **4**, 5115–5123 (2016). <https://doi.org/10.1039/c6ta01398h>
225. S. Sun, X. Liao, Y. Sun, G. Yin, Y. Yao, Z. Huang, X. Pu, Facile synthesis of a α - MoO_3 nanoplate/ TiO_2 nanotube composite for high electrochemical performance. *RSC Adv.* **7**, 22983–22989 (2017). <https://doi.org/10.1039/c7ra01164d>
226. X. Xiao, T. Ding, L. Yuan, Y. Shen, Q. Zhong et al., $\text{WO}_{3-x}/\text{MoO}_3$ Electrochemical and XPS evidence of the aqueous formation of Mo_2O_{5x} core/shell nanowires on carbon fabric as an anode for all-solid-state asymmetric supercapacitors. *Adv. Energy Mater.* **2**, 1328–1332 (2012). <https://doi.org/10.1002/aenm.201200380>
227. G.-R. Li, Z.-L. Wang, F.-L. Zheng, Y.-N. Ou, Y.-X. Tong, ZnO@MoO_3 core/shell nanocables: facile electrochemical synthesis and enhanced supercapacitor performances. *J. Mater. Chem.* **21**, 4217–4221 (2011). <https://doi.org/10.1039/c0jm03500a>
228. J.-C. Liu, H. Li, M. Batmunkh, X. Xiao, Y. Sun et al., Structural engineering to maintain the superior capacitance of molybdenum oxides at ultrahigh mass loadings. *J. Mater. Chem. A* **7**, 23941–23948 (2019). <https://doi.org/10.1039/c9ta04835a>
229. X.F. Lu, Z.X. Huang, Y.X. Tong, G.R. Li, Asymmetric supercapacitors with high energy density based on helical hierarchical porous Na_xMnO_2 and MoO_2 . *Chem. Sci.* **7**, 510–517 (2016). <https://doi.org/10.1039/c5sc03326h>
230. H. Zheng, J.Z. Ou, M.S. Strano, R.B. Kaner, A. Mitchell, K. Kalantar-zadeh, Nanostructured tungsten oxide-properties, synthesis, and applications. *Adv. Funct. Mater.* **21**, 2175–2196 (2011). <https://doi.org/10.1002/adfm.201002477>
231. B. Yang, H. Li, M. Blackford, V. Luca, Novel low density mesoporous WO_3 films prepared by electrodeposition. *Curr. Appl. Phys.* **6**, 436–439 (2006). <https://doi.org/10.1016/j.cap.2005.11.035>
232. S. Wang, X. Feng, J. Yao, L. Jiang, Controlling wettability and photochromism in a dual-responsive tungsten oxide film. *Angew. Chem. Int. Ed.* **45**, 1264–1267 (2006). <https://doi.org/10.1002/anie.200502061>
233. P. Shen, N. Chi, K.-Y. Chan, Morphology of electrodeposited WO_3 studied by atomic force microscopy. *J. Mater. Chem.* **10**, 697–700 (2000). <https://doi.org/10.1039/a908348k>
234. Z. Sun, X.G. Sang, Y. Song, D. Guo, D.Y. Feng, X. Sun, X.X. Liu, A high performance tungsten bronze electrode in a mixed electrolyte and applications in supercapacitors. *Chem. Commun.* **55**, 14323–14326 (2019). <https://doi.org/10.1039/c9cc06845g>
235. G. Yang, X.-X. Liu, Electrochemical fabrication of interconnected tungsten bronze nanosheets for high performance supercapacitor. *J. Power Sources* **383**, 17–23 (2018). <https://doi.org/10.1016/j.jpowsour.2018.02.035>
236. T. Pauporté, A simplified method for WO_3 electrodeposition. *J. Electrochem. Soc.* **149**, C539–C545 (2002). <https://doi.org/10.1088/2053-1583/ab1e0a>
237. S.H. Baeck, K.S. Choi, T.F. Jaramillo, G.D. Stucky, E.W. McFarland, Enhancement of photocatalytic and electrochromic properties of electrochemically fabricated mesoporous WO_3 thin films. *Adv. Mater.* **15**, 1269–1273 (2003). <https://doi.org/10.1002/adma.200304669>
238. A.K. Srivastava, M. Deepa, S. Singh, R. Kishore, S.A. Agnihotry, Microstructural and electrochromic characteristics of electrodeposited and annealed WO_3 films. *Solid State Ionics* **176**, 1161–1168 (2005). <https://doi.org/10.1016/j.ssi.2004.10.006>
239. M. Deepa, A.K. Srivastava, T.K. Saxena, S.A. Agnihotry, Annealing induced microstructural evolution of electrodeposited electrochromic tungsten oxide films. *Appl. Surf. Sci.* **252**, 1568–1580 (2005). <https://doi.org/10.1016/j.apsusc.2005.02.123>
240. M. Deepa, M. Kar, S.A. Agnihotry, Electrodeposited tungsten oxide films: annealing effects on structure and electrochromic performance. *Thin Solid Films* **468**, 32–42 (2004). <https://doi.org/10.1016/j.tsf.2004.04.056>
241. C. Yao, B. Wei, H. Li, G. Wang, Q. Han, H. Ma, Q. Gong, Carbon-encapsulated tungsten oxide nanowires as a stable and high-rate anode material for flexible asymmetric supercapacitors. *J. Mater. Chem. A* **5**, 56–61 (2017). <https://doi.org/10.1039/c6ta08274b>

242. Y. Zeng, M. Yu, Y. Meng, P. Fang, X. Lu, Y. Tong, Iron-based supercapacitor electrodes: advances and challenges. *Adv. Energy Mater.* **6**, 1601053 (2016). <https://doi.org/10.1002/aenm.201601053>
243. Q. Xia, M. Xu, H. Xia, J. Xie, Nanostructured iron oxide/hydroxide-based electrode materials for supercapacitors. *ChemNanoMat* **2**, 588–600 (2016). <https://doi.org/10.1002/cnma.201600110>
244. J. Chen, J. Xu, S. Zhou, N. Zhao, C.-P. Wong, Amorphous nanostructured FeOOH and Co–Ni double hydroxides for high-performance aqueous asymmetric supercapacitors. *Nano Energy* **21**, 145–153 (2016). <https://doi.org/10.1016/j.nanoen.2015.12.029>
245. X.-F. Lu, X.-Y. Chen, W. Zhou, Y.-X. Tong, G.-R. Li, α -Fe₂O₃@PANI core–shell nanowire arrays as negative electrodes for asymmetric supercapacitors. *ACS Appl. Mater. Interfaces* **7**, 14843–14850 (2015). <https://doi.org/10.1021/acsami.5b03126>
246. J. Liu, M. Zheng, X. Shi, H. Zeng, H. Xia, Amorphous FeOOH quantum dots assembled mesoporous film anchored on graphene nanosheets with superior electrochemical performance for supercapacitors. *Adv. Funct. Mater.* **26**, 919–930 (2016). <https://doi.org/10.1002/adfm.201504019>
247. J. Sun, Y. Huang, C. Fu, Y. Huang, M. Zhu, X. Tao, C. Zhi, H. Hu, A high performance fiber-shaped PEDOT@MnO₂/C@Fe₃O₄ asymmetric supercapacitor for wearable electronics. *J. Mater. Chem. A* **4**, 14877–14883 (2016). <https://doi.org/10.1039/c6ta05898a>
248. M.-S. Wu, R.-H. Lee, Electrochemical growth of iron oxide thin films with nanorods and nanosheets for capacitors. *J. Electrochem. Soc.* **156**, A737–A743 (2009). <https://doi.org/10.1149/1.3160547>
249. K.A. Owusu, L. Qu, J. Li, Z. Wang, K. Zhao et al., Low-crystalline iron oxide hydroxide nanoparticle anode for high-performance supercapacitors. *Nat. Commun.* **8**, 14264 (2017). <https://doi.org/10.1038/ncomms14264>
250. W. Fu, E. Zhao, X. Ren, A. Magasinski, G. Yushin, Hierarchical fabric decorated with carbon nanowire/metal oxide nanocomposites for 1.6 V wearable aqueous supercapacitors. *Adv. Energy Mater.* **8**, 1703454 (2018). <https://doi.org/10.1002/aenm.201703454>
251. Y.C. Chen, Y.G. Lin, Y.K. Hsu, S.C. Yen, K.H. Chen, L.C. Chen, Novel iron oxyhydroxide lepidocrocite nanosheet as ultrahigh power density anode material for asymmetric supercapacitors. *Small* **10**, 3803–3810 (2014). <https://doi.org/10.1002/sml.201400597>
252. X. Tang, R. Jia, T. Zhai, H. Xia, Hierarchical Fe₃O₄@Fe₂O₃ core–shell nanorod arrays as high-performance anodes for asymmetric supercapacitors. *ACS Appl. Mater. Interfaces* **7**, 27518–27525 (2015). <https://doi.org/10.1021/acsami.5b09766>
253. Y. Li, J. Xu, T. Feng, Q. Yao, J. Xie, H. Xia, Fe₂O₃ nanoneedles on ultrafine nickel nanotube arrays as efficient anode for high-performance asymmetric supercapacitors. *Adv. Funct. Mater.* **27**, 1606728 (2017). <https://doi.org/10.1002/adfm.201606728>
254. T. Deng, W. Zhang, O. Arcelus, J.G. Kim, J. Carrasco et al., Atomic-level energy storage mechanism of cobalt hydroxide electrode for pseudocapacitors. *Nat. Commun.* **8**, 15194 (2017). <https://doi.org/10.1038/ncomms15194>
255. V. Gupta, S. Gupta, N. Miura, Potentiostatically deposited nanostructured Co_xNi_{1-x} layered double hydroxides as electrode materials for redox-supercapacitors. *J. Power Sources* **175**, 680–685 (2008). <https://doi.org/10.1016/j.jpowsour.2007.09.004>
256. Y. Zeng, Z. Lai, Y. Han, H. Zhang, S. Xie, X. Lu, Oxygen-vacancy and surface modulation of ultrathin nickel cobaltite nanosheets as a high-energy cathode for advanced Zn-ion batteries. *Adv. Mater.* **30**, 1802396 (2018). <https://doi.org/10.1002/adma.201802396>
257. Y. Zeng, Y. Meng, Z. Lai, X. Zhang, M. Yu et al., An ultrastable and high-performance flexible fiber-shaped Ni–Zn battery based on a Ni–NiO heterostructured nanosheet cathode. *Adv. Mater.* **29**, 1702698 (2017). <https://doi.org/10.1002/adma.201702698>
258. M. Huang, M. Li, C. Niu, Q. Li, L. Mai, Recent advances in rational electrode designs for high-performance alkaline rechargeable batteries. *Adv. Funct. Mater.* **29**, 1807847 (2019). <https://doi.org/10.1002/adfm.201807847>
259. Y. Liu, N. Fu, G. Zhang, M. Xu, W. Lu, L. Zhou, H. Huang, Design of hierarchical Ni–Co@Ni–Co layered double hydroxide core–shell structured nanotube array for high-performance flexible all-solid-state battery-type supercapacitors. *Adv. Funct. Mater.* **27**, 1605307 (2017). <https://doi.org/10.1002/adfm.201605307>
260. G. Nagaraju, S. Chandra Sekhar, L. Krishna Bharat, J.S. Yu, Wearable fabrics with self-branched bimetallic layered double hydroxide coaxial nanostructures for hybrid supercapacitors. *ACS Nano* **11**, 10860–10874 (2017). <https://doi.org/10.1021/acs.nano.7b04368>
261. T. Wang, B. Zhao, H. Jiang, H.-P. Yang, K. Zhang et al., Electro-deposition of CoNi₂S₄ flower-like nanosheets on 3D hierarchically porous nickel skeletons with high electrochemical capacitive performance. *J. Mater. Chem. A* **3**, 23035–23041 (2015). <https://doi.org/10.1039/c5ta04705f>
262. H. Xu, C. Zhang, W. Zhou, G.R. Li, Co(OH)₂/RGO/NiO sandwich-structured nanotube arrays with special surface and synergistic effects as high-performance positive electrodes for asymmetric supercapacitors. *Nanoscale* **7**, 16932–16942 (2015). <https://doi.org/10.1039/c5nr04449a>
263. G. Xiong, P. He, D. Wang, Q. Zhang, T. Chen, T.S. Fisher, Hierarchical Ni–Co hydroxide petals on mechanically robust graphene petal foam for high-energy asymmetric supercapacitors. *Adv. Funct. Mater.* **26**, 5460–5470 (2016). <https://doi.org/10.1002/adfm.201600879>
264. J.A. Syed, J. Ma, B. Zhu, S. Tang, X. Meng, Hierarchical multicomponent electrode with interlaced Ni(OH)₂ nanoflakes wrapped zinc cobalt sulfide nanotube arrays for sustainable high-performance supercapacitors. *Adv. Energy Mater.* **7**, 1701228 (2017)
265. X. Lu, X. Huang, S. Xie, T. Zhai, C. Wang et al., Controllable synthesis of porous nickel–cobalt oxide nanosheets for

- supercapacitors. *J. Mater. Chem.* **22**, 13357–13364 (2012). <https://doi.org/10.1039/c2jm30927k>
266. H. Li, Y. Gao, C. Wang, G. Yang, A simple electrochemical route to access amorphous mixed-metal hydroxides for supercapacitor electrode materials. *Adv. Energy Mater.* **5**, 1401767 (2015). <https://doi.org/10.1002/aenm.201401767>
267. X. Xia, J. Tu, Y. Zhang, J. Chen, X. Wang, C. Gu, C. Guan, J. Luo, H.J. Fan, Porous hydroxide nanosheets on preformed nanowires by electrodeposition: branched nanoarrays for electrochemical energy storage. *Chem. Mater.* **24**, 3793–3799 (2012). <https://doi.org/10.1021/cm302416d>
268. W. Guo, C. Yu, S. Li, X. Song, H. Huang et al., A universal converse voltage process for triggering transition metal hybrids in situ phase reconstruction toward ultrahigh-rate supercapacitors. *Adv. Mater.* **31**, 1901241 (2019). <https://doi.org/10.1002/adma.201901241>
269. J.C. Chen, C.-T. Hsu, C.-C. Hu, Superior capacitive performances of binary nickel–cobalt hydroxide nanonetwork prepared by cathodic deposition. *J. Power Sources* **253**, 205–213 (2014). <https://doi.org/10.1016/j.jpowsour.2013.12.073>
270. R. Li, S. Wang, Z. Huang, F. Lu, T. He, NiCo₂S₄@Co(OH)₂ core–shell nanotube arrays in situ grown on Ni foam for high performances asymmetric supercapacitors. *J. Power Sources* **312**, 156–164 (2016). <https://doi.org/10.1016/j.jpowsour.2016.02.047>
271. H. Pourfarzad, M. Shabani-Nooshabadi, M.R. Ganjali, H. Kashani, Synthesis of Ni–Co–Fe layered double hydroxide and Fe₂O₃/graphene nanocomposites as active materials for high electrochemical performance supercapacitors. *Electrochim. Acta* **317**, 83–92 (2019). <https://doi.org/10.1016/j.electacta.2019.05.122>
272. Z. Li, H. Duan, M. Shao, J. Li, D. O’Hare, M. Wei, Z.L. Wang, Ordered-vacancy-induced cation intercalation into layered double hydroxides: a general approach for high-performance supercapacitors. *Chem* **4**, 2168–2179 (2018). <https://doi.org/10.1016/j.chempr.2018.06.007>
273. G. Lee, J.W. Kim, H. Park, J.Y. Lee, H. Lee et al., Dynamically stretchable, planar supercapacitors with buckled carbon nanotube/Mn–Mo mixed oxide electrodes and air-stable organic electrolyte. *ACS Nano* **13**, 855–866 (2019). <https://doi.org/10.1021/acsnano.8b08645>
274. K. Okamura, R. Inoue, T. Seville, K. Tomono, M. Nakayama, An approach to optimize the composition of supercapacitor electrodes consisting of manganese–molybdenum mixed oxide and carbon nanotubes. *J. Electrochem. Soc.* **158**, A711 (2011). <https://doi.org/10.1149/1.3578039>
275. Y.-H. Li, Q.-Y. Li, H.-Q. Wang, Y.-G. Huang, X.-H. Zhang et al., Synthesis and electrochemical properties of nickel–manganese oxide on MWCNTs/CFP substrate as a supercapacitor electrode. *Appl. Energy* **153**, 78–86 (2015). <https://doi.org/10.1016/j.apenergy.2014.09.055>
276. H. Zhou, X. Zou, K. Zhang, P. Sun, M.S. Islam, J. Gong, Y. Zhang, J. Yang, Molybdenum–tungsten mixed oxide deposited into titanium dioxide nanotube arrays for ultrahigh rate supercapacitors. *ACS Appl. Mater. Interfaces* **9**, 18699–18709 (2017). <https://doi.org/10.1021/acsnano.8b08645>
277. E. Karaca, D. Gökçen, N.Ö. Pekmez, K. Pekmez, Electrochemical synthesis of PPy composites with nanostructured MnO_x, CoO_x, NiO_x, and FeO_x in acetonitrile for supercapacitor applications. *Electrochim. Acta* **305**, 502–513 (2019). <https://doi.org/10.1016/j.electacta.2019.03.060>
278. C.H. Ng, H.N. Lim, Y.S. Lim, W.K. Chee, N.M. Huang, Fabrication of flexible polypyrrole/graphene oxide/manganese oxide supercapacitor. *Int. J. Energy Res.* **39**, 344–355 (2015). <https://doi.org/10.1002/er.3247>
279. L. Chen, L.-J. Sun, F. Luan, Y. Liang, Y. Li, X.-X. Liu, Synthesis and pseudocapacitive studies of composite films of polyaniline and manganese oxide nanoparticles. *J. Power Sources* **195**, 3742–3747 (2010). <https://doi.org/10.1016/j.jpowsour.2009.12.036>
280. J. Kim, H. Ju, A.I. Inamdar, Y. Jo, J. Han, H. Kim, H. Im, Synthesis and enhanced electrochemical supercapacitor properties of Ag–MnO₂–polyaniline nanocomposite electrodes. *Energy* **70**, 473–477 (2014). <https://doi.org/10.1016/j.energy.2014.04.018>
281. Z. Su, C. Yang, C. Xu, H. Wu, Z. Zhang et al., Co-electrodeposition of the MnO₂–PEDOT:PSS nanostructured composite for high areal mass, flexible asymmetric supercapacitor devices. *J. Mater. Chem. A* **1**, 12432 (2013). <https://doi.org/10.1039/c3ta13148c>
282. Z. Wang, J. Du, M. Zhang, J. Yu, H. Liu et al., Continuous preparation of high performance flexible asymmetric supercapacitor with a very fast, low-cost, simple and scalable electrochemical co-deposition method. *J. Power Sources* **437**, 226827 (2019). <https://doi.org/10.1016/j.jpowsour.2019.226827>
283. P. Asen, S. Shahrokhian, A. Irajizad, One step electrodeposition of V₂O₅/polypyrrole/graphene oxide ternary nanocomposite for preparation of a high performance supercapacitor. *Int. J. Hydrog. Energy* **42**, 21073–21085 (2017). <https://doi.org/10.1016/j.ijhydene.2017.07.008>
284. M.H. Bai, L.J. Bian, Y. Song, X.X. Liu, Electrochemical codeposition of vanadium oxide and polypyrrole for high-performance supercapacitor with high working voltage. *ACS Appl. Mater. Interfaces* **6**, 12656–12664 (2014). <https://doi.org/10.1021/am502630g>
285. M.-Y. Zhang, Y. Song, D. Guo, D. Yang, X. Sun et al., Strongly coupled polypyrrole/molybdenum oxide hybrid films via electrochemical layer-by-layer assembly for pseudocapacitors. *J. Mater. Chem. A* **7**, 9815–9821 (2019). <https://doi.org/10.1039/c9ta00705a>
286. J.-W. Geng, Y.-J. Ye, D. Guo, X.-X. Liu, Concurrent electropolymerization of aniline and electrochemical deposition of tungsten oxide for supercapacitor. *J. Power Sources* **342**, 980–989 (2017). <https://doi.org/10.1016/j.jpowsour.2017.01.029>
287. Y. Wang, S. Dong, X. Wu, M. Li, One-step electrodeposition of MnO₂@NiAl layered double hydroxide nanostructures on the nickel foam for high-performance supercapacitors. *J. Electrochem. Soc.* **164**, H56–H62 (2016). <https://doi.org/10.1149/2.0861702jes>
288. Z. Zeng, P. Sun, J. Zhu, X. Zhu, Porous petal-like Ni(OH)₂–MnO_x nanosheet electrodes grown on carbon fiber

- paper for supercapacitors. *Surf. Interfaces* **8**, 73–82 (2017). <https://doi.org/10.1016/j.surfin.2017.04.011>
289. B.-X. Zou, Y. Liang, X.-X. Liu, D. Diamond, K.-T. Lau, Electrodeposition and pseudocapacitive properties of tungsten oxide/polyaniline composite. *J. Power Sources* **196**, 4842–4848 (2011). <https://doi.org/10.1016/j.jpowsour.2011.01.073>
290. X. Fan, X. Wang, G. Li, A. Yu, Z. Chen, High-performance flexible electrode based on electrodeposition of polypyrrole/MnO₂ on carbon cloth for supercapacitors. *J. Power Sources* **326**, 357–364 (2016). <https://doi.org/10.1016/j.jpowsour.2016.05.047>
291. C.-C. Hu, C.-Y. Hung, K.-H. Chang, Y.-L. Yang, A hierarchical nanostructure consisting of amorphous MnO₂, Mn₃O₄ nanocrystallites, and single-crystalline MnOOH nanowires for supercapacitors. *J. Power Sources* **196**, 847–850 (2011). <https://doi.org/10.1016/j.jpowsour.2010.08.001>
292. P. Tang, L. Han, L. Zhang, Facile synthesis of graphite/PEDOT/MnO₂ composites on commercial supercapacitor separator membranes as flexible and high-performance supercapacitor electrodes. *ACS Appl. Mater. Interfaces* **6**, 10506–10515 (2014). <https://doi.org/10.1021/am5021028>
293. N. Zhao, H. Fan, M. Zhang, C. Wang, X. Ren et al., Preparation of partially-cladding NiCo-LDH/Mn₃O₄ composite by electrodeposition route and its excellent supercapacitor performance. *J. Alloys Compd.* **796**, 111–119 (2019). <https://doi.org/10.1016/j.jallcom.2019.05.023>
294. D.V. Zhuzhelskii, E.G. Tolstojatova, S.N. Eliseeva, A.V. Ivanov, S. Miao, V.V. Kondratiev, Electrochemical properties of PEDOT/WO₃ composite films for high performance supercapacitor application. *Electrochim. Acta* **299**, 182–190 (2019). <https://doi.org/10.1016/j.electacta.2019.01.007>
295. S.-Q. Wang, X. Cai, Y. Song, X. Sun, X.-X. Liu, VO_x@MoO₃ nanorod composite for high-performance supercapacitors. *Adv. Funct. Mater.* **28**, 1803901 (2018). <https://doi.org/10.1002/adfm.201803901>
296. G.-F. Chen, Z.-Q. Liu, J.-M. Lin, N. Li, Y.-Z. Su, Hierarchical polypyrrole based composites for high performance asymmetric supercapacitors. *J. Power Sources* **283**, 484–493 (2015). <https://doi.org/10.1016/j.jpowsour.2015.02.103>
297. J. Yang, C. Yu, X. Fan, S. Liang, S. Li, H. Huang, Z. Ling, C. Hao, J. Qiu, Electroactive edge site-enriched nickel-cobalt sulfide into graphene frameworks for high-performance asymmetric supercapacitors. *Energy Environ. Sci.* **9**, 1299–1307 (2016). <https://doi.org/10.1039/c5ee03633j>
298. J. Zeng, J. Liu, S.S. Siwal, W. Yang, X. Fu, Q. Zhang, Morphological and electronic modification of 3D porous nickel microsphere arrays by cobalt and sulfur dual synergistic modulation for overall water splitting electrolysis and supercapacitors. *Appl. Surf. Sci.* **491**, 570–578 (2019). <https://doi.org/10.1016/j.apsusc.2019.06.182>
299. B.D. Falola, L. Fan, T. Wiltowski, I.I. Suni, Electrodeposition of Cu-doped MoS₂ for charge storage in electrochemical supercapacitors. *J. Electrochem. Soc.* **164**, D674–D679 (2017). <https://doi.org/10.1149/2.0421712jes>
300. B.D. Falola, T. Wiltowski, I.I. Suni, Electrodeposition of MoS₂ for charge storage in electrochemical supercapacitors. *J. Electrochem. Soc.* **163**, D568–D574 (2016). <https://doi.org/10.1149/2.0011610jes>
301. X. Zhang, J. Gong, K. Zhang, W. Zhu, J.-C. Li, Q. Ding, All-solid-state asymmetric supercapacitor based on porous cobalt selenide thin films. *J. Alloys Compd.* **772**, 25–32 (2019). <https://doi.org/10.1016/j.jallcom.2018.09.023>
302. W. Chen, C. Xia, H.N. Alshareef, One-step electrodeposited nickel cobalt sulfide nanosheet arrays for high-performance asymmetric supercapacitors. *ACS Nano* **8**, 9531–9541 (2014). <https://doi.org/10.1021/nn503814y>
303. K.R. Prasad, K. Koga, N. Miura, Electrochemical deposition of nanostructured indium oxide: high-performance electrode material for redox supercapacitors. *Chem. Mater.* **16**, 1845–1847 (2004). <https://doi.org/10.1021/cm0497576>
304. A. Albu-Yaron, C. Lévy-Clément, A. Katty, S. Bastide, R. Tenne, Influence of the electrochemical deposition parameters on the microstructure of MoS₂ thin films. *Thin Solid Films* **361–362**, 223–228 (2000). [https://doi.org/10.1016/s0040-6090\(99\)00838-x](https://doi.org/10.1016/s0040-6090(99)00838-x)
305. W. Deng, X. Feng, Y. Xiao, C. Li, Layered molybdenum (oxy) pyrophosphate (MoO₂)₂P₂O₇ as a cathode material for sodium-ion batteries. *ChemElectroChem* **5**, 1032–1036 (2018). <https://doi.org/10.1002/celec.201800005>
306. B. Wen, N.A. Chernova, R. Zhang, Q. Wang, F. Omenya, J. Fang, M.S. Whittingham, Layered molybdenum (oxy)pyrophosphate as cathode for lithium-ion batteries. *Chem. Mat.* **25**, 3513–3521 (2013). <https://doi.org/10.1021/cm401946h>
307. C. Masquelier, L. Croguennec, Polyanionic (phosphates, silicates, sulfates) frameworks as electrode materials for rechargeable Li (or Na) batteries. *Chem. Rev.* **113**, 6552–6591 (2013). <https://doi.org/10.1021/cr3001862>
308. R. Murugavel, A. Choudhury, M.G. Walawalkar, R. Pothiraja, C.N. Rao, Metal complexes of organophosphate esters and open-framework metal phosphates: synthesis, structure, transformations, and applications. *Chem. Rev.* **108**, 3549–3655 (2008). <https://doi.org/10.1021/cr000119q>
309. R. Sahoo, D.T. Pham, T.H. Lee, T.H.T. Luu, J. Seok, Y.H. Lee, Redox-driven route for widening voltage window in asymmetric supercapacitor. *ACS Nano* **12**, 8494–8505 (2018). <https://doi.org/10.1021/acsnano.8b04040>
310. Y. Yang, H. Hou, G. Zou, W. Shi, H. Shuai, J. Li, X. Ji, Electrochemical exfoliation of graphene-like two-dimensional nanomaterials. *Nanoscale* **11**, 16–33 (2018). <https://doi.org/10.1039/c8nr08227h>
311. S. Yang, P. Zhang, F. Wang, A.G. Ricciardulli, M.R. Lohe, P.W.M. Blom, X. Feng, Fluoride-free synthesis of two-dimensional titanium carbide (MXene) using a binary aqueous system. *Angew. Chem. Int. Ed.* **57**, 15491–15495 (2018). <https://doi.org/10.1002/anie.201809662>
312. M. Le Thai, G.T. Chandran, R.K. Dutta, X. Li, R.M. Penner, 100k cycles and beyond: extraordinary cycle stability for MnO₂ nanowires imparted by a gel electrolyte. *ACS Energy Lett.* **1**, 57–63 (2016). <https://doi.org/10.1021/acsenenergyl.ett.6b00029>
313. P. Zhang, F. Wang, S. Yang, G. Wang, M. Yu, X. Feng, Flexible in-plane micro-supercapacitors: progresses and challenges



- in fabrication and applications. *Energy Storage Mater.* **28**, 160–187 (2020). <https://doi.org/10.1016/j.ensm.2020.02.029>
314. A. Emrani, P. Vasekar, C.R. Westgate, Effects of sulfurization temperature on CZTS thin film solar cell performances. *Sol. Energy* **98**, 335–340 (2013). <https://doi.org/10.1016/j.solener.2013.09.020>
315. J.G. Werner, G.G. Rodríguez-Calero, H.D. Abruña, U. Wiesner, Block copolymer derived 3-D interpenetrating multifunctional gyroidal nanohybrids for electrical energy storage. *Energy Environ. Sci.* **11**, 1261–1270 (2018). <https://doi.org/10.1039/c7ee03571c>
316. T. Liu, F. Yang, G. Cheng, W. Luo, Reduced graphene oxide-wrapped Co_{9-x}Fe_xS₈/Co, Fe–N–C composite as bifunctional electrocatalyst for oxygen reduction and evolution. *Small* **14**, 1703748 (2018). <https://doi.org/10.1002/sml.201703748>
317. H. Niu, Y. Zhang, Y. Liu, B. Luo, N. Xin, W. Shi, MOFs-derived Co₉S₈-embedded graphene/hollow carbon spheres film with macroporous frameworks for hybrid supercapacitors with superior volumetric energy density. *J. Mater. Chem. A* **7**, 8503–8509 (2019). <https://doi.org/10.1039/c8ta11983j>
318. X.M. Lin, J.H. Chen, J.J. Fan, Y. Ma, P. Radjenovic et al., Synthesis and operando sodiation mechanistic study of nitrogen-doped porous carbon coated bimetallic sulfide hollow nanocubes as advanced sodium ion battery anode. *Adv. Energy Mater.* **9**, 1902312 (2019). <https://doi.org/10.1002/aenm.201902312>
319. R. Kumar, S. Sahoo, E. Joanni, R.K. Singh, R.M. Yadav et al., A review on synthesis of graphene, h-BN and MoS₂ for energy storage applications: recent progress and perspectives. *Nano Res.* **12**, 2655–2694 (2019). <https://doi.org/10.1007/s12274-019-2467-8>